

REMTECH

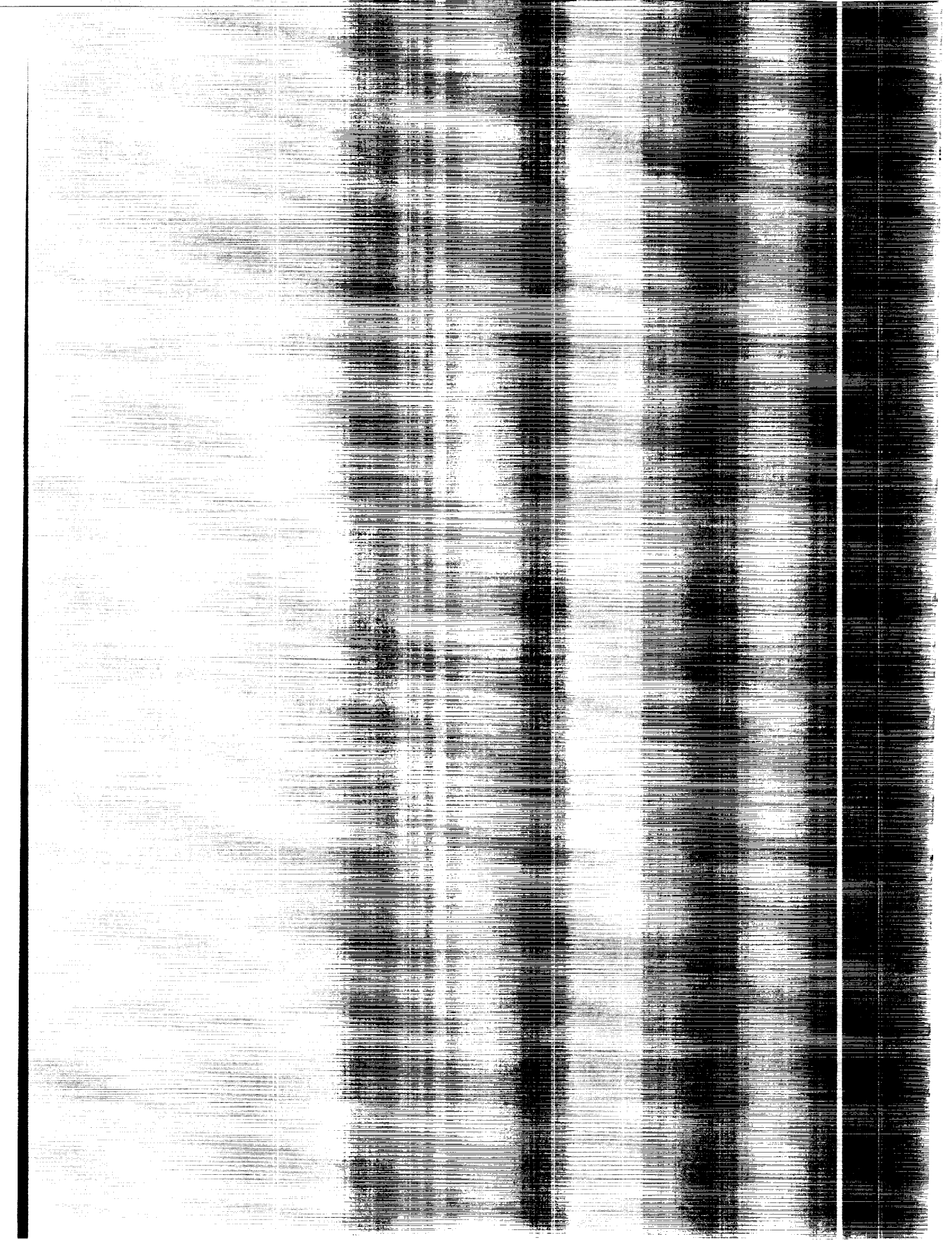
RTR 113-03

(NASA-C-17016) REMTECH SSME
NOZZLE DESIGN FDS Final Report
(Remtech) 114 p

193-26655

Unclassified

G3/20 0163033



ABSTRACT

Thermal protection system thermal damage was observed on the orbiter SSME nozzle aft manifold for 7 of the first 10 Shuttle flights. This problem precipitated efforts at MSFC, Rockwell and Rocketdyne to investigate design thermal environments and thermal protection system designs to implement corrective actions. This effort performed for MSFC addressed nozzle TPS experimental and theoretical thermal modeling, wind tunnel data analyses, aerothermal math modeling, and a new TPS design. The results indicate that the adopted TPS design is currently inadequate to protect the nozzle from a three sigma aerothermal environment, but will protect from most reentry aerothermal environment conditions. It is recommended that a Nicalon fabric barrier be added to the existing TPS to provide complete protection.

FOREWORD

This report presents work which was conducted for Marshall Space Flight Center (MSFC) in response to requirements of Contract NAS8-36151. The work presented was performed at REMTECH's Huntsville office and is entitled "REMTECH SSME Nozzle Design TPS Final Report."

The NASA technical coordination for this study was provided by Mr. Lee Foster of the Thermal Environment Branch of the Systems Dynamics Laboratory.

Contents

ABSTRACT	i
FOREWORD	ii
List of Figures	iv
List of Tables	vii
1 INTRODUCTION	1
2 TESTING	3
2.1 Orbiter/Nozzle Tests	3
2.2 HGF TPS Testing	19
3 MATH MODEL	31
3.1 Aerothermal Models	31
3.2 Thermal Analyses Models	43
4 FLIGHT PREDICTIONS	52
5 DESIGN TRAJECTORY	57
6 DESIGN ENVIRONMENT	61
7 REMTECH TPS DESIGN	68
7.1 1985 Environment	68
7.2 Bridge Concept	73
8 TPS THERMAL RESPONSE	85
8.1 1987 Design Environment	85
8.2 Ramp Design	87
9 CONCLUSIONS AND RECOMMENDATIONS	94
9.1 Conclusions	94
9.2 Recommendations	95
10 REFERENCES	96
Appendix	98

List of Figures

2.1.1 Orbiter Model with Instrumentation Reference System	6
2.1.2 Orbiter-Sting Configuration for Nozzle Heating Test	7
2.1.3 OH-39 SSME Instrumentation	8
2.1.4 OH-84B SSME Instrumentation	9
2.1.5 OH-98 Left Hand SSME Instrumentation	10
2.1.6 OH-98 Right Hand SSME Instrumentation	11
2.1.7 Wind Tunnel Control Surface Set Conditions	12
2.1.8 Base Region Configuration Effects on Heating at $\alpha = 40$ Degrees .	13
2.1.9 Axial Heating Distribution	14
2.1.10 OH-84B Wind Tunnel Data	15
2.1.11 OH-84B and OH-98 Wind Tunnel Data	16
2.1.12 Wind Tunnel Data	17
2.1.13 Effect of Sideslip on SSME Entry Heating	18
2.2.1 Full-Scale Thermocouple and Pressure (Acoustics) Calibration Models	21
2.2.2 0.30 Scaled Calibration Models ($\alpha = 35$)	22
2.2.3 Model 5, STS-13 Full-Scale TPS	23
2.2.4 Model 5, STS-14 Full-Scale TPS	24
2.2.5 STS-13 Calibration ($\alpha = 0$)	25
2.2.6 STS-14 Calibration ($\alpha = 0$)	26
2.2.7 Calibration Model Data for 35 Degrees Angle-of-Attack Flow (0.30 Scale)	27
2.2.8 Theoretical Interference Factors and Data Versus Wedge Angle ($h_i/h_u = (P_i/P_u)^{.8}$) Where the Pressure Ratio is from Wedge Tables . . .	28
2.2.9 Heating Data Rates Summary	29

2.2.10 STS-13 and 14 Layered Insulation Temperature Response Near Peak Heating Location	30
3.1.1 Comparison of Orbiter Base Pressures with Other Entry Vehicles .	32
3.1.2 Angle-of-Attack Effect on Base Pressure	33
3.1.3 Math Model Data (OH-98 and OH-84B)	34
3.1.4 Correlation of Heating Dependence on Angle-of-Attack	35
3.1.5 Envelope of Laminar Circumferential SSME Heating Data (OH-98 and OH-84B)	36
3.1.6 Axial Heating Distribution	37
3.1.7 Axial Heating Distribution	41
3.2.1 SSME Aft Manifold View Factor Distribution to Deep Space . . .	45
3.2.2 TPS Surface Distribution with STS-14 AOA Heating Rate	46
3.2.3 Comparison of Stored vs. Reradiated Load	47
3.2.4 Radiation Equilibrium Temperature	48
3.2.5 Heating Distribution	49
3.2.6 One-Dimensional Model Temperature Response Comparison with HGF Data	51
4.1.1 STS-11 Postflight Photo for SSME #2	53
4.1.2 Elevon Flight Experience	54
4.1.3 Body Flap Flight Experience	55
4.1.4 SSME Aft Manifold Flight Peak Heating Prediction	56
5.1.1 Descending Node Design Trajectory vs. "BET" for STS-1 to STS-32	58
5.1.2 Descending Node Trajectory Velocity Time History	59
5.1.3 Descending Node Trajectory Q Time History	60
6.1.1 Design Environment Elevon Schedule	62
6.1.2 Design Environment Body Flap Schedule	63
6.1.3 Peak Heating Prediction	64

6.1.4 Worst Heating Time History	65
6.1.5 Worst Forward, Mid and Aft Heating Time Histories	66
6.1.6 Peak Circumferential Heating Distribution	67
7.1.1 Comparison of 3 Sigma and No Sigma Angle-of-Attack	69
7.1.2 Nominal Alpha and Three Sigma ICD Design Trajectory	71
7.1.3 Heating Rate Distribution at PHI = 49°	72
7.2.1 REMTECH Design TPS	76
7.2.2 TPS Design #1, Internal Stiffeners	77
7.2.3 TPS Close-Out Concept at Ramp-Manifold Intersect	78
7.2.4 Thermal Conductivity vs. Temperature for Different Cerachrome Densities (Ref. 3)	80
7.2.5 SSME Redesigned TPS	81
7.2.6 Four Lb Cerachrome Thickness for SSME Redesigned TPS	83
7.2.7 REMTECH TPS Design	84
8.1.1 Worst Heating Time History	86
8.2.1 Current "Ramp" TPS Capability	88
8.2.2 Current Corner "Ramp" TPS Capability	89
8.2.3 1-D Thermal Model Surface Temperature Response	90
8.2.4 Time to Reach Nichrome Melt Temperature	91
8.2.5 Radiation Equilibrium Temperature Analysis for STS-9	92
8.2.6 Radiation Equilibrium Temperature Analysis	93
A1 Thermal Conductivity vs. Temperature	99
A2 Comparison of Different Cerachrome Conductivity	100
A3 Conductivity vs. Temperature for Different Cerachrome Density (Ref 6)	101
A4 Thermal Conductivity vs. Temperature for 6 Lb. Cerachrome	102
A5 Thermal Conductivity vs. Temperature for 8 Lb. Cerachrome	102

List of Tables

1.1.1 SSME Aft Manifold Damage History	2
2.1.1 Orbiter/SSME Nozzle Tests	5
3.1.1 Aeroheating Math Model Components	38
3.1.2 SSME Heating Calculation Procedure	39
3.1.3 Rockwell Math Model	40
3.1.4 REMTECH and Rockwell Math Model Prediction vs. Flight Data	42
3.2.1 Radiation Equilibrium Temperature Analysis	44
3.2.2 One-Dimensional Thermal Analysis	50
7.1.1 Distribution of Maximum Heat Flux to SSME Nozzle (Ref. 10) . .	70
7.2.1 TPS Materials Considered and Selected	79
7.2.2 Estimated TPS Weight	82

Section 1

INTRODUCTION

Thermal damage to the SSME aft manifold TPS has been observed for flights STS-8 through STS-13 as shown in Table 1.1.1. This damaged area is located on the ME2 and ME3 and extends over a region of approximately one square foot. Total failure or burn-through of the TPS could lead to severe thermal damage of the SSME manifold and loss of an engine nozzle necessitating nozzle replacement causing significant schedule delays and cost increases. Thermal damage to the manifold can be defined as a situation where the manifold temperature becomes greater than 1300° F; thereby causing loss of heat treat to the nozzle.

Table 1.1.1: SSME Aft Manifold Damage History

STS	DAMAGE DESCRIPTION
1	NONE NOTED
2	NONE NOTED
3	NONE NOTED
4	ME2 - OUTER SCREEN MELTED ONLY ME3 - MELTED THROUGH INSULATION LOCALLY, MANIFOLD EXPOSED
5	ME3 - OUTER SCREEN & FOIL MELTED
6	ME2 - 3/4" HOLE THROUGH SCREEN, FOIL & INTO BATTING ME3 - ONE AREA UNKNOWN EXTENT
7	ME2 - NO DAMAGE ME3 - NUMEROUS AREAS OF SCREEN DAMAGE, 3/4" OR LESS
8	ME2 - MELTING AT 5 LOCATIONS; THROUGH SCREEN & FOIL IN WORST CASE ME3 - MELTING AT 5 LOCATIONS; THROUGH SCREEN, FOIL, & INSULATION
9	ME2 - MELTING OF SCREEN & FOIL ME3 - MELTING OF SCREEN & FOIL
11	ME2 - MELTING OF SCREEN, FOIL, & INSULATION; MANIFOLD EXPOSED ME3 - MELTING OF SCREEN & FOIL

Section 2

TESTING

2.1 Orbiter/Nozzle Tests

Four wind tunnel tests were conducted to measure the relative heating on the SSME lower engines. These tests were conducted at AEDC Tunnel B with a nominal Mach 8 flow condition. The first two tests, OH-39 and OH-49, (Refs. 1,2) used smooth SSME nozzle geometries, whereas the later two tests, OH-84B (Ref. 3) and OH-98, (Ref. 4) used nozzles with heat band simulations (Table 2.1.1).

The instrumentation reference system for these tests is shown in Fig. 2.1.1. The vertical tail sting attachment used in testing the nozzle components for these tests is shown in Fig. 2.1.2.

Figures 2.1.3 through 2.1.6 show the SSME instrumentation for the tests. The summary of the wind tunnel data for OH-84B and OH-98 is shown in Fig 2.1.7. The OH-98 test contained data where the base region configuration was altered. The configurations were:

Config. #0 Nominal flight geometry (Nominal)

Config. #1 Hardware added to body flap to produce a rectangular platform (Rectangular Body Flap)

Config. #2 Wedges added to aft side of fuselage (Small Fence)

Config. #3 Plate extension of fuselage side and body flap (Large Fence)

The data shown in Fig. 2.1.8 clearly show that the large fence blocks the flow from direct impingement on the nozzle. Thus, the impingement flow is not coming from the aft edge of the body flap, but rather from the elevon-body flap corner. The OH-98 data for axial heating distribution are shown in Fig. 2.1.9. Figures 2.1.10 to 2.1.12 show Stanton number versus Reynolds number plots of OH-98 and OH-84B data. These data indicate that transition from laminar to turbulent flow occurs between 1.0 and 2.0 million Reynolds number. This indicates that to establish the

type of flow, the whole Reynolds number spectrum must be analyzed. The effect of sideslip on SSME entry heating is shown in Fig. 2.1.13.

Table 2.1.1: Orbiter/SSME Nozzle Tests

TEST	NOZZLE	α	β	δ_e	δ_{bf}	α_N	β_N
OH-39	LH (Smooth)	20, 25, 30 35, 40, 45	-2, 0, 2	-30, -15, -7 0, 5, 10	0, 5, 15, 22	10, 15, 20	0, 3.45
OH-84B	RH (Hat Bands)	40	0	-15, -12.5,-5, 0, 5, 7.5	-12.5, -5, 0, 5, 8, 15, 23.5	20	0
OH 98	LH (Smooth) RH (Hat Bands)	25, 30, 35 40, 45	0	-15, -10, -7.5, -5, -2.5, 0 5, 7.5, 10	-12.5, 0, 6.5, 14.5, 19, 23.5	20	0

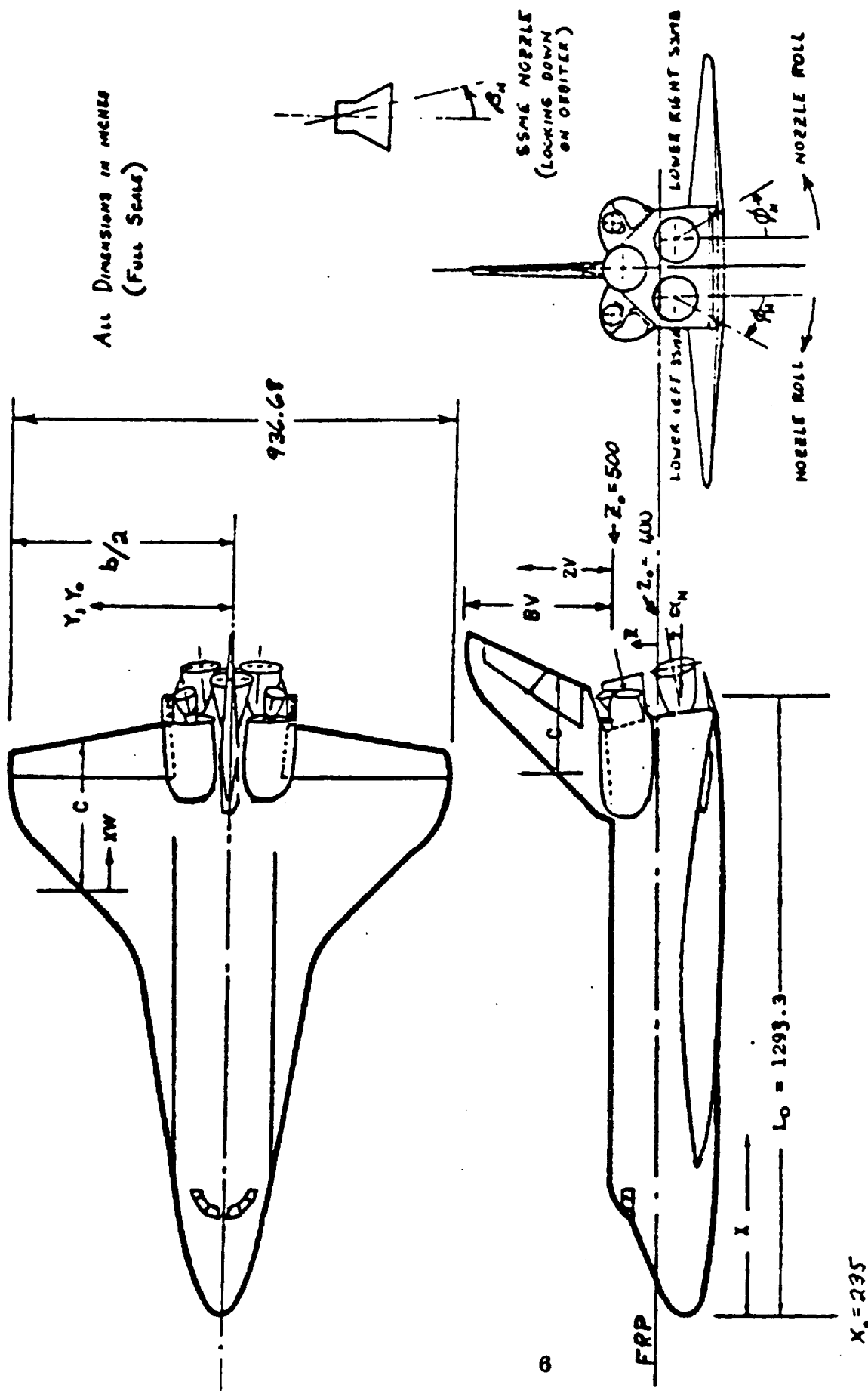


Figure 2.1.1: Orbiter Model with Instrumentation Reference System

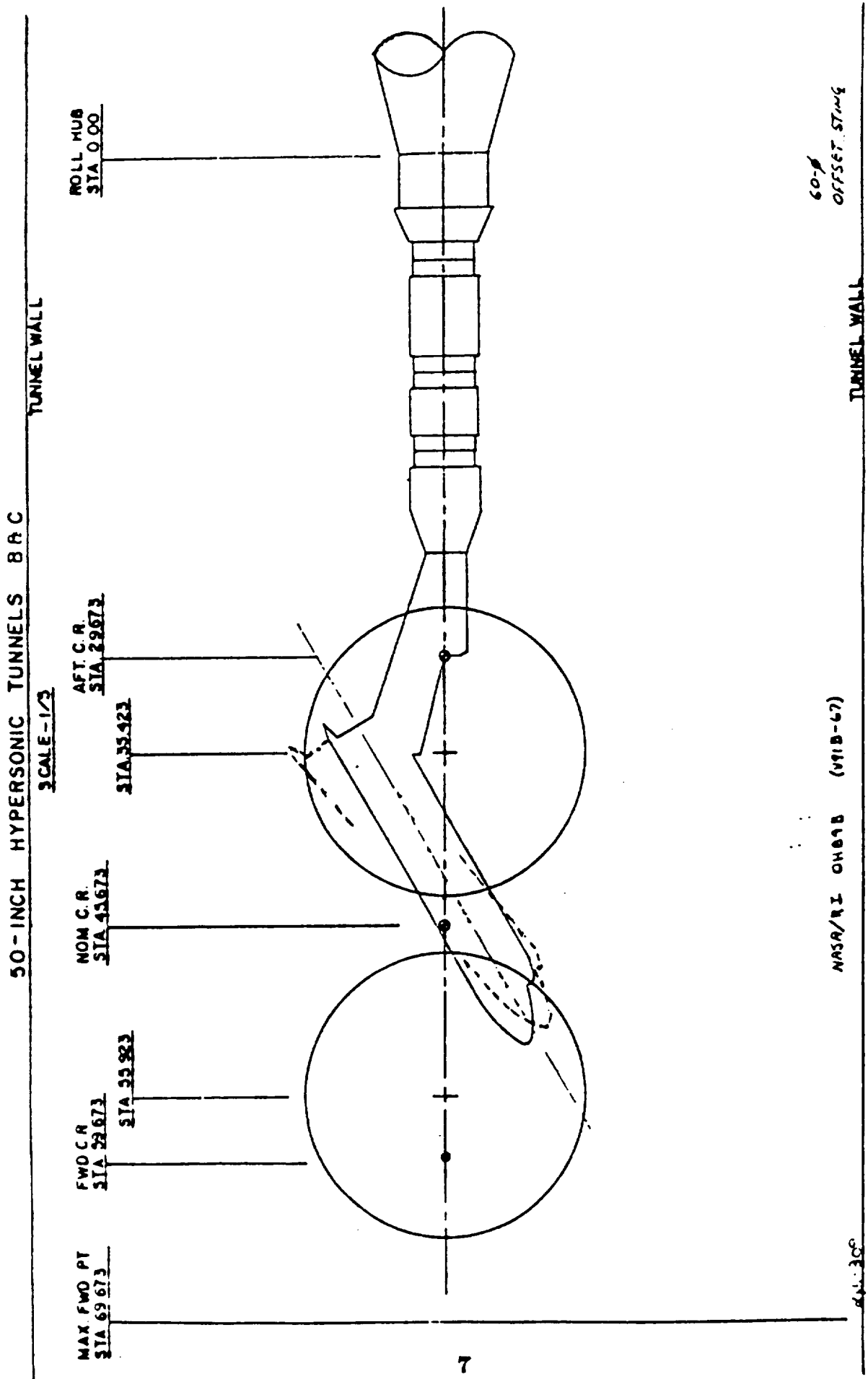


Figure 2.1.2: Orbiter-Sting Configuration for Nozzle Heating Test

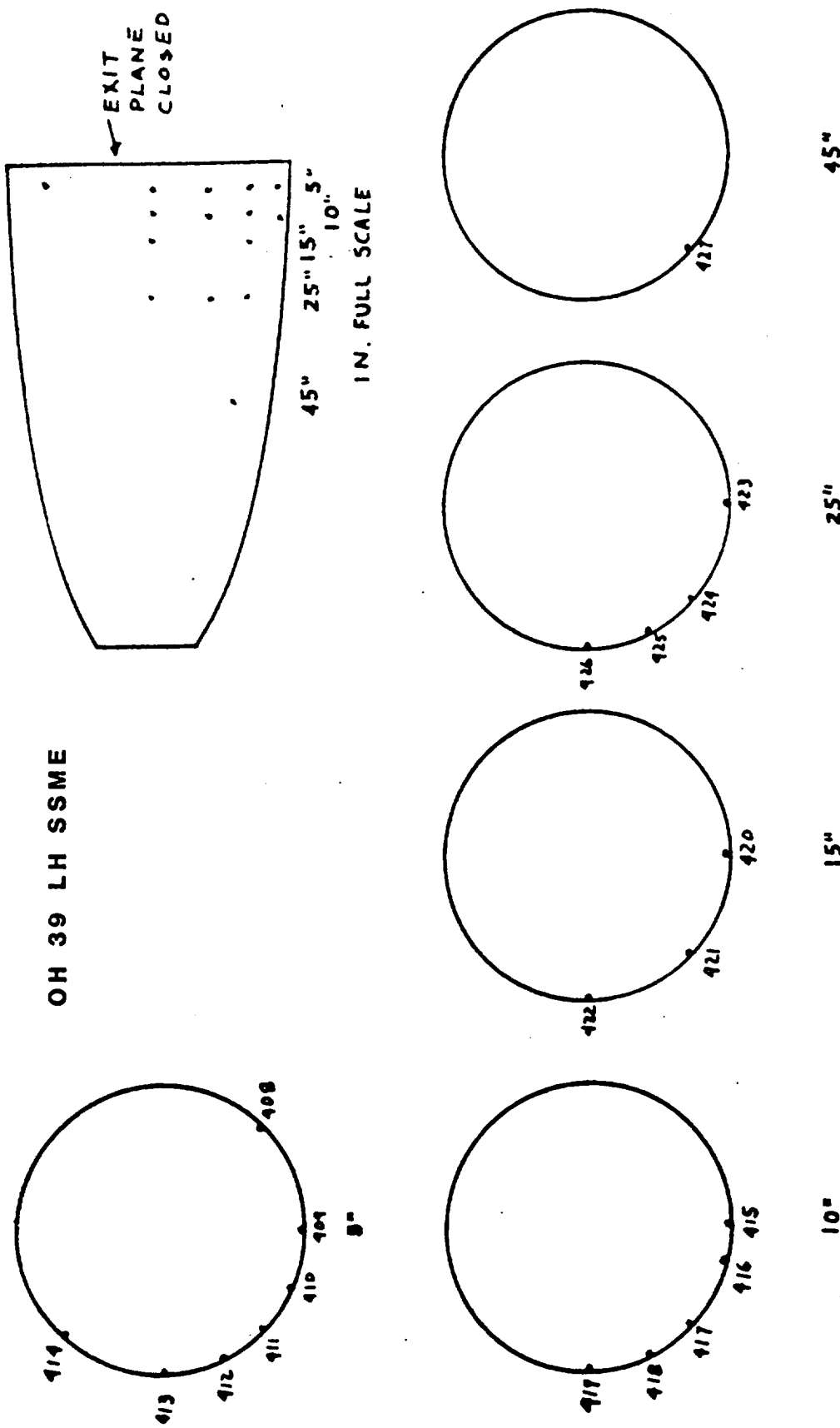


Figure 2.1.3: OH-39 SSME Instrumentation

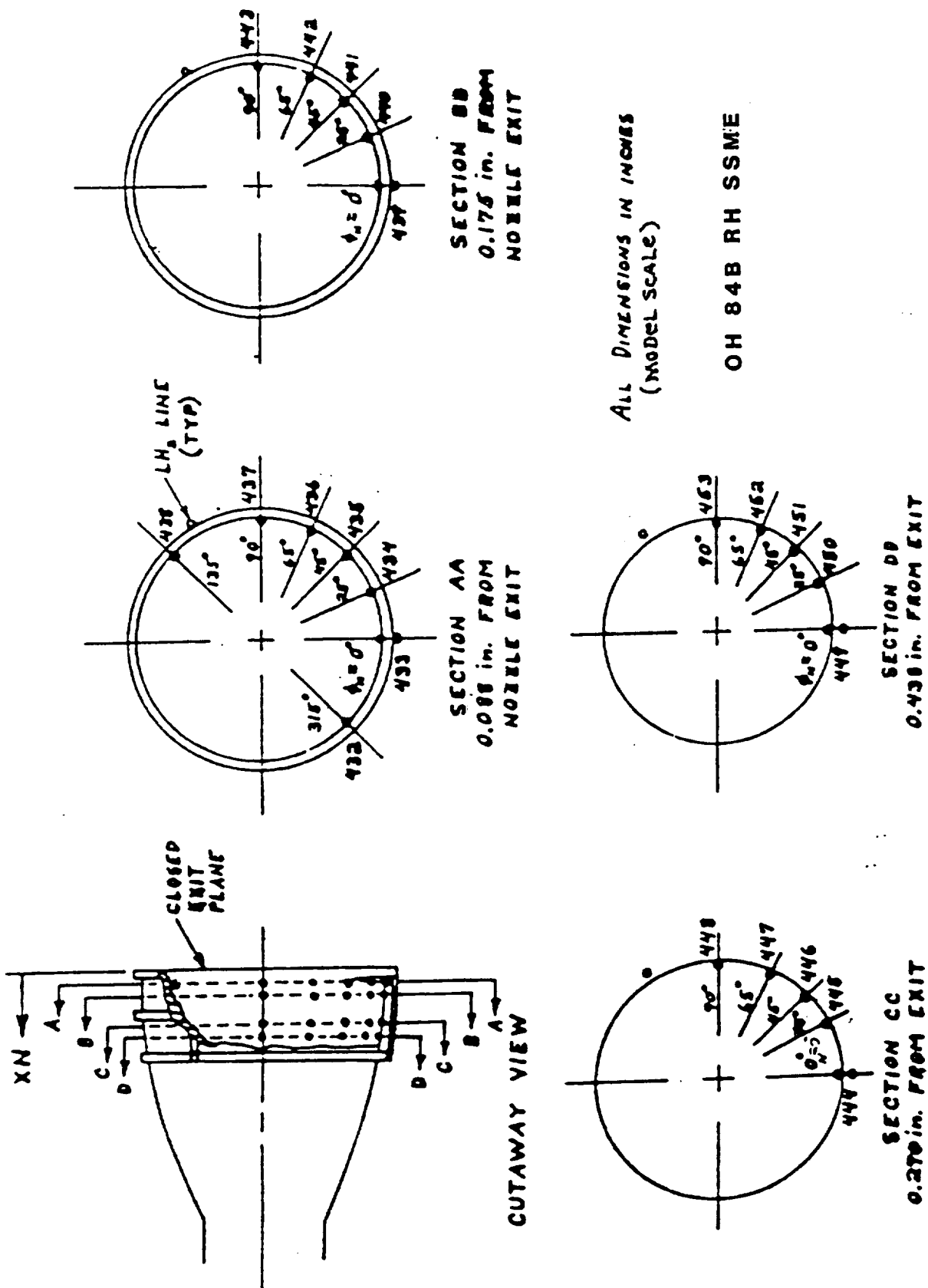


Figure 2.1.4: OH-84B SSME Instrumentation

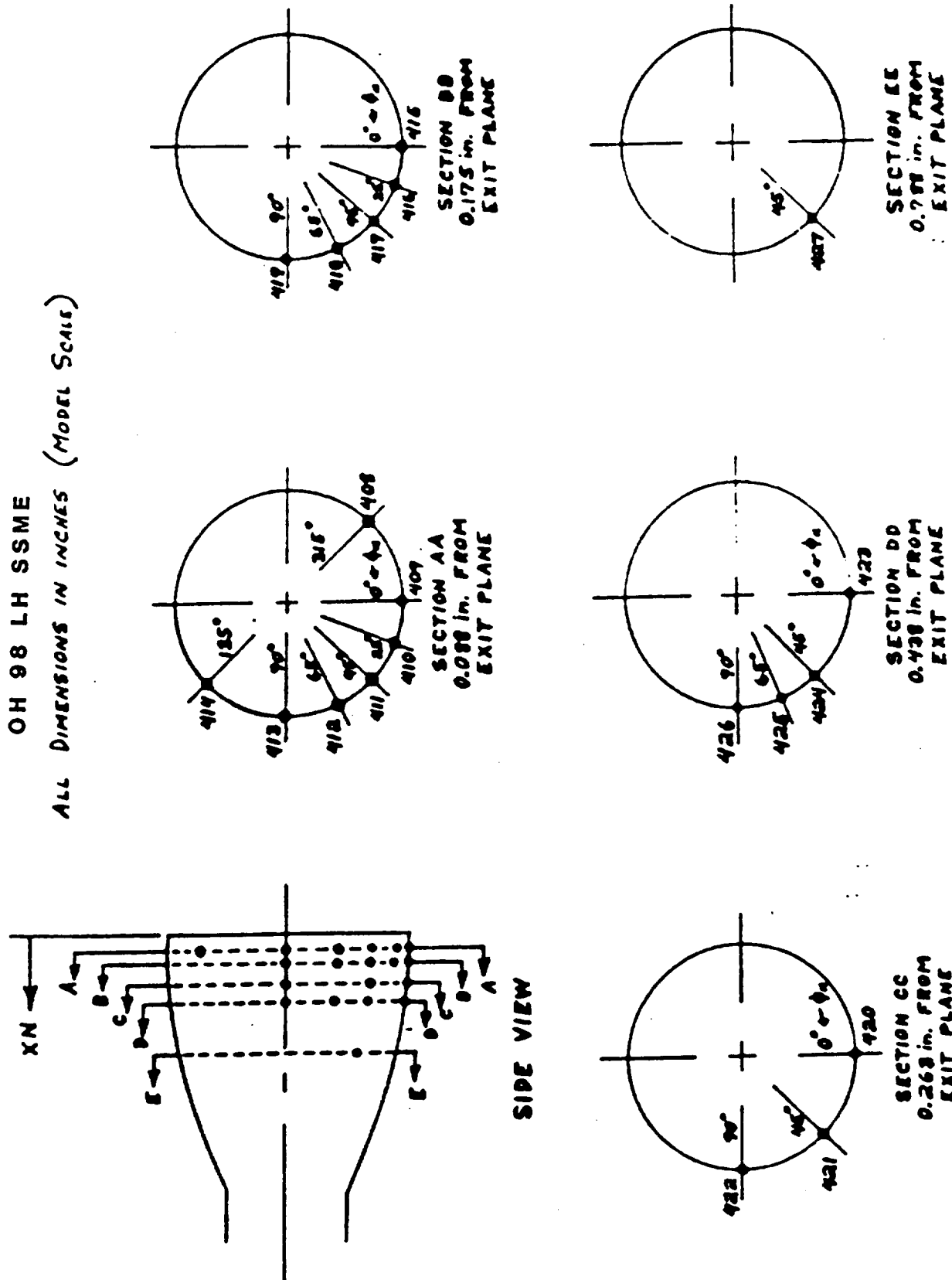


Figure 2.1.5: OH-98 Left Hand SSME Instrumentation

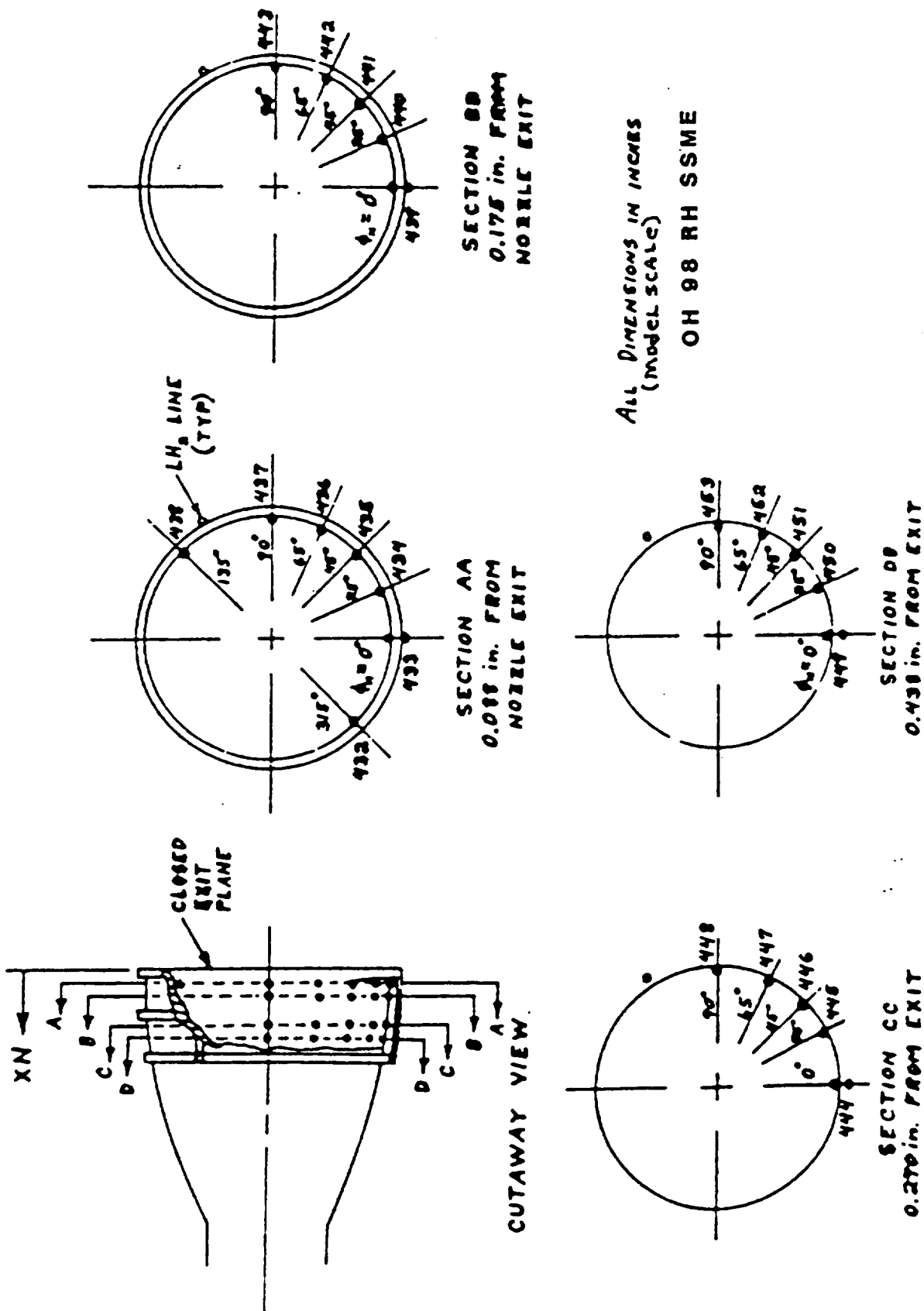


Figure 2.1.6: OH-98 Right Hand SSME Instrumentation

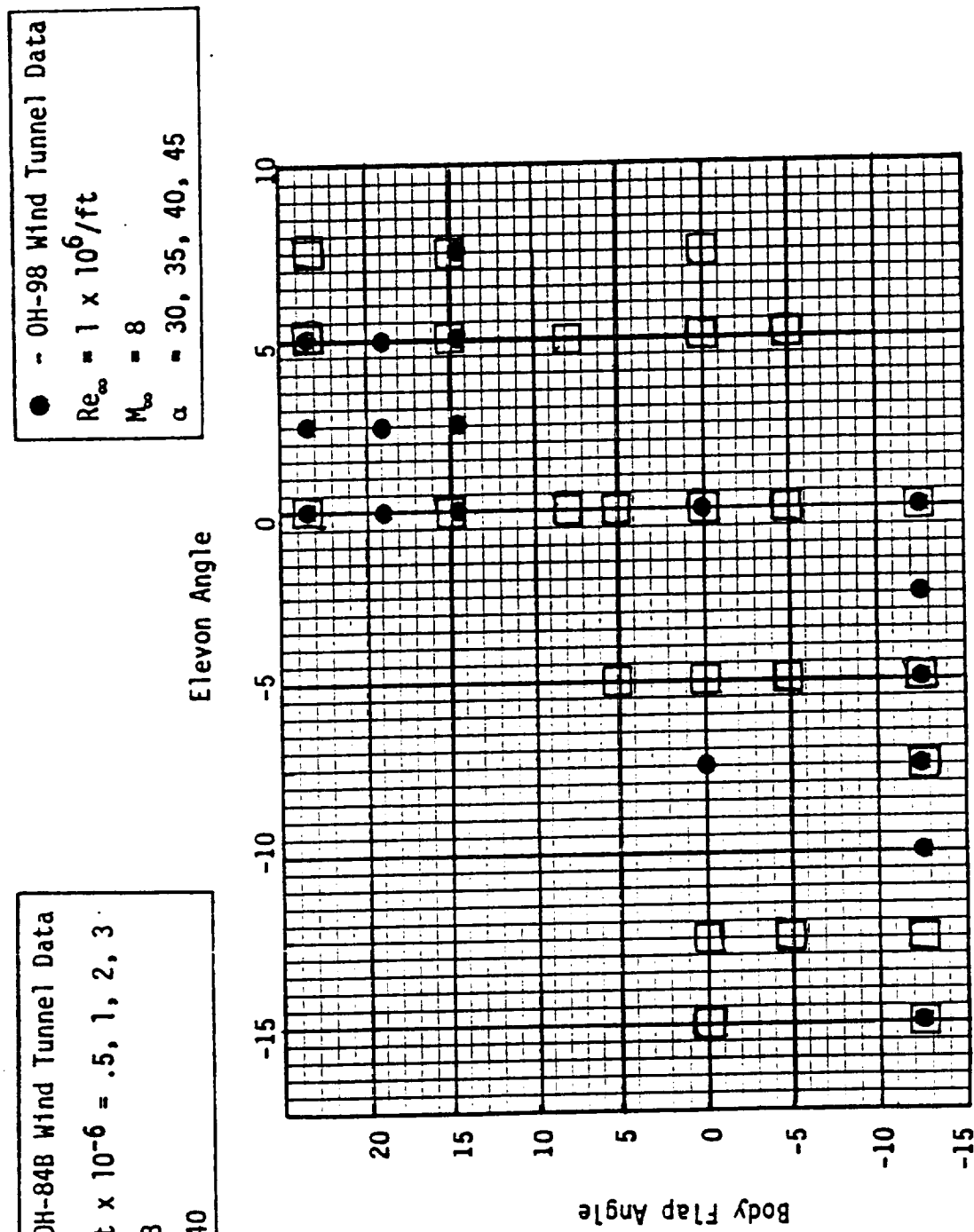


Figure 2.1.7: Wind Tunnel Control Surface Set Conditions

OH-98 TEST GEOMETRY EFFECTS

REMTECT

RTR 113-03

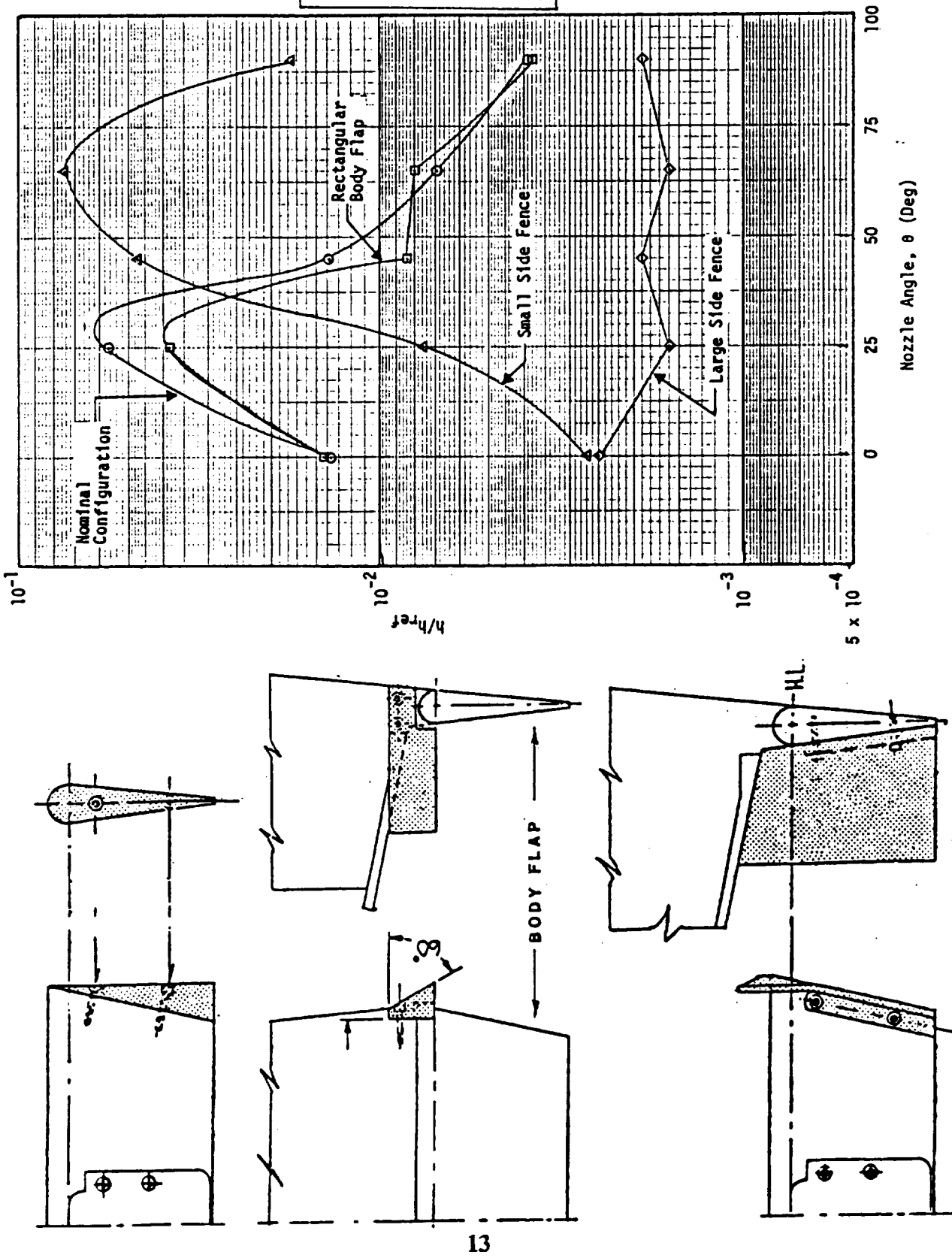


Figure 2.1.8: Base Region Configuration Effects on Heating at $\alpha = 40$ Degrees

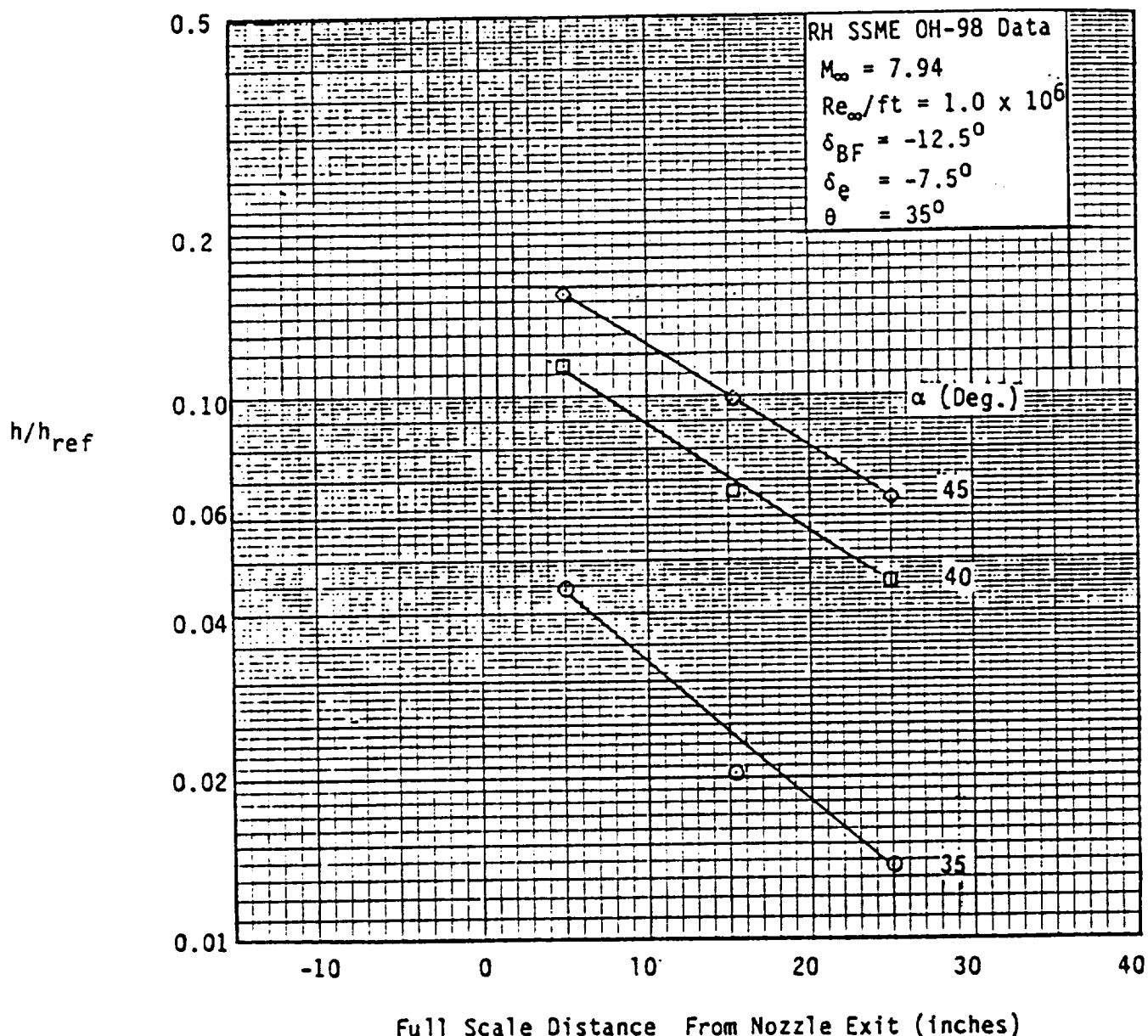


Figure 2.1.9: Axial Heating Distribution

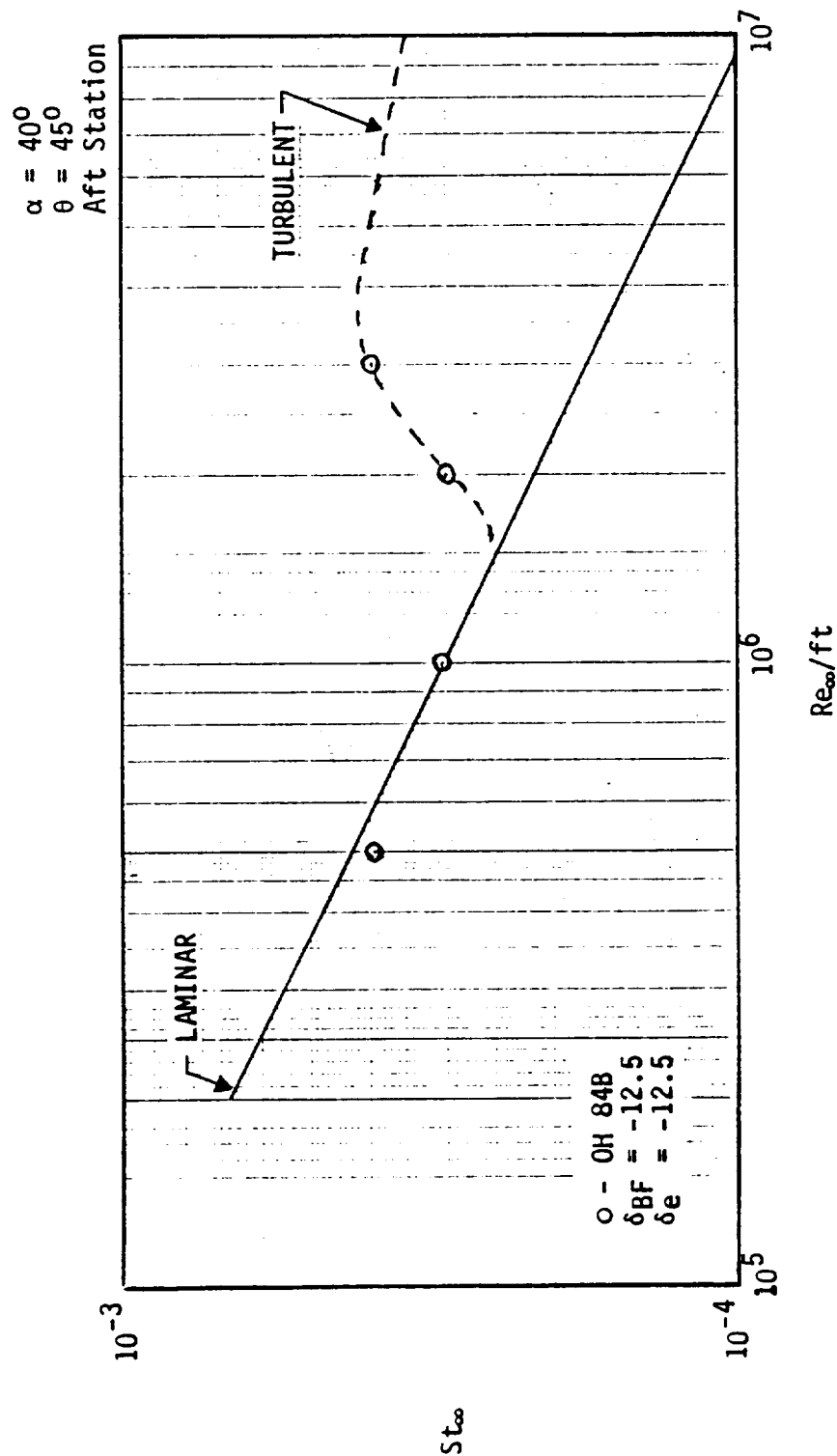


Figure 2.1.10: OH-84B Wind Tunnel Data

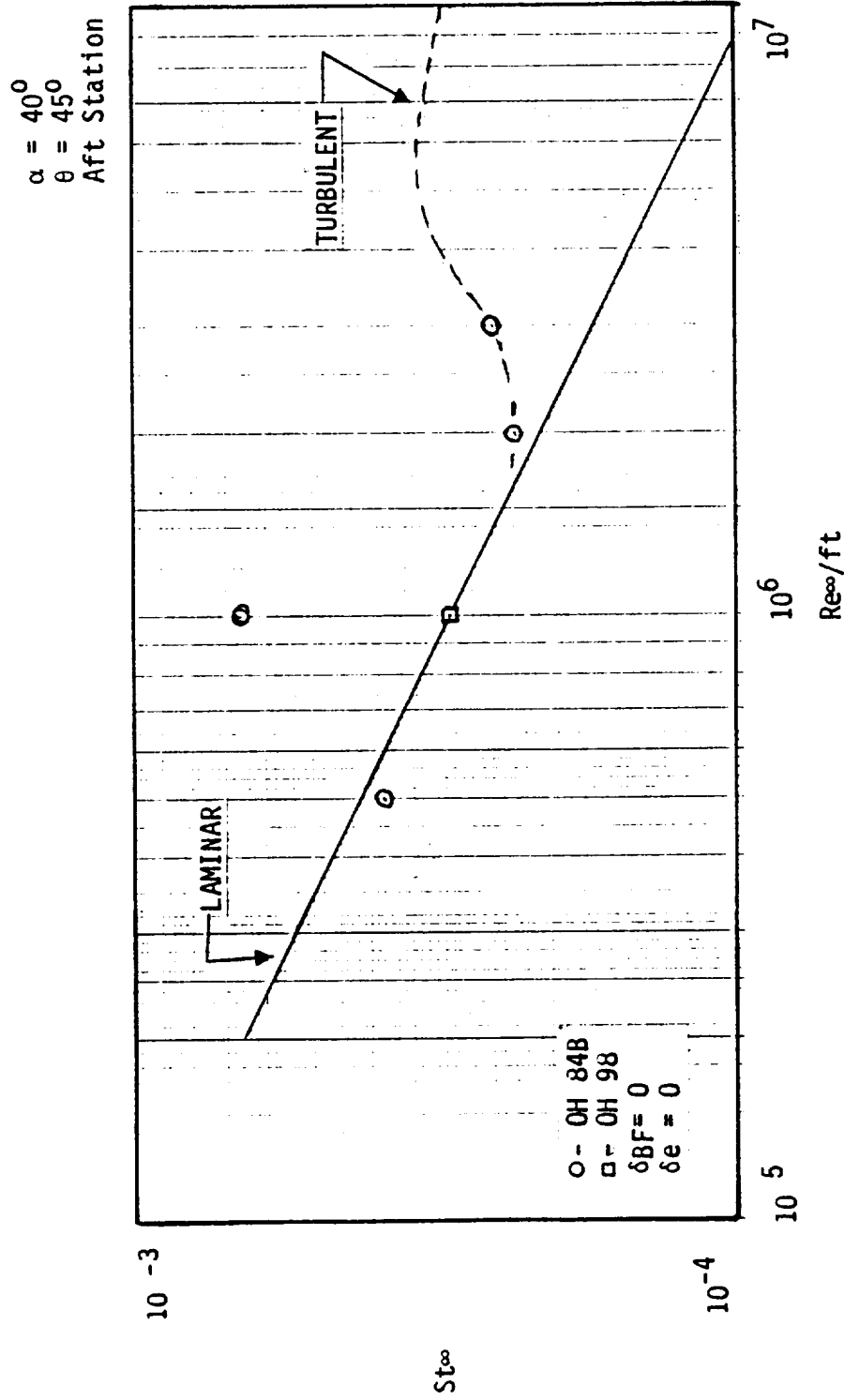


Figure 2.1.11: OH-84B and OH-98 Wind Tunnel Data.

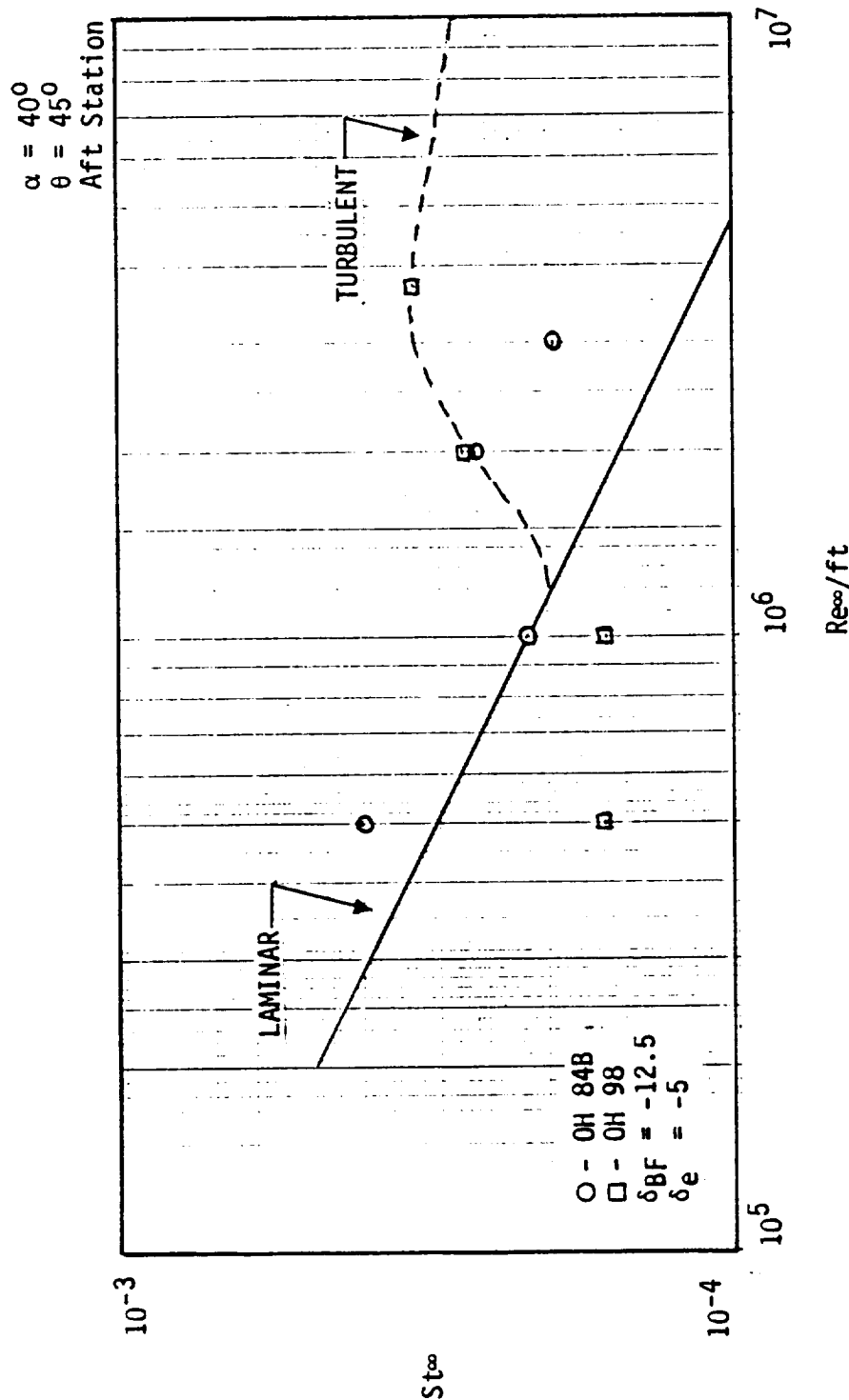
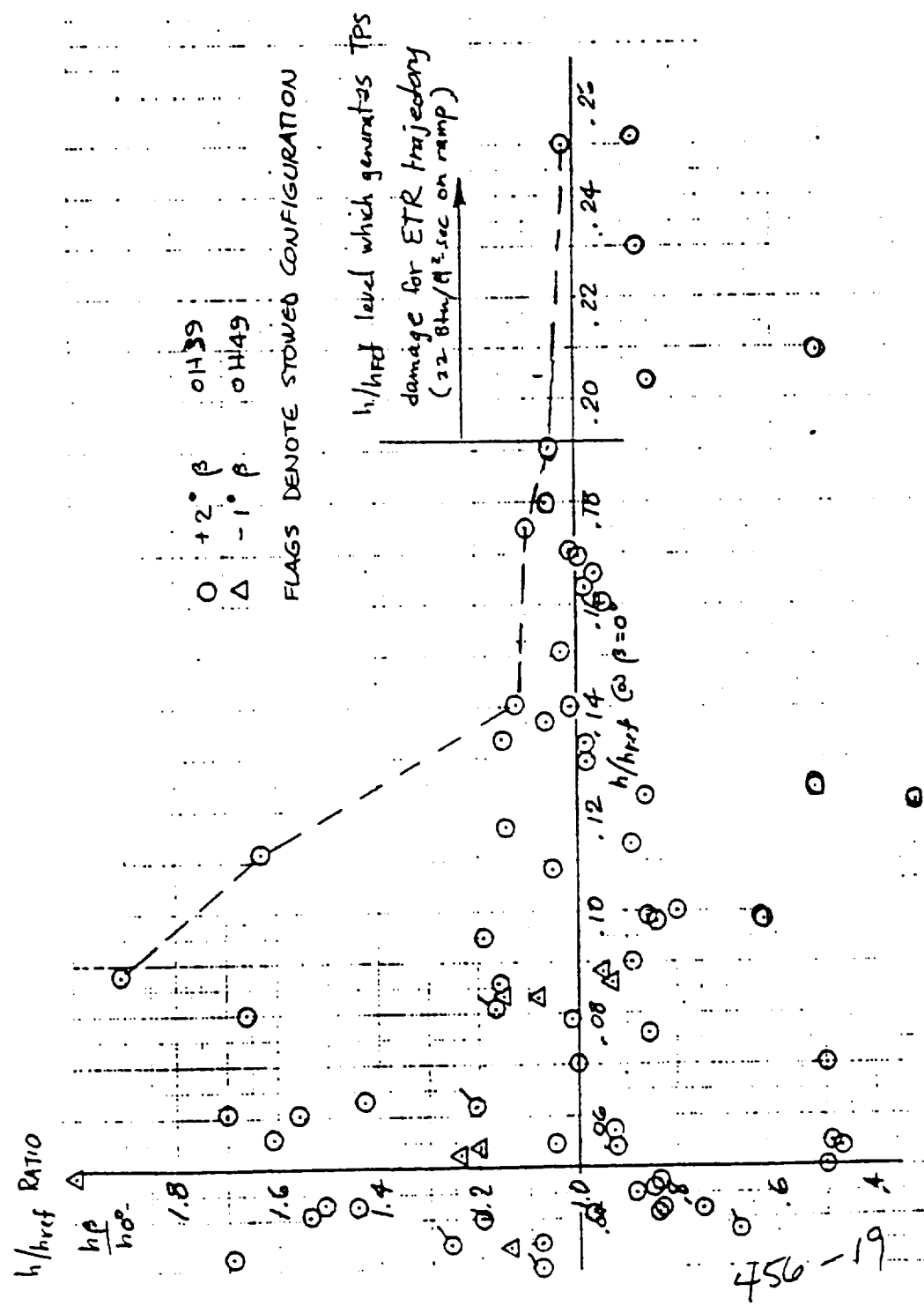


Figure 2.1.12: Wind Tunnel Data



FROM ROCKWELL/DONNEY

09/09/87 17:16 P.18

Figure 2.1.13: Effect of Sideslip on SSME Entry Heating

2.2 HGF TPS Testing

Hot Gas Facility (HGF) tests were initiated to provide a thermal, acoustic and flutter environment for the redesigned TPS to be flown on STS-14. The major change to the TPS was the addition of an aerodynamic fairing which was originally thought to reduce aerodynamic heating and increase radiative exchange to deep space. The original intent was to qualitatively provide data for acceptance of the new TPS. As the tests progressed, it became clear that more than qualitative data could be obtained from these tests. As a result, data were obtained which were useful in developing math models of both the flight environment and thermal response of the TPS. Data which were obtained were heat transfer, pressure, acoustic, temperature response and flutter (high speed movies). These tests are documented in detail in Ref. 5 and will only be summarized herein. The zero angle-of-attack calibration models used in this test are shown in Fig. 2.2.1. These models are full-scale and are approximately 12 inches wide. Also shown in Fig. 2.2.1 is the STS-14 calibration model with 40-mesh screen over the .030 inch stainless steel thin skin and a schematic of T/C attachment to the screen wire. Figure 2.2.2 shows the STS-13 and 14 thirty percent scale calibration models at an angle of attack of 35 deg. The STS-13 full-scale TPS model is depicted in Fig. 2.2.3. Also shown in Fig. 2.2.3 is the cross section of the layer of foil, mesh and batting which make up the TPS and the thermocouple locations within the TPS. Figure 2.2.4 shows the TPS model cross section for the STS-14 configuration and the thermocouple locations.

Several hot flow runs were made with the STS-13 and 14 configuration calibration models. Nominal test calculations were:

$$\begin{aligned} M_\infty &= 3.4 \\ P_c &= 100 \text{ psia} \\ T_c &= 2200^\circ\text{F} \end{aligned}$$

produced by hydrogen lean combustion in air. Heat transfer results are shown in Figs. 2.2.5 and 2.2.6 for the STS-13 and 14 configurations, respectively. Peak heating occurs on the nose of the manifold as seen in Fig. 2.2.5 and forward on the ramp on the STS-14 configuration. Note that for this zero angle-of-attack condition, the heating to the STS-14 configuration is a factor of 2 lower than for the STS-13 configuration. The theory shown for the STS-14 configuration is wedge shock and local wedge pressure with Spaulding-Chi heat transfer using Von Karman Reynolds analogy factor. The heat transfer with the 40 mesh screen shown in Fig. 2.2.6 is the heat transfer to the metallic skin below the screen.

Heat transfer data for the 30 percent scale models at 35 deg angle-of-attack

are shown in Fig. 2.2.7. Note the peak heating for both configurations is about the same. This is not surprising, since previous experimental data have shown this same effect. Figure 2.2.8 shows experimental data of wedges which have wedge angles of 0 to 90 deg. Note that for our Mach number of 3.4, the zero angle-of-attack test corresponds to a wedge angle of 90 to 9 deg for STS-13 to 14, respectively. The peak heating ratio is $3.6/1.9 = 1.89$, which is approximately the ratio measured as shown in Figs. 2.2.5 and 2.2.6. However, for 35 deg angle-of-attack, the wedge angle to use in Fig. 2.2.8 is 90 and 44 deg for STS-13 and 14, respectively. As seen in Fig. 2.2.8, this gives about the same heating as verified by data shown in Fig. 2.2.7.

Heating data ratios are summarized in Fig. 2.2.9 where data are ratioed to the full scale X=5 inch location where engine wind tunnel data are available. No significant influence of the steerhorn was observed in the data. The peak heating for the STS-14 configuration at 35 deg angle-of-attack is essentially the same as for the STS-13 configuration.

Temperature response of the layered insulation on the STS-13 and STS-14 configurations was determined from thermocouples placed between the various materials. Each thermocouple was first spot welded to a one-half inch square .001-inch stainless steel foil and then placed between the layers of insulation. This was done to ensure thermal contact with the insulation material while adding very little thermal mass. Typical results using this technique are shown in Fig. 2.2.10 for the STS-13 and 14 TPS. Notice that the outer surface thermocouple indicates that the surface temperature responds as quickly as expected in a radiatively cooled structure, whereas the internal temperature response is quite benign. The drop in temperature near 12 seconds for the STS-13 configuration was due to TPS structural failure. High-speed movies taken during these tests showed violent movement and flutters of the insulation forward of the manifold which may allow hot gas infiltration into the TPS. The movies showed that the STS-14 configuration was much less susceptible to flutters than the STS-13 configuration.

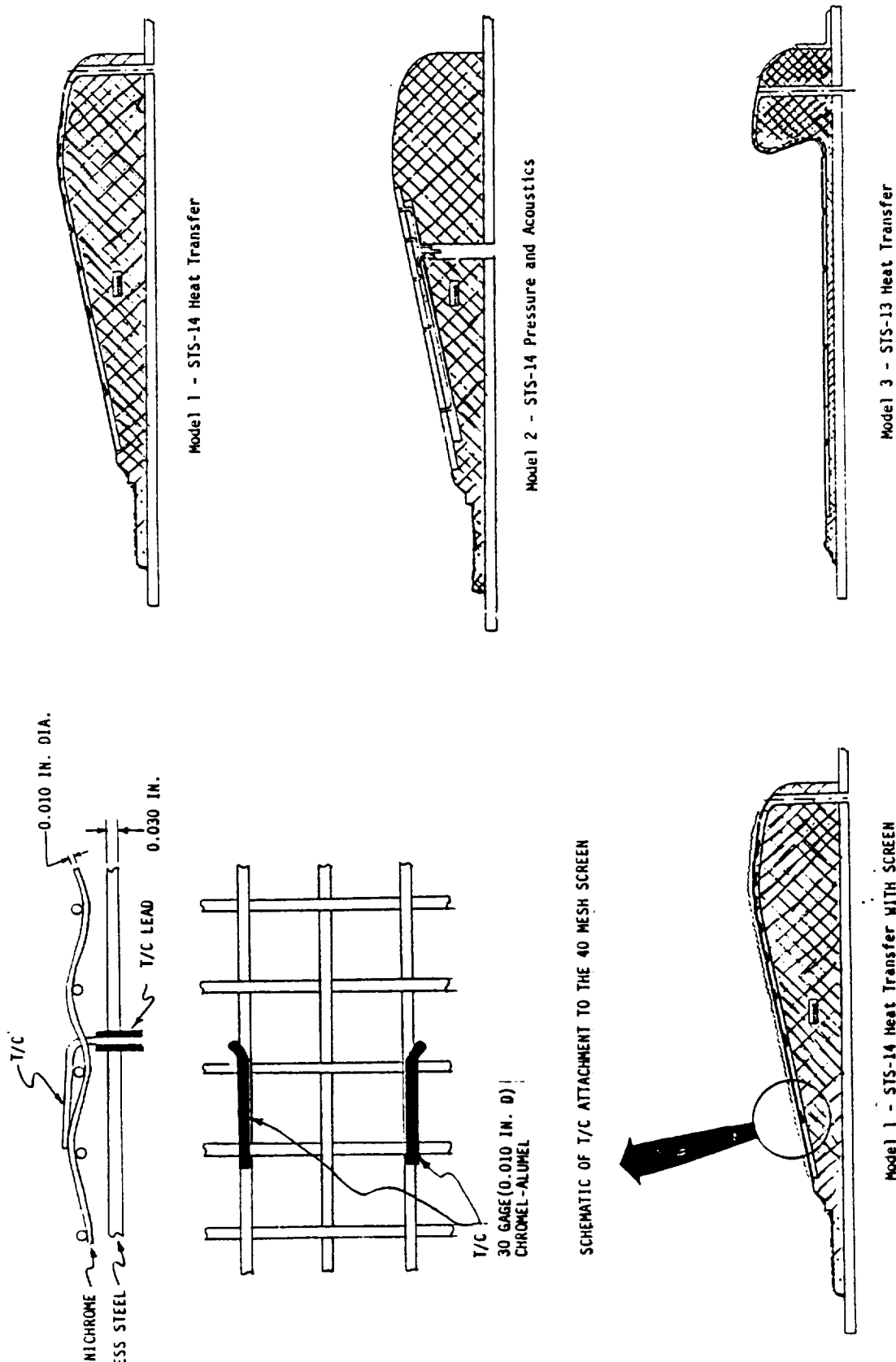
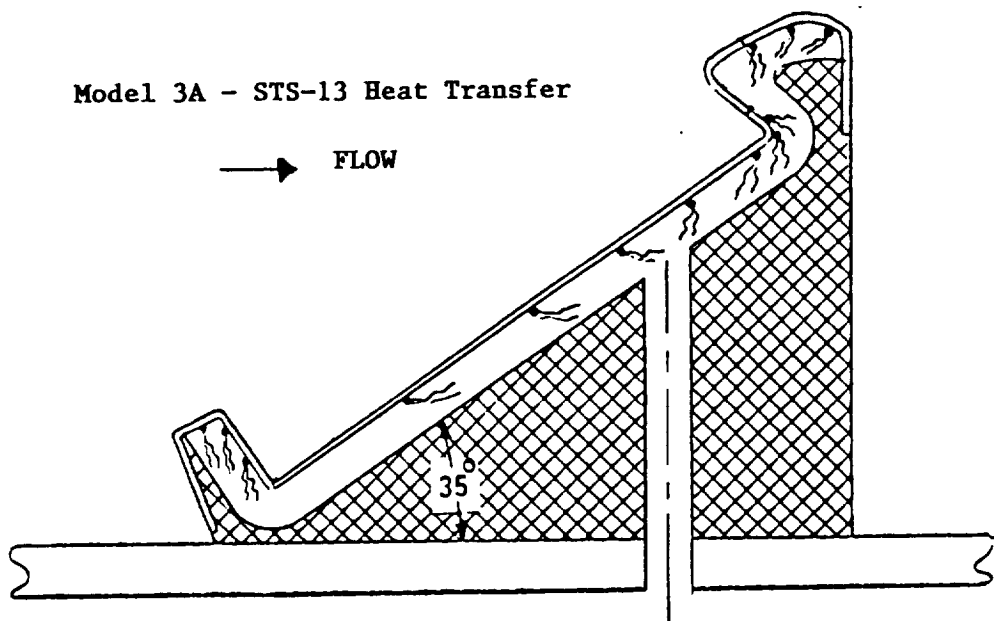
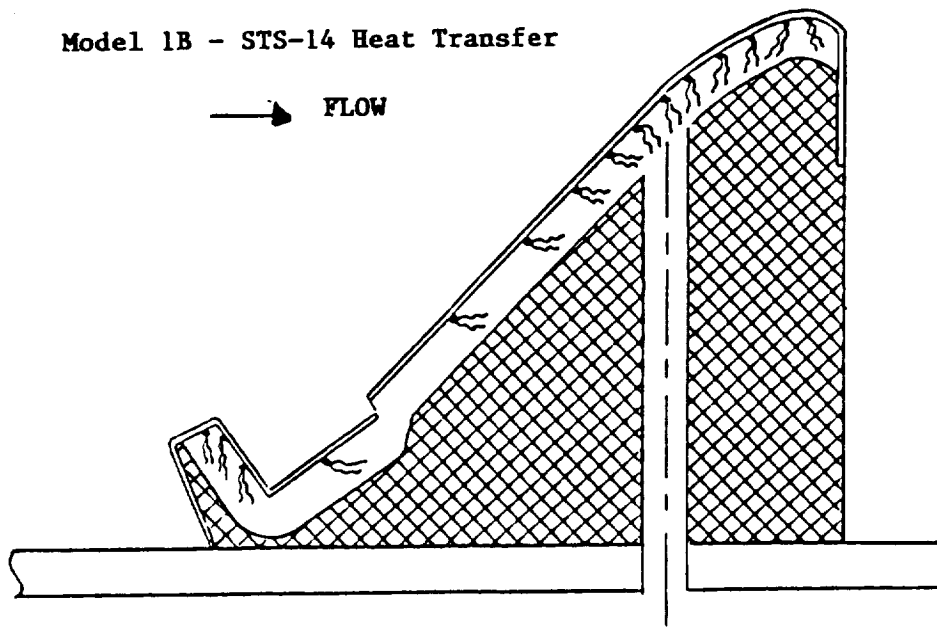


Figure 2.2.1: Full-Scale Thermocouple and Pressure (Acoustics) Calibration Models

Model 3A - STS-13 Heat Transfer



Model 1B - STS-14 Heat Transfer

Figure 2.2.2: 0.30 Scaled Calibration Models ($\alpha = 35$)

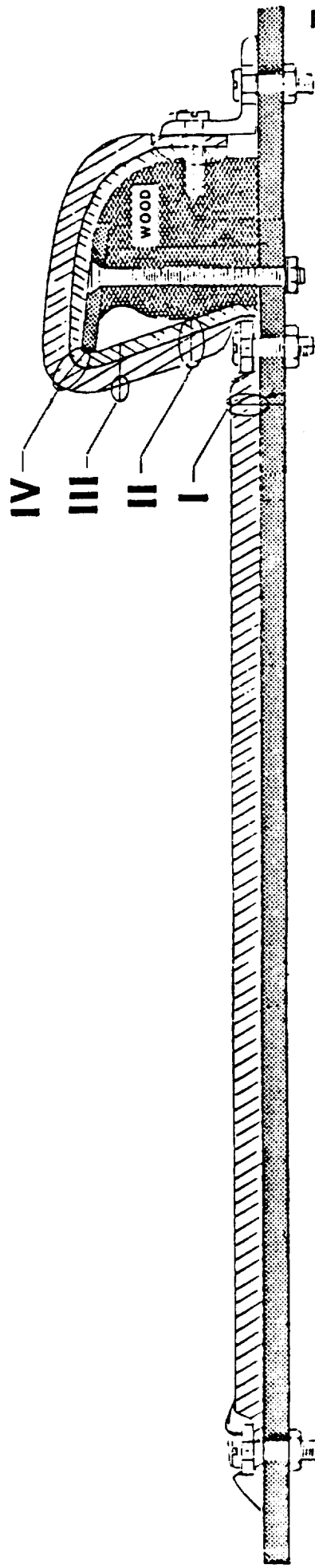
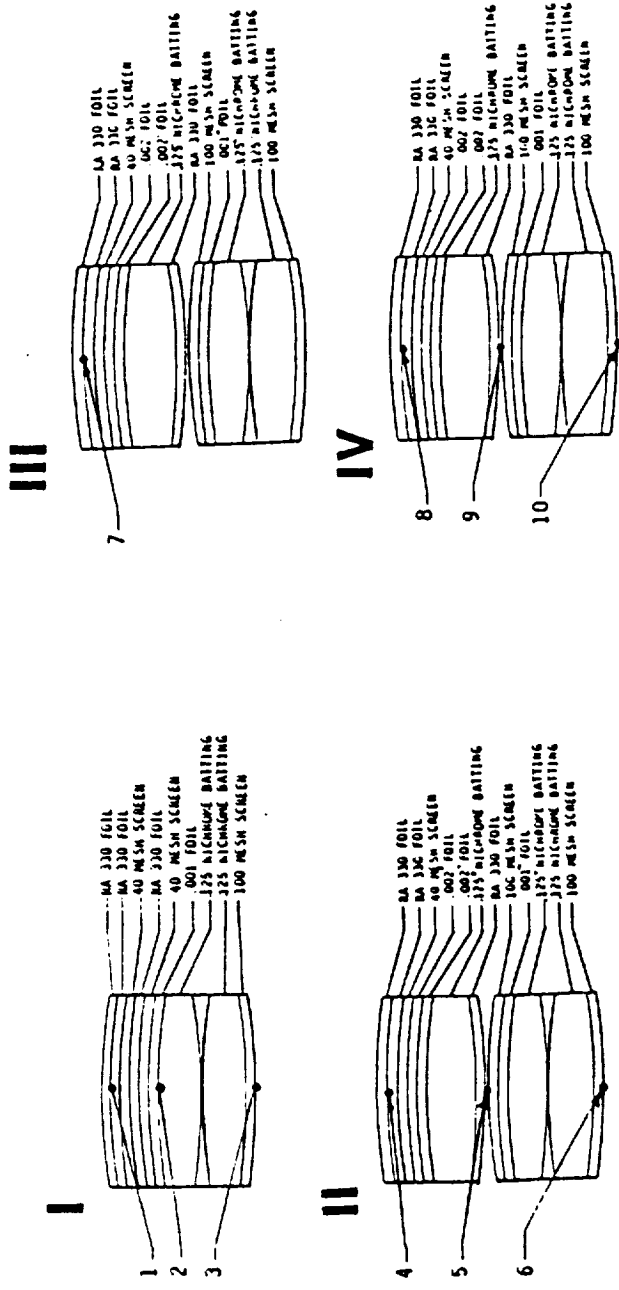


Figure 2.2.3: Model 5, STS-13 Full-Scale TPS

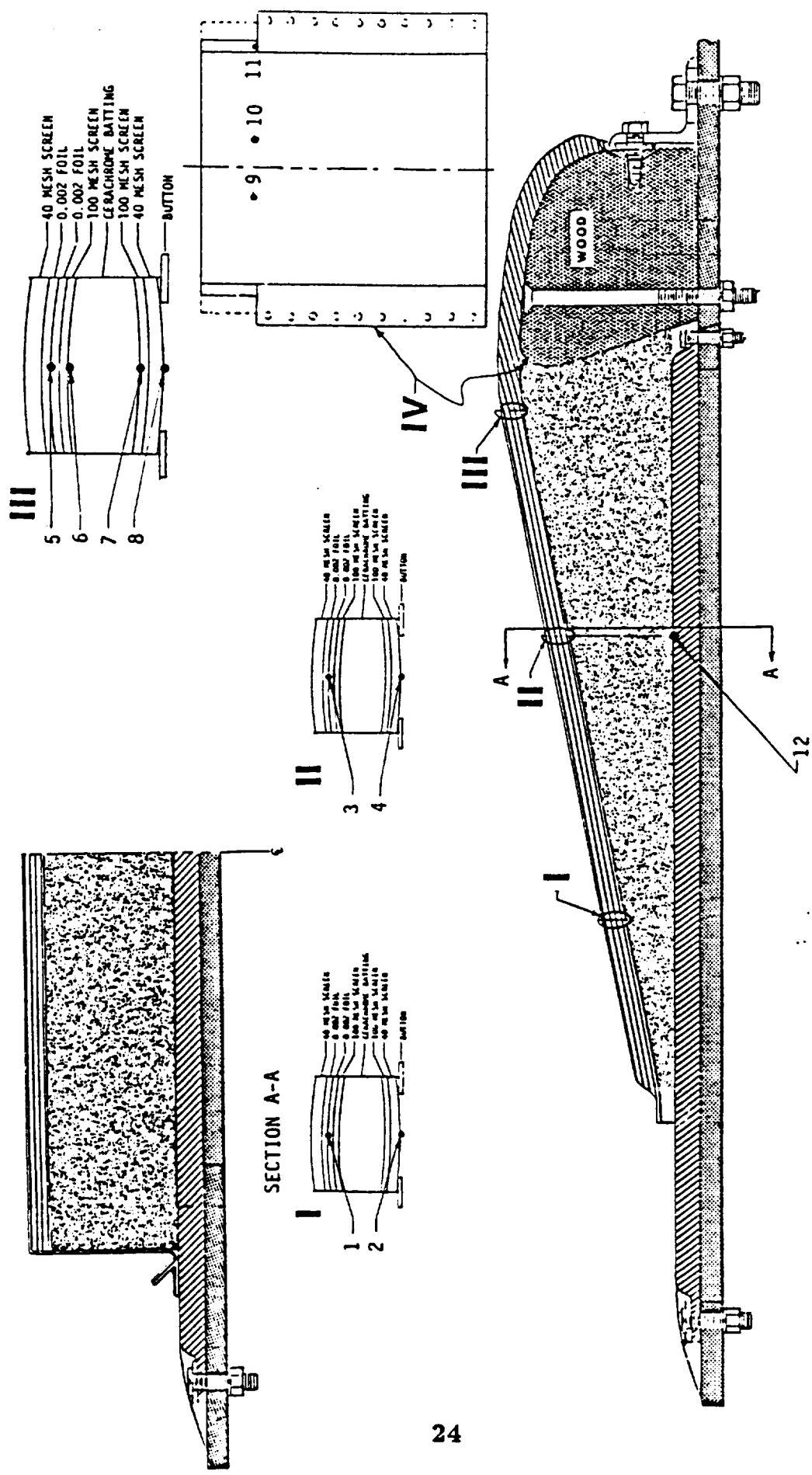
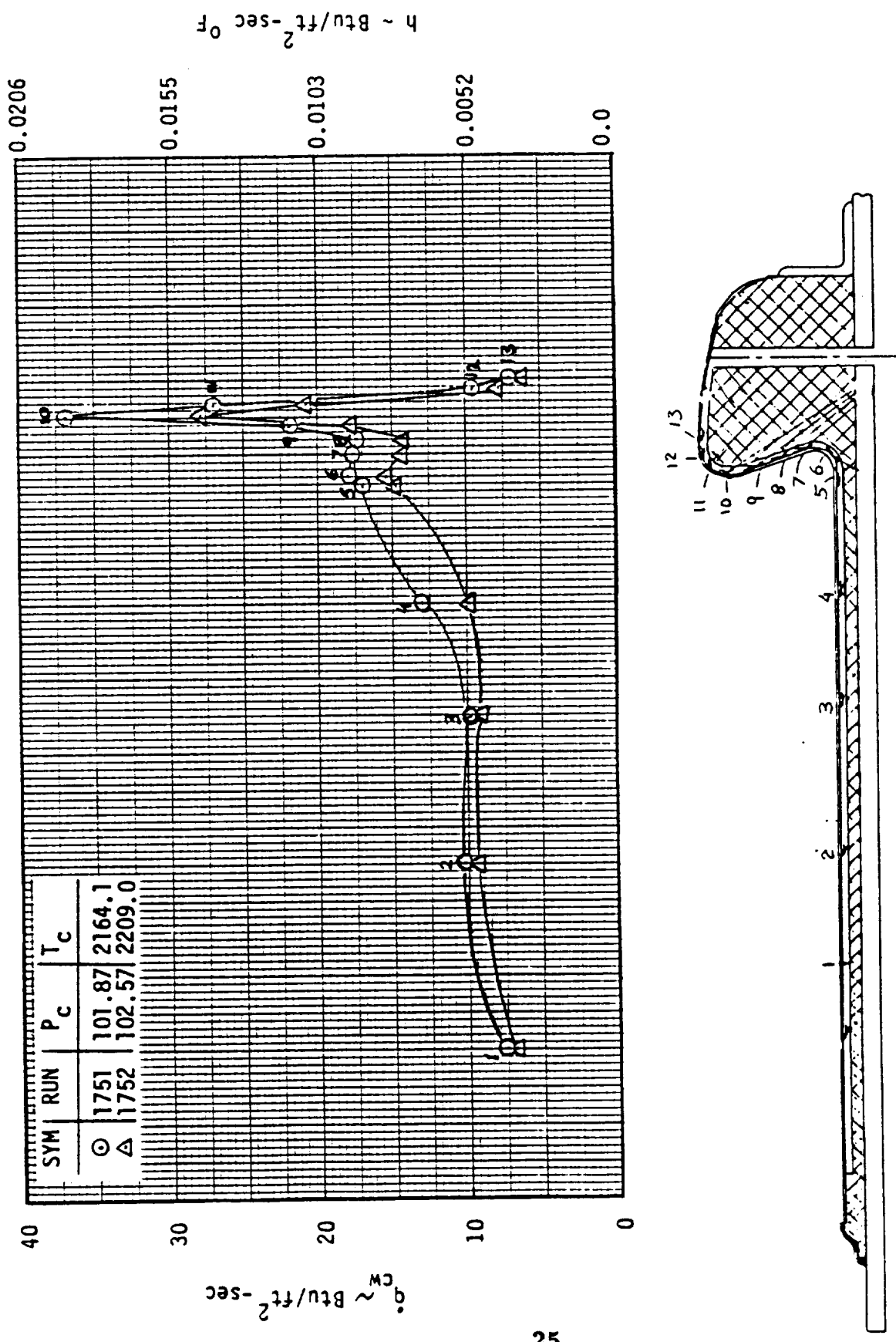


Figure 2.2.4: Model 5, STS-14 Full-Scale TPS

Figure 2.2.5: STS-13 Calibration ($\alpha = 0$)

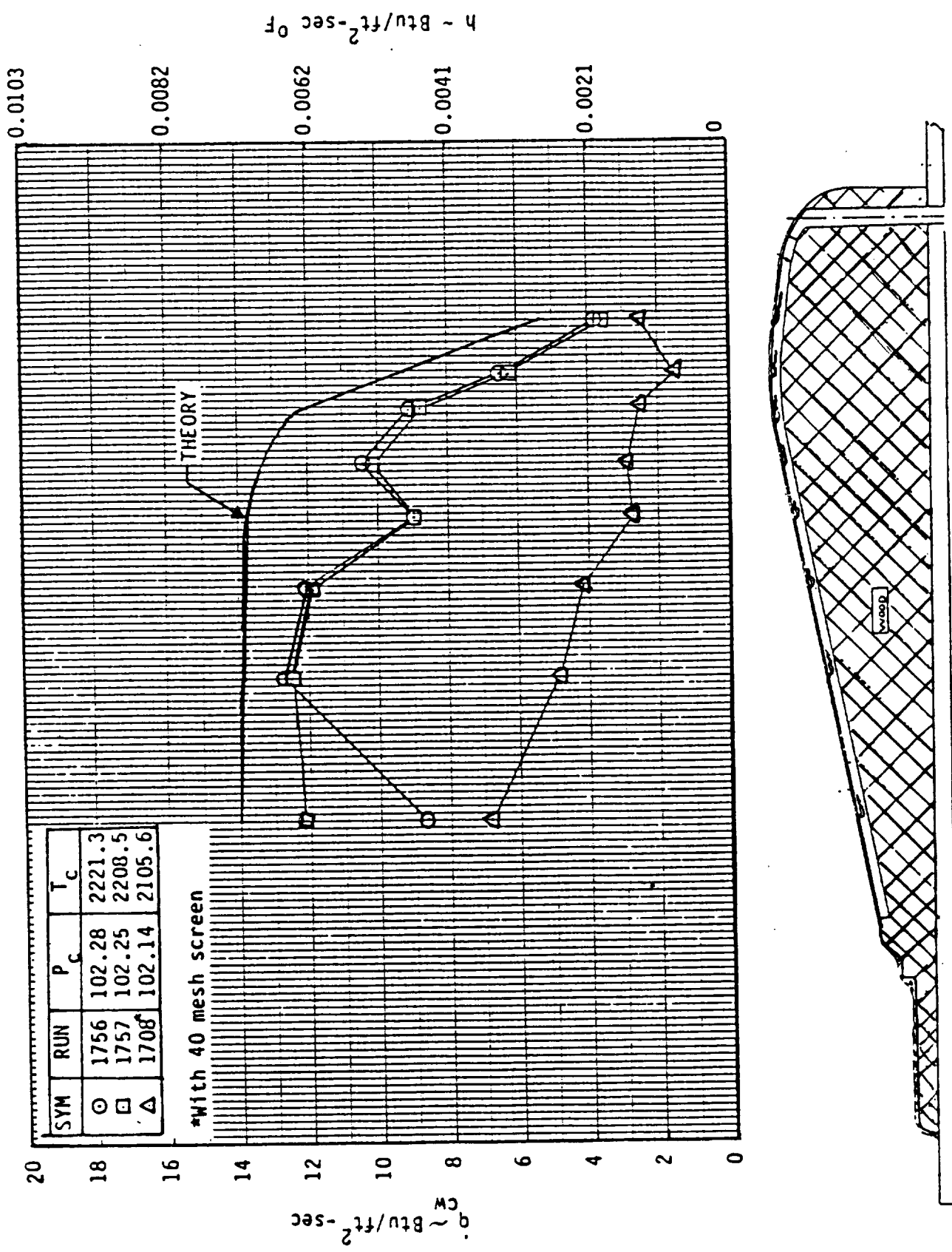


Figure 2.2.6: STS-14 Calibration ($\alpha = 0$)

STS-14

STS-13

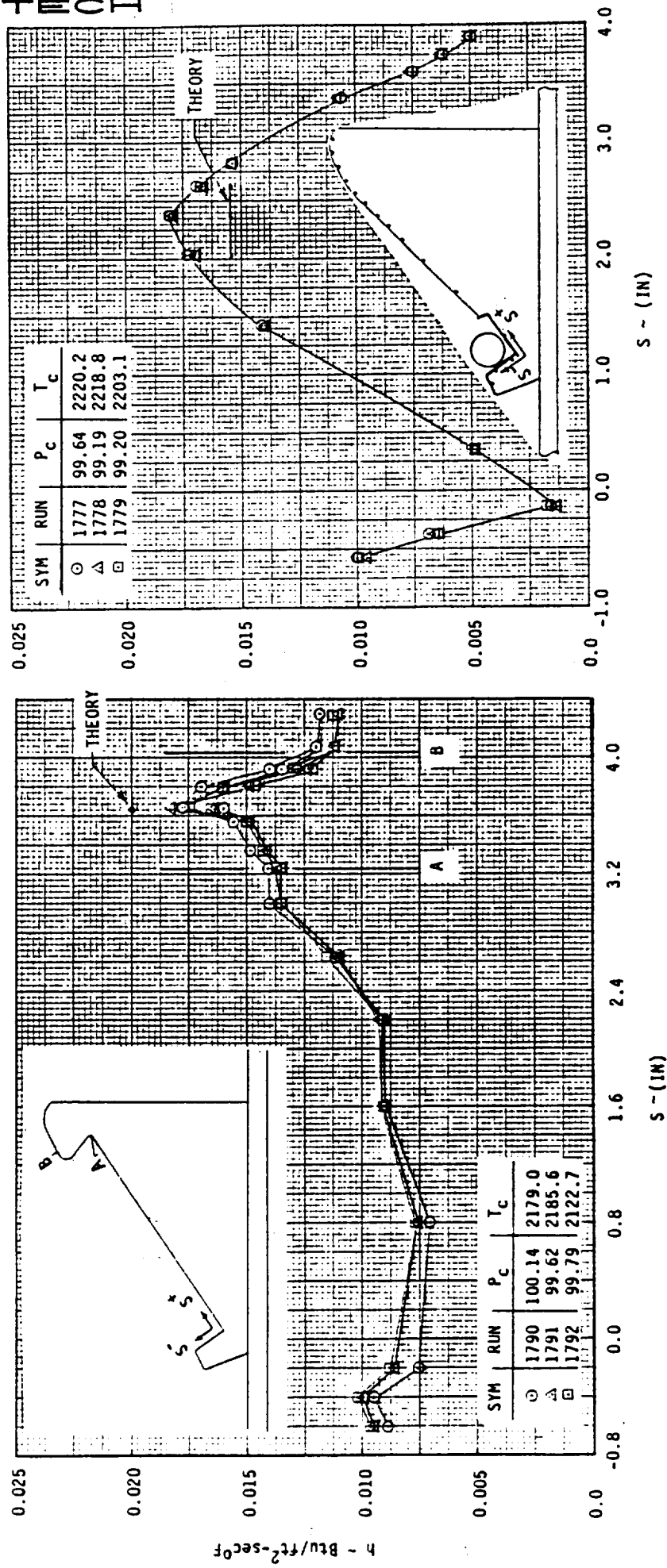


Figure 2.2.7: Calibration Model Data for 35 Degrees Angle-of-Attack Flow (0.30 Scale)

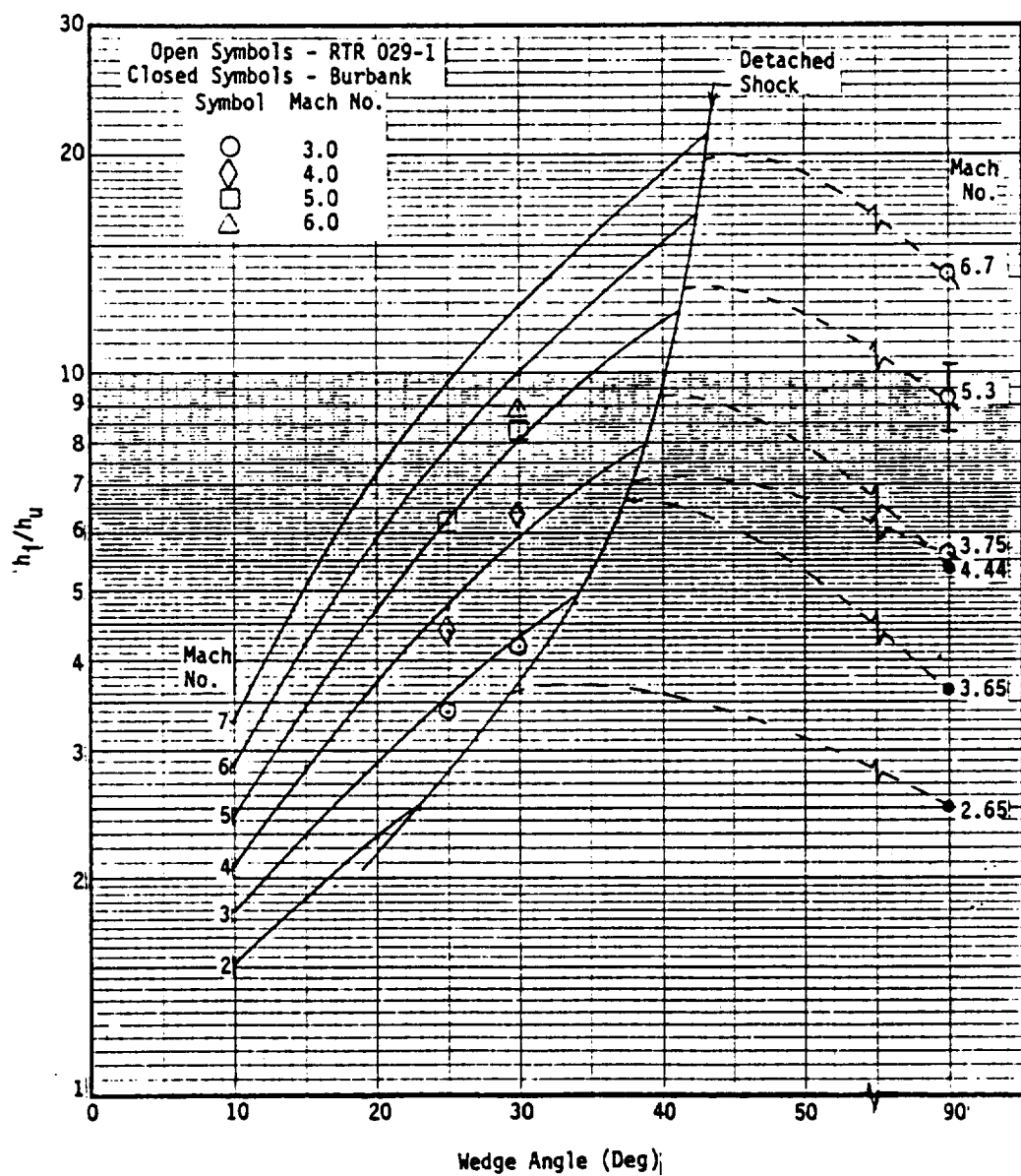


Figure 2.2.8: Theoretical Interference Factors and Data Versus Wedge Angle ($h_i/h_u = (P_i/P_u)^{.8}$) Where the Pressure Ratio is from Wedge Tables

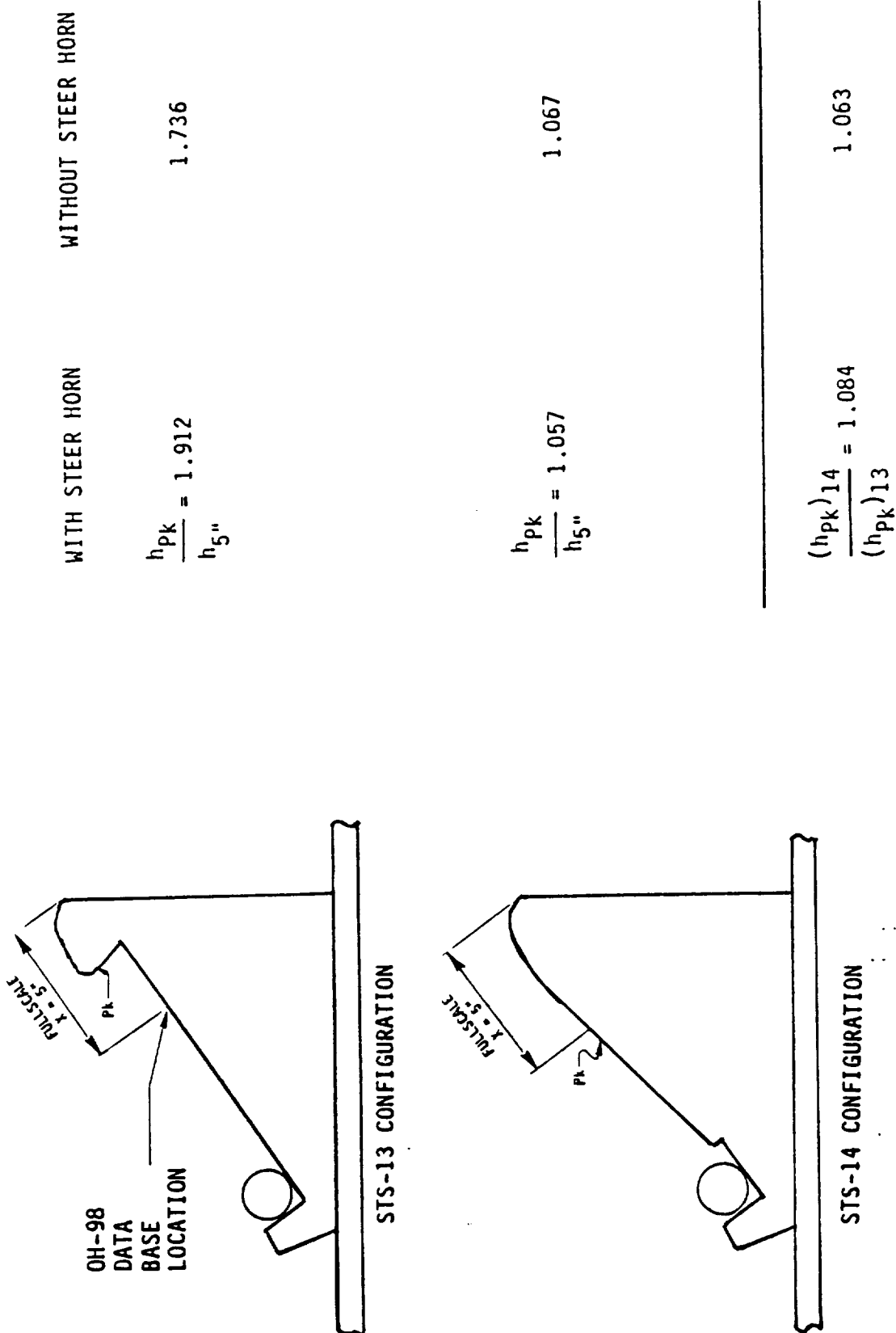


Figure 2.2.9: Heating Data Rates Summary

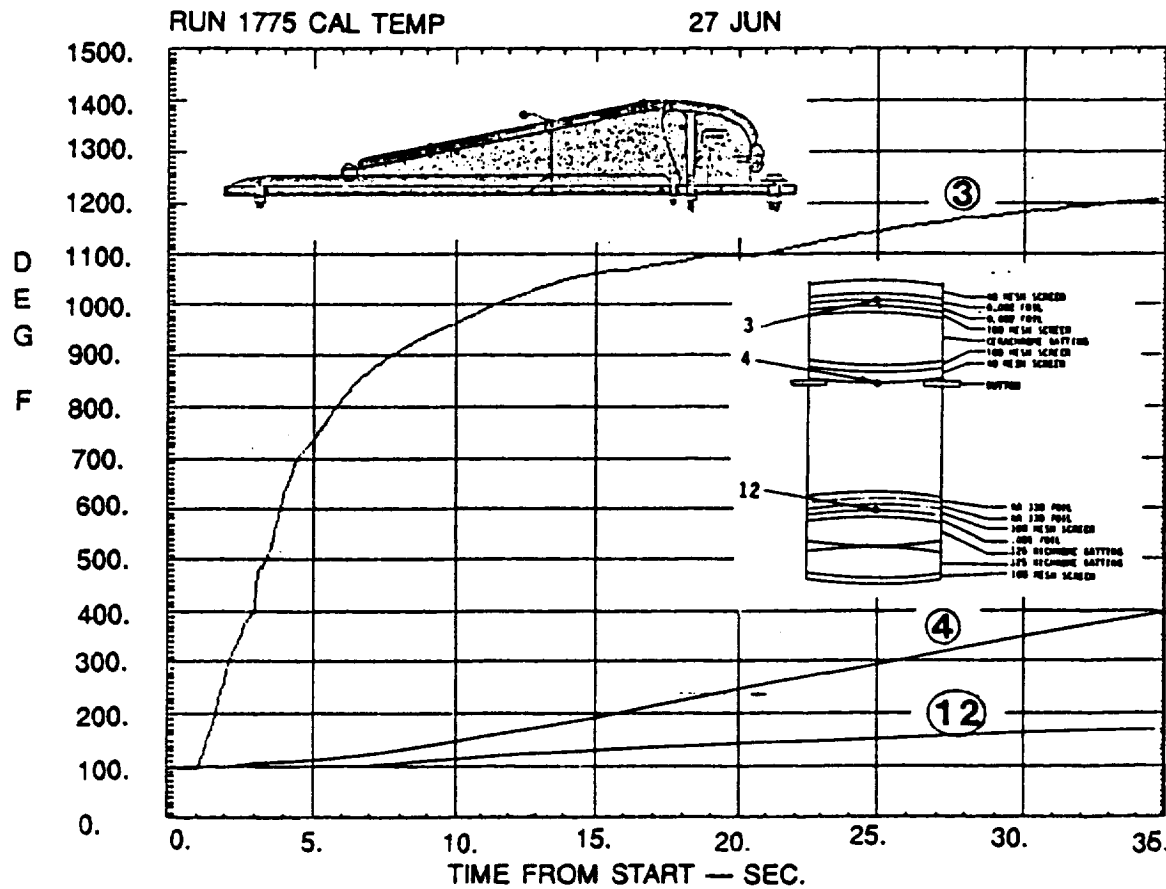
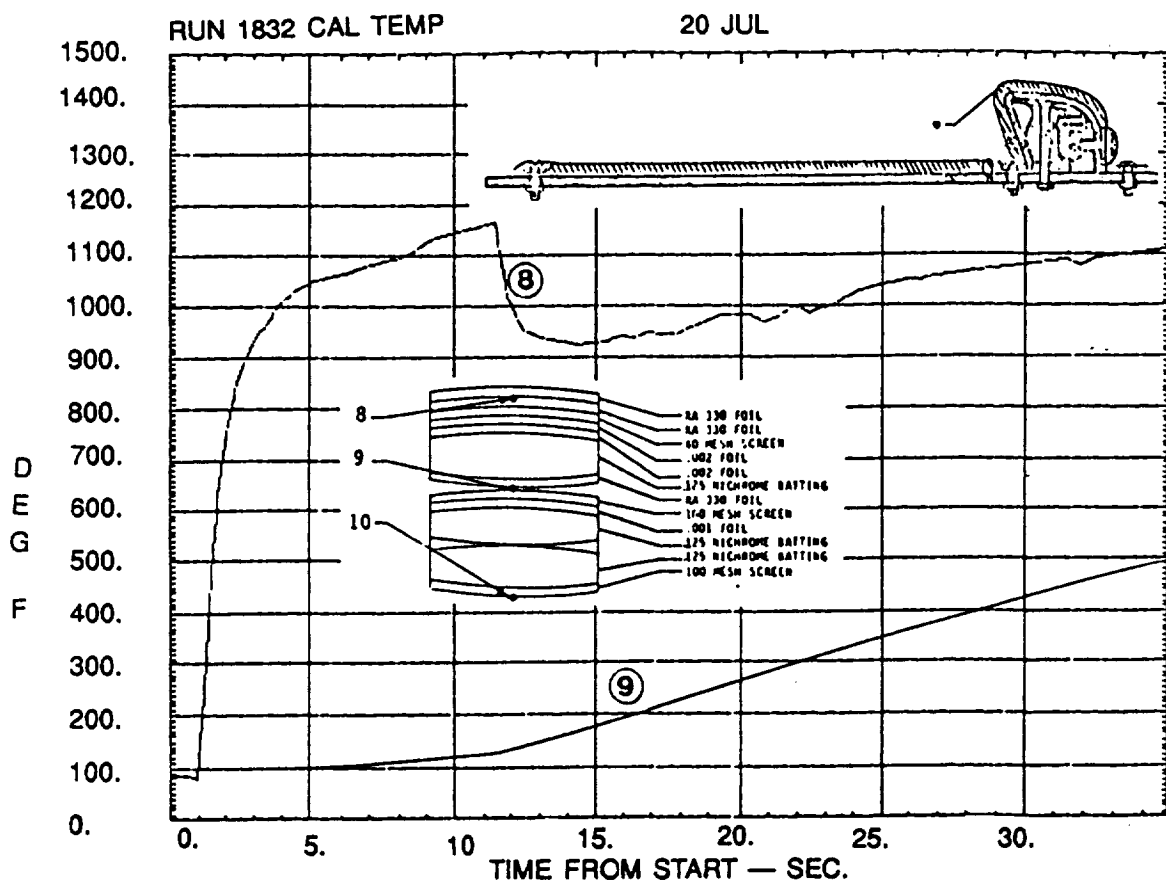


Figure 2.2.10: STS-13 and 14 Layered Insulation Temperature Response Near Peak Heating Location

Section 3

MATH MODEL

3.1 Aerothermal Models

An aerothermal math model for peak heating location on the SSME was developed to predict maximum heating to the SSME nozzle aft manifold. It was assumed that the impingement flow forms between the elevon and the body flap (see Section 2.1, Orbiter/Nozzle Tests). This flow expands to the orbiter base pressure. Figure 3.1.1 shows a comparison of orbiter base pressure with other entry vehicles which is included in the data base. This expanded flow impinges at a 40 deg angle and causes a parallel shock to be formed to the nozzle. This phenomenon has been included in the math model as swept cylinder flow. The effect of flight angle-of-attack versus orbiter base pressure is presented in Fig. 3.1.2. The primary data base used in the math model is the wind tunnel data taken from the OH-98 tests which characterizes heating rates to the nozzle by the standard h/h_{ref} parameter where h_{ref} is the heat transfer coefficient to a scaled 1.0 foot radius sphere. This data base is then nondimensionalized by replacing the h_{ref} for sphere with h_{cyl} for cylinder, using post orbiter shock entropy and prenozzle shock pressure from STS-3 correlation evaluated at 7.94 Mach Number, and a swept cylinder at $\alpha=40$ deg at nozzle exit radius. Figure 3.1.3 shows the OH-98 and OH-84B data used in the math model. Figure 3.1.4 shows the nozzle heating dependence on the angle of attack. The OH-98 data base was corrected for location effects using the HGF test data to get a ratio of peak to OH-98 data, and by using the OH-98 data to impose nonuniform flow effects. Figures 3.1.5 and 3.1.6 show the circumferential and axial SSME heating data used in REMTECH's math model. The line and equations in Fig. 3.1.5 provide the envelope of the data used in the math model. Tables 3.1.1 and 3.1.2 summarize REMTECH's aerothermal math model assumptions and results. Table 3.1.3 summarizes Rockwell's math model. The axial heating distribution of Rockwell data base is compared with REMTECH's correlation of OH-98 data as shown in Fig. 3.1.7. Table 3.1.4 shows a comparison of REMTECH and Rockwell math models heating rate predictions versus flight observations for STS 1 through 11.

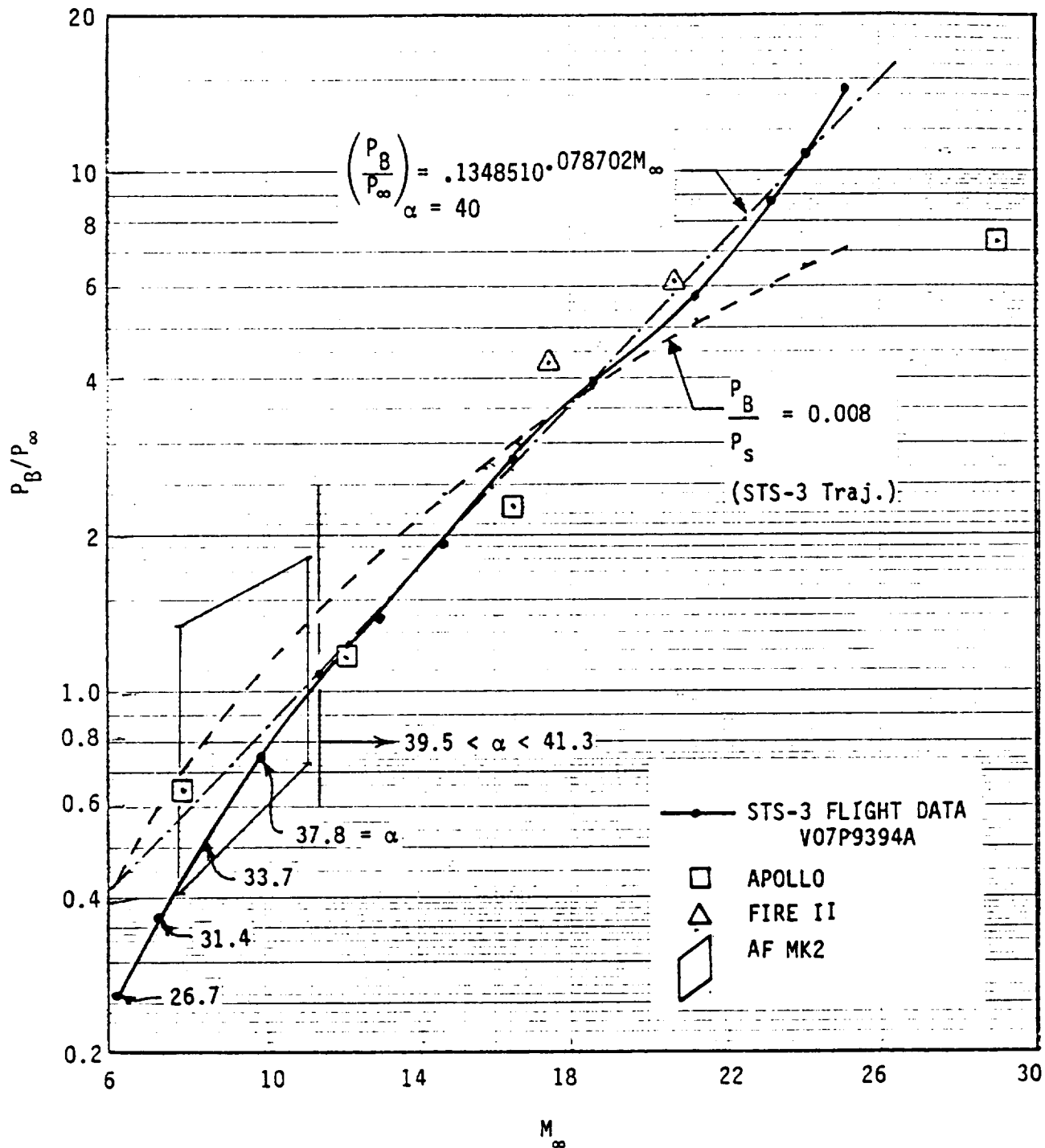


Figure 3.1.1: Comparison of Orbiter Base Pressures with Other Entry Vehicles

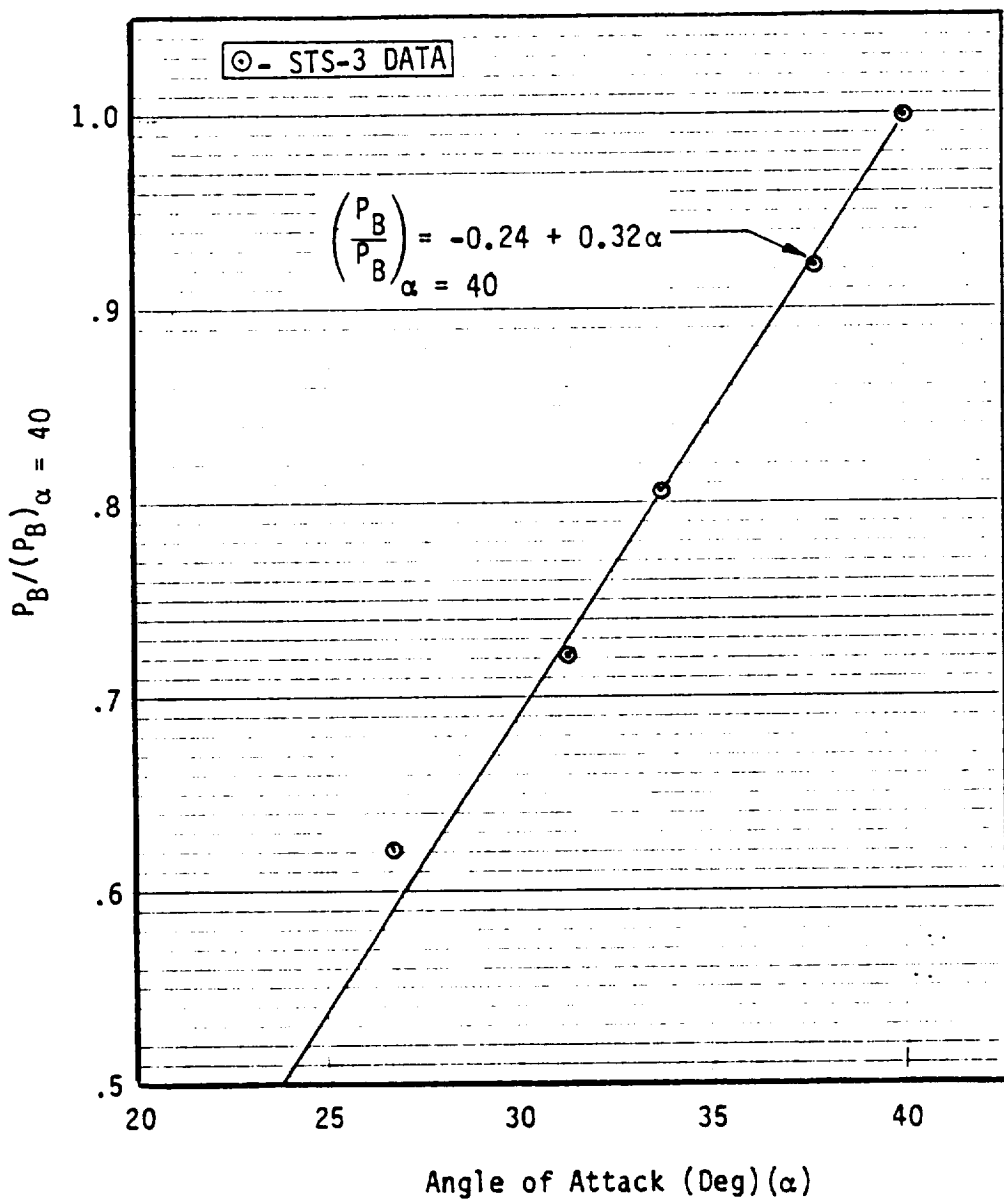
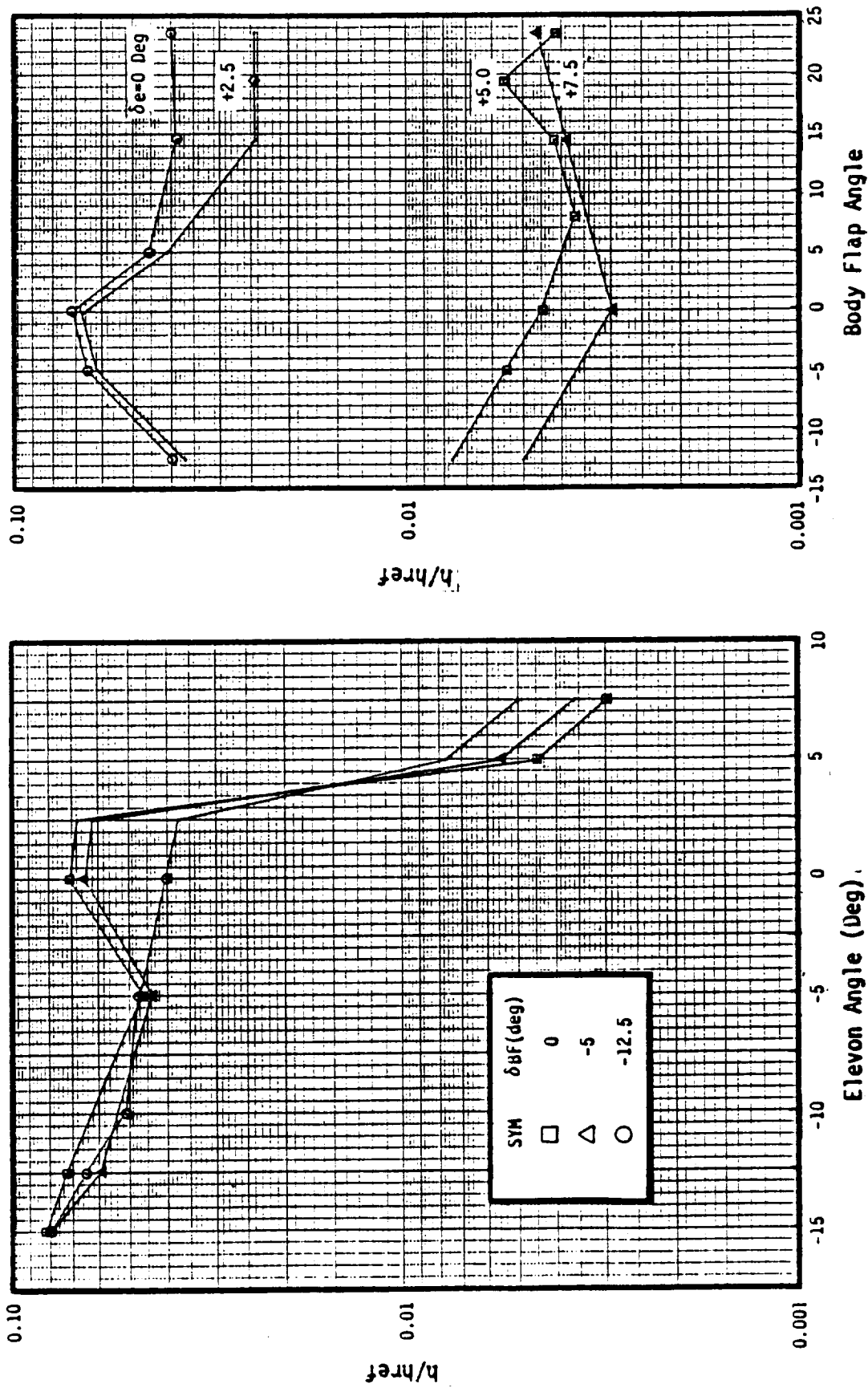


Figure 3.1.2: Angle-of-Attack Effect on Base Pressure



$Re_\infty/\text{ft} = 1.0 \times 10^6$, $\alpha = 40^\circ$, $x = 5$ inches, $\theta = 45^\circ$

Figure 3.1.3: Math Model Data (OH-98 and OH-84B)

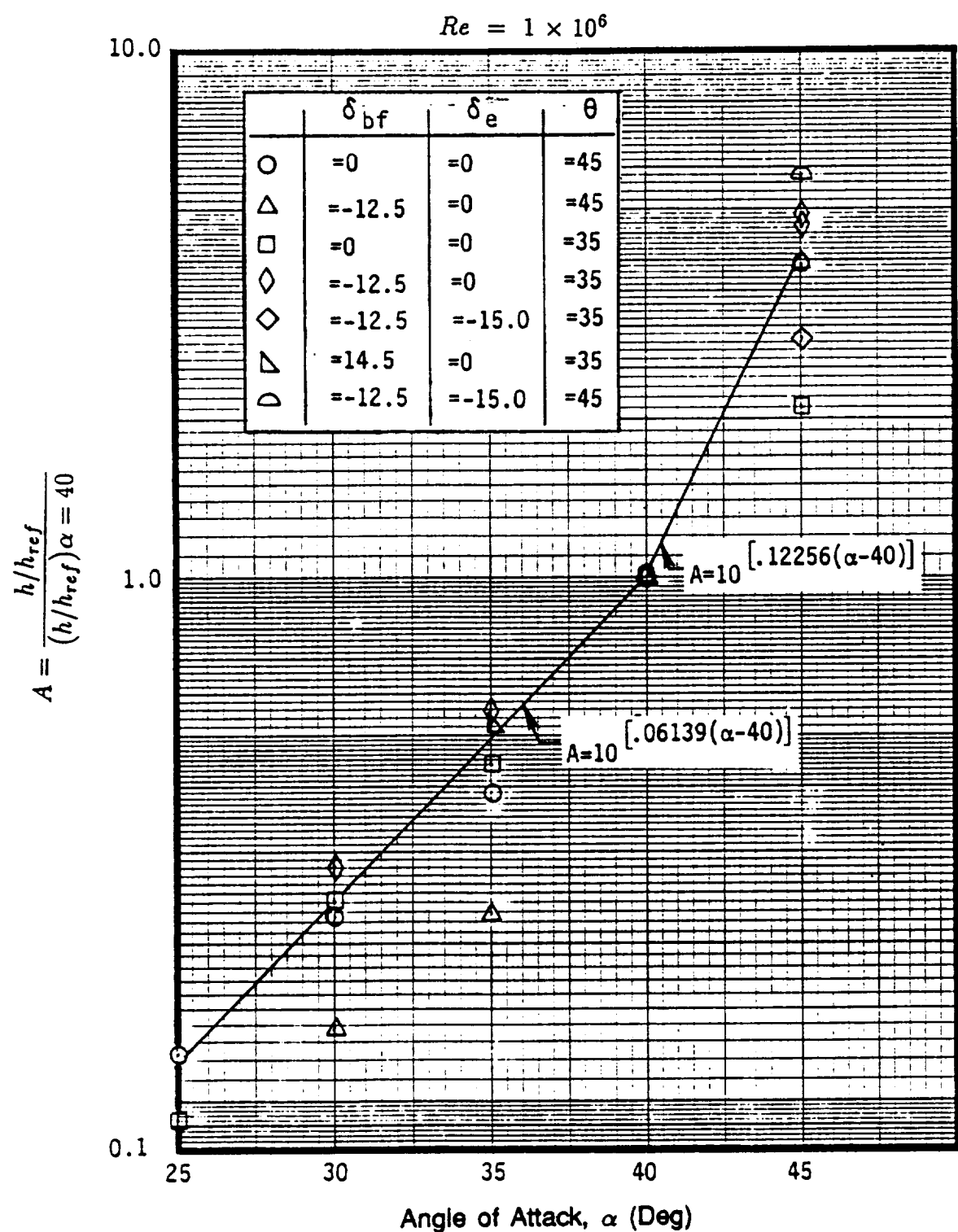


Figure 3.1.4: Correlation of Heating Dependence on Angle-of-Attack

$$\begin{aligned} 0 < \theta < 35 & \quad h/h_{pk} = 0.175 + 0.02357\theta \\ 35 < \theta < 45 & \quad h/h_{pk} = 1.0 \\ 45 < \theta < 55 & \quad h/h_{pk} = 3.9115 - 0.06470\theta \\ 55 < \theta < 90 & \quad h/h_{pk} = 0.5675 - 0.00390\theta \end{aligned}$$

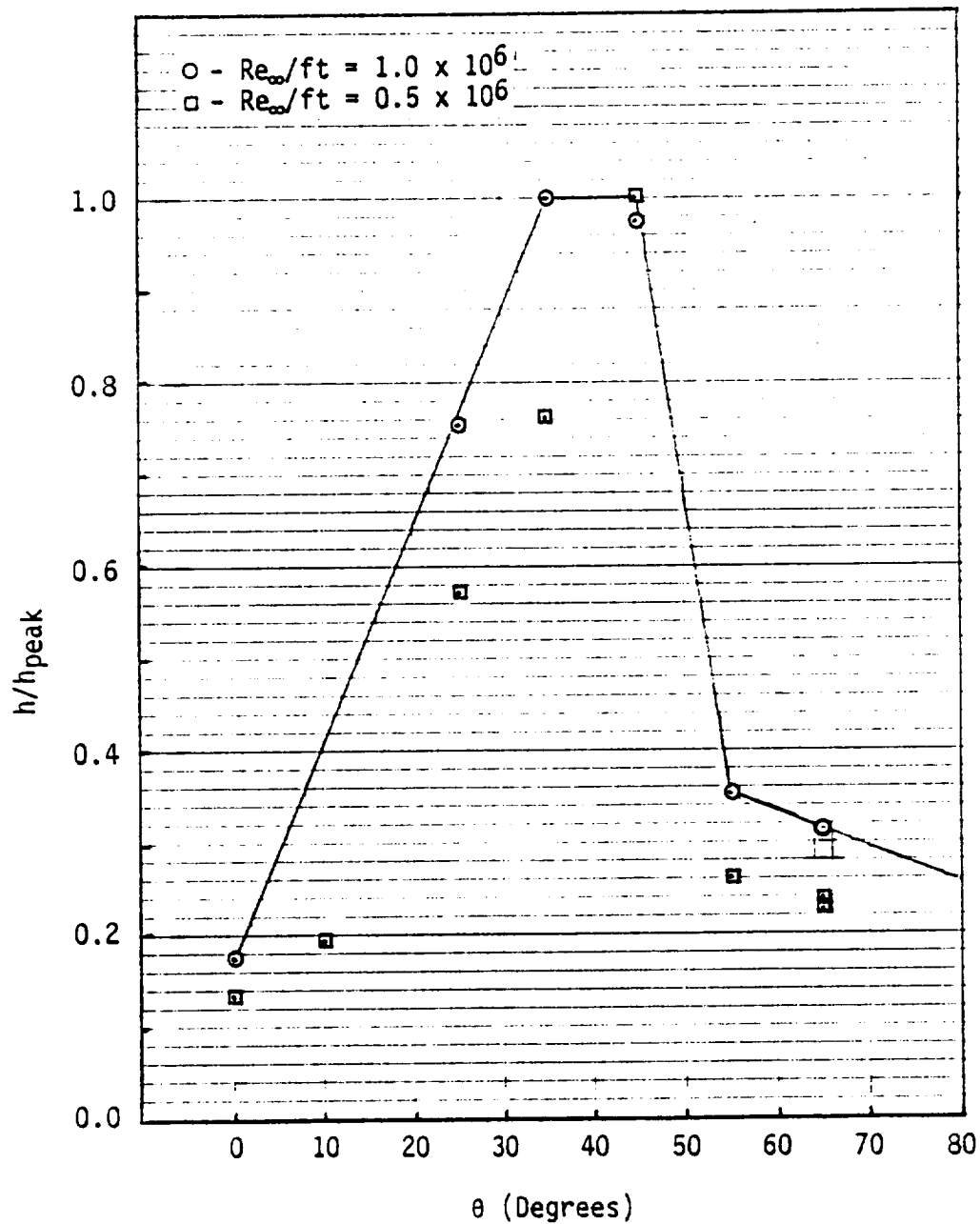


Figure 3.1.5: Envelope of Laminar Circumferential SSME Heating Data (OH-98 and OH-84B)

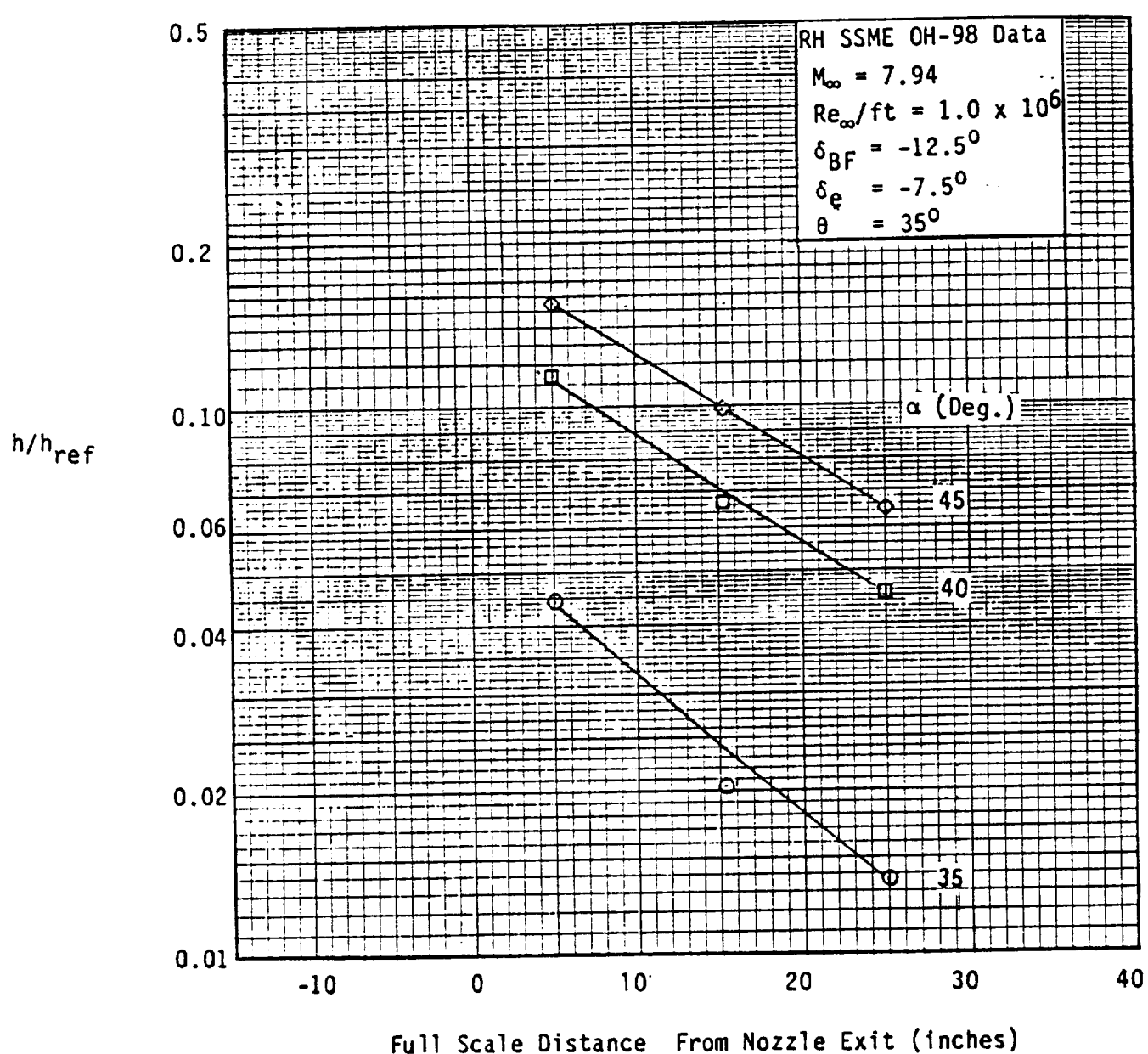


Figure 3.1.6: Axial Heating Distribution

Table 3.1.1: Aeroheating Math Model Components

NO.	MATH MODEL ASSUMPTIONS
1	ORBITER SHOCK ENTROPY
2	EXPAND FLOW TO BASE PRESSURE
3	BASE PRESSURE $(P_B/P_\infty)_{\alpha=40} = (0.13485) 10^{0.078702 M_\infty}$ $P_B/(P_B)_{\alpha=40} = -0.24 + 0.032\alpha$ STS-3 FLIGHT DATA CORRELATION
4	EXPANDED FLOW IMPINGES AT 40 DEGREES ANGLE
5	A SHOCK PARALLEL TO NOZZLE IS FORMED
6	SWEPT CYLINDER FLOW AND HEATING IS PRODUCED
7	WIND TUNNEL (OH-98) DATA IS NONDIMENSIONALIZED BY SWEPT CYLINDER HEATING
8	TURBULENT FLOW HEATING FACTORS ARE DERIVED FROM LAMINAR FACTORS USING PRESSURE INTERACTION THEORY
9	HGF TEST DATA PROVIDE THE FACTORS TO APPLY TO THE OH-98 DATA TO CALCULATE THE PEAK VALUE AND DISTRIBUTION
10	OH-98 AXIAL DISTRIBUTION USED TO ADJUST HGF DATA FOR NONUNIFORM APPROACH FLOW

Table 3.1.2: SSME Heating Calculation Procedure

NO.	CALCULATION PROCEDURE
1	DATA BASE (OH-98) @ $R_{e,\infty}/FT = 10^6$ a) LARGEST DATA BASE b) SOME DATA AT $R_{e,\infty}/FT = 3.7 \times 10^6$ TRANSITIONAL
2	DATA BASE NONDIMENSIONALIZATION a) REPLACE h_{ref} SPHERE WITH h_{cyl} CYLINDER USING (i) POST ORBITER SHOCK ENTROPY (ii) PRENOZZLE SHOCK PRESSURE FROM STS-3 CORRELATION EVALUATED AT $M_\infty = 7.94$ (iii) CYLINDER AT $\alpha = 40^\circ$ AND NOZZLE EXIT RADIUS
3	CORRECT OH-98 DATA FOR LOCATION EFFECTS a) USE HGF TEST DATA TO GET RATIO OF PEAK TO OH-98 DATA (1.85 FACTOR) b) USE OH-98 DATA TO IMPOSE NONUNIFORM FLOW EFFECTS (1.12 FACTOR)
4	APPLY TO FLIGHT a) CALCULATE POST ORBITER SHOCK ENTROPY b) CALCULATE BASE PRESSURE FROM STS-3 CORRELATION c) CALCULATE NOZZLE EDGE CONDITION BEHIND NOZZLE SHOCK ASSUMING A SWEPT CYLINDER AT $\alpha = 40^\circ$ d) CALCULATE LAMINAR AND TURBULENT SWEPT CYLINDER HEATING e) TRANSITION CRITERION: CYL. EDGE $R_{e,4} = 80,000 \rightarrow 160,000$
5	CALCULATE TURBULENT INTERFERENCE FACTORS $(h/h_{cyl})_T = (h/h_{cyl})_L^{.68}$ FROM PRESSURE INTERACTION THEORY
6	FINAL HEATING RESULTS $h_{pk} = (h/h_{ref})(h_{ref}/h_{cyl})^n \text{ tunnel } \bullet h_{cyl} \bullet (1.85) \bullet (1.12) \bullet \overbrace{(0.67)}^{\text{THERMAL PANNEL FACTOR (JUNE 85)}} \\ \text{WHERE } n = 1 \text{ FOR Laminar, } 0.68 \text{ FOR TURBULENT}$

Table 3.1.3: Rockwell Math Model

NO.	ASSUMPTIONS AND CALCULATION PROCEDURE
1	DATA BASE OH-98 AND OH-84B a) $h/h_{ref} = f(\alpha, \delta_e, \delta_{BF}, Re/ft, \theta)$ FOR THE NOZZLE WITH HATBAND b) VOIDS IN THE MATRIX FILLED IN BY INTERPOLATION AND ENGINEERING JUDGEMENT.
2	REAL GAS EFFECTS ON PRANDTL-MEYER ANGLE ACCOUNTED FOR BY $\delta_e = (\delta_e)_{actual} + 3.5$.
3	PROTUBERANCE FACTOR FOR AFT MANIFOLD 1.6 BASED ON BURBANK AND IH51C TEST DATA.
4	FLIGHT SCALING FACTOR OF 1.53 USED ON STS-13 CONFIGURATION TO MATCH FLIGHT DAMAGE ASSUMING 20 Btu/sqft.-sec. IS DAMAGE THRESHOLD.
5	THE RAMP FOR STS-14 CONFIGURATION REDUCES THE HEATING BY A FACTOR OF 2.0 BASED ON THE RATIO OF SMOOTH (LEFT) TO HATBAND (RIGHT) NOZZLE DATA RATIOS.
6	THE CIRCUMFERENTIAL DISTRIBUTION WAS SHIFTED UPWARD FOUR DEGREES TO AGREE WITH FLIGHT DAMAGE.
7	$q/q_{stag} = h/h_{ref}$ IS ASSUMED TO SCALE FOR LAMINAR AND TURBULENT FLOW FROM TUNNEL FLIGHT.
8	$\dot{q} = \left(\dot{q}_{ref} \right)_{sphere} \bullet \left(\frac{h}{h_{ref}} \right)_{Tunnel} \bullet 1.53 \bullet 1.6 \bullet \widehat{0.67}$ <u>THERMAL PANEL FACTOR (JUNE 85)</u>

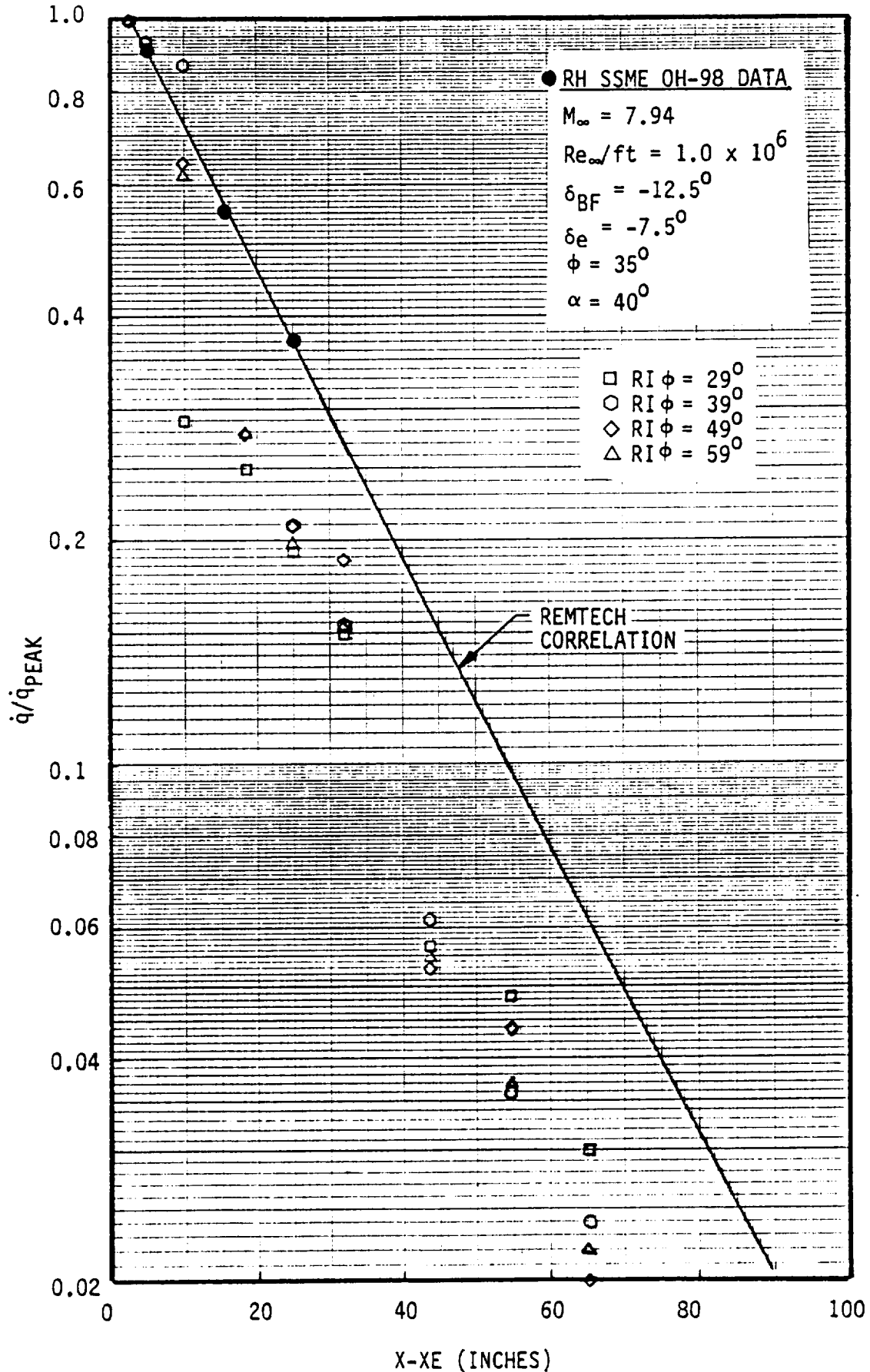


Figure 3.1.7: Axial Heating Distribution

Table 3.1.4: REMTECH and Rockwell Math Model Prediction vs. Flight Data

FLIGHT (STS)	REMTECH \dot{Q}_{MAX}	RI \dot{Q}_{MAX}	DAMAGE
1	13.1	8.4	NONE NOTED
2	12.2	9.2	NONE NOTED
3	10.9	13.2	NONE NOTED
4	21.1	L 15.5	ME2 - OUTER SCREEN MELTED ONLY ME3 - MELTED THROUGH INSULATION LOCALLY, MANIFOLD EXPOSED
5	L 12.1	9.6	ME3 - OUTER SCREEN & FOIL MELTED
6	6.9	9.6	ME2 - 3.4" HOLE THROUGH SCREEN, FOIL & BATTING ME3 - ONE AREA UNKNOWN EXTENT
7	17.4	L 9.6	ME2 - NO DAMAGE ME3 - NUMEROUS AREAS OF SCREEN DAMAGE, 3.4" OR LESS
8	17.6	L 15.2	ME2 - MELTING AT 5 LOCATIONS; THROUGH SCREEN & FOIL IN WORST CASE ME3 - MELTING AT 5 LOCATIONS; THROUGH SCREEN, FOIL & INSULATION
9	21.2	H 31.7	ME2 - MELTING OF SCREEN & FOIL ME3 - MELTING OF SCREEN & FOIL
11	22.4	21.6	ME2 - MELTING OF SCREEN, FOIL & INSULATION; MANIFOLD EXPOSED ME3 - MELTING OF SCREEN & FOIL

L - Low
H - High

3.2 Thermal Analyses Models

Thermal models of the STS-1, STS13 and STS14 (current) aft manifold and aft panel were developed to predict TPS thermal response to the design environment. These models were developed using two basic assumptions: first, the idea that most heat to the TPS is rejected through radiation and that only a small fraction of the total load is stored within the TPS and aft manifold; second, the heating distributions are such that lateral conduction effects can be neglected and that a one-dimensional conduction model will yield reasonably accurate, although somewhat conservative, temperature distributions through the TPS.

Radiation models were developed for the above three TPS configurations. These models determined the radiation interchange between surfaces which can "see" each other, considering reflections and direct irradiation and assuming that the surfaces are grey and diffuse (Table 3.2.1). Radiation interchange factors between each surface and deep space were computed. Interchange factors to deep space are shown in Fig. 3.2.1.

These results were used to determine surface temperature response of three TPS configurations using surface emissivity of 0.4, 0.625 and 0.9 for various STS-9, 13 and 14 heating trajectories. An example of these results for the baseline STS-14 AOA with uncertainties heating rate with $\epsilon=0.90$ is shown in Fig. 3.2.2. It can be concluded from Figs. 3.2.2, 3.2.3 and 3.2.4 that surface temperatures are only slightly lower than radiation equilibrium temperature.

The primary damage to the TPS occurs in the corner of the area where the ramp and manifold intersect, as has been observed in previous flights; hence a three-dimensional thermal model of this area was developed using the same two basic assumptions as described previously. The majority of the nodes were concentrated at the corner location (Fig. 3.2.5).

A radiation model was developed for this TPS configuration. A view factor code was written using finite difference technique to calculate the view factors. For the surfaces which are close together, the view factors were calculated using view factor algebra and handbook figures. These view factors were used to determine the radiation interchange between surfaces which can "see" each other, considering reflections and direct irradiation and assuming that the surfaces are grey and diffuse. Radiation interchange factors between each surface and deep space were computed.

One-dimensional thermal models of the different flight TPS configurations were analyzed using the EXITS (Ref. 6) thermal analyzer code to determine the manifold temperature. Table 3.2.2 shows the assumptions which were used in the

Table 3.2.1: Radiation Equilibrium Temperature Analysis

NO.	ASSUMPTIONS AND CALCULATION PROCEDURES
1	RADIATION VIEW FACTORS FOR 15 TO 20 SURFACES, TO DEEP SPACE AND TO EACH OTHER COMPUTED
2	RADIATION INTERCHANGE FACTORS COMPUTED <ul style="list-style-type: none"> a) GREY BODY ASSUMPTION ($\alpha_\lambda \cdot \epsilon_\lambda$) b) DIFFUSE SURFACES ASSUMED c) DEEP SPACE; $\epsilon = 1.0$, $T = 0^\circ R$
3	NO THERMAL ENERGY STORED (ANALYSIS SLIGHTLY CONSERVATIVE)
4	STS-14 (AERODYNAMIC FAIRING) ELIMINATES RADIATION TRAPPING AND INCREASES VIEW FACTORS

analysis.

The thermal models were verified using the Hot Gas Facility (HGF) data (Ref. 5). As shown in Fig. 3.2.6, the response of the surface shows good agreement with the measured data, although the initial response is somewhat slow. Response of node No. 6 position is somewhat faster than the data indicate, suggesting that radiation between layers in the foil-screen systems may be important but not accounted for. Agreement of thermocouple No. 7 is good; however, backside heating may have affected the data. Node No. 8 shows higher temperatures than node No. 7, suggesting heating from gases entering leading edge of wedge.

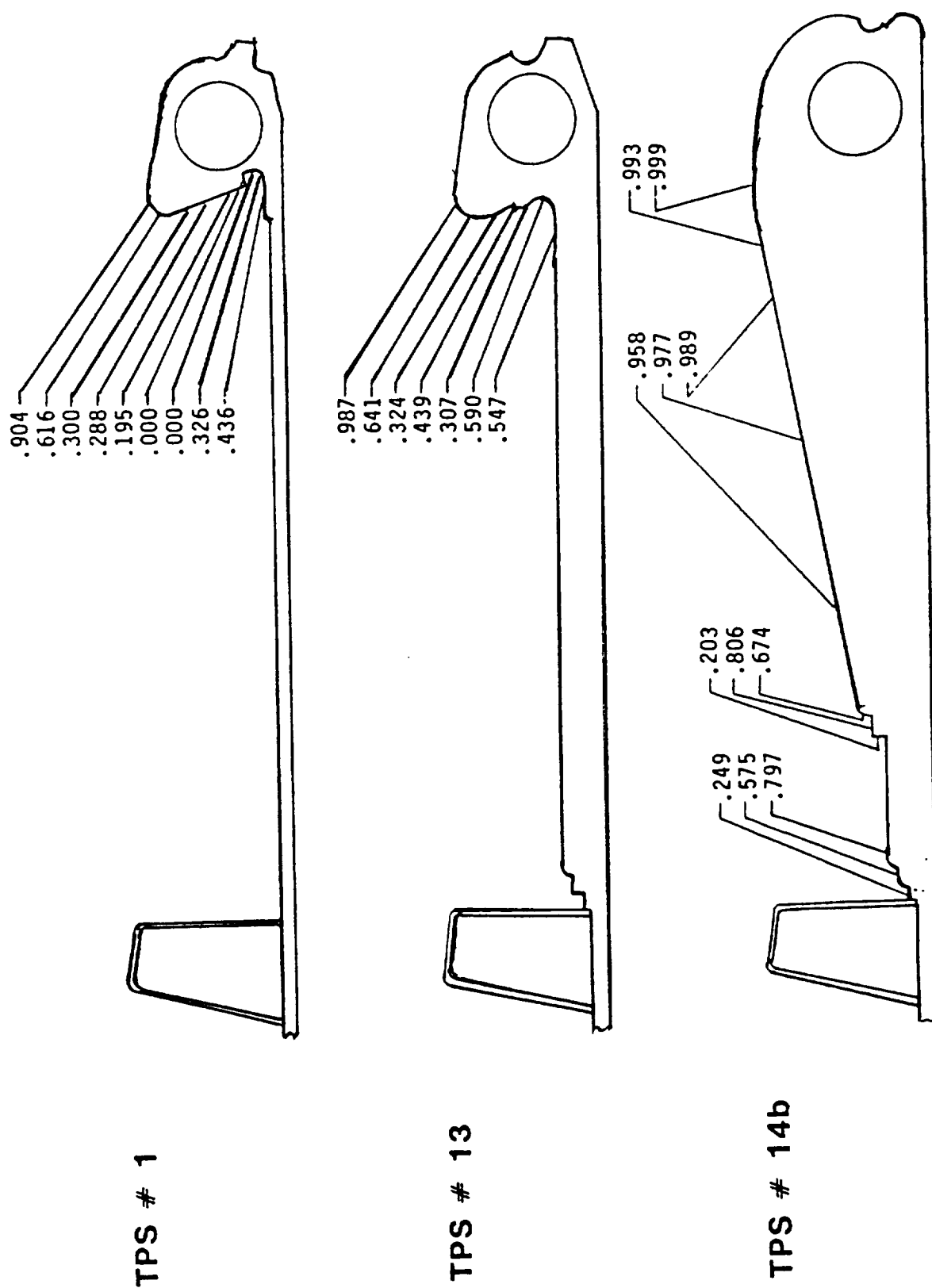


Figure 3.2.1: SSME Aft Manifold View Factor Distribution to Deep Space

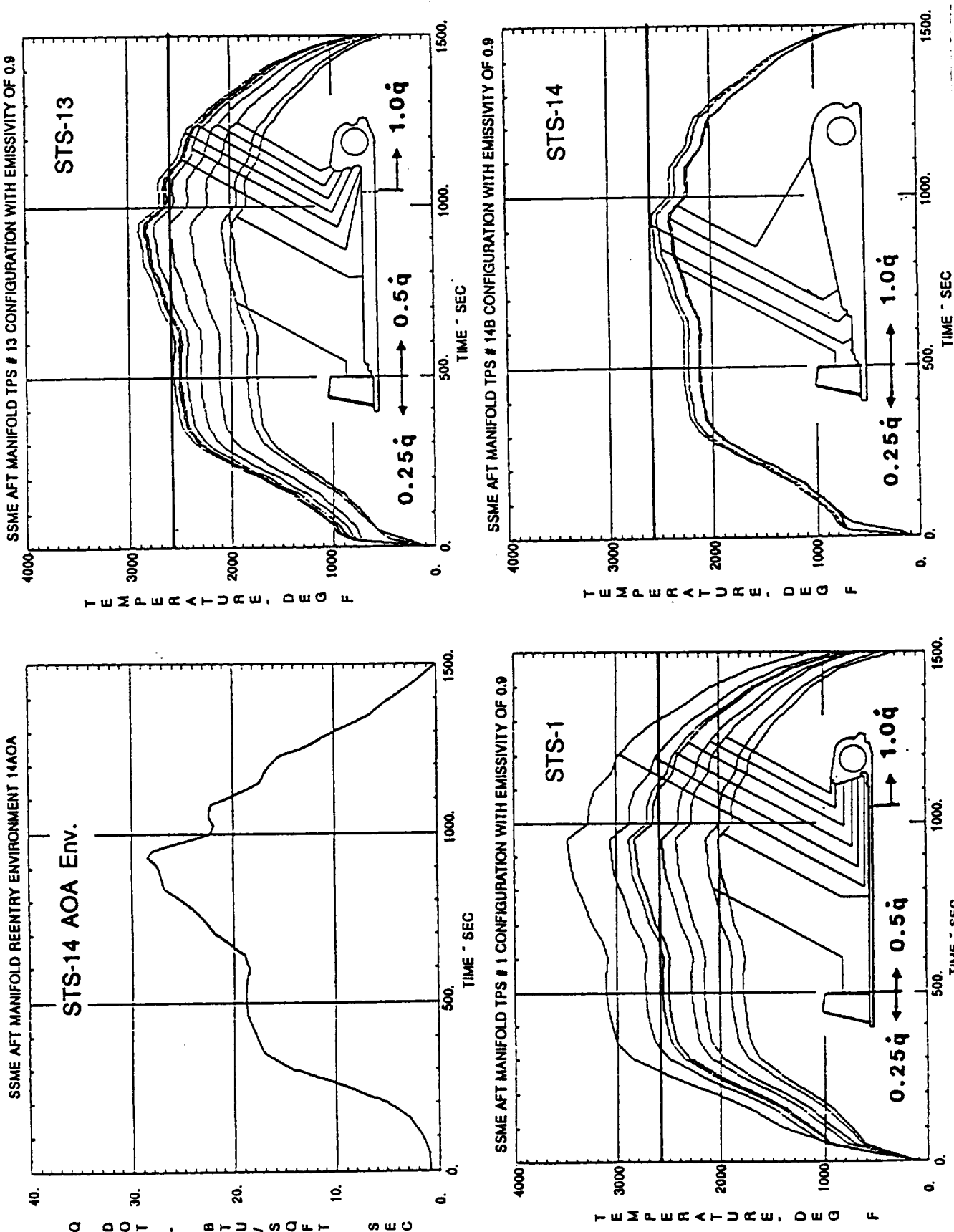


Figure 3.2.2: TPS Surface Distribution with STS-14 AOA Heating Rate

STS-14 SSME NOZZLE EOM ENVIRONMENT 1-D THERMAL MODEL

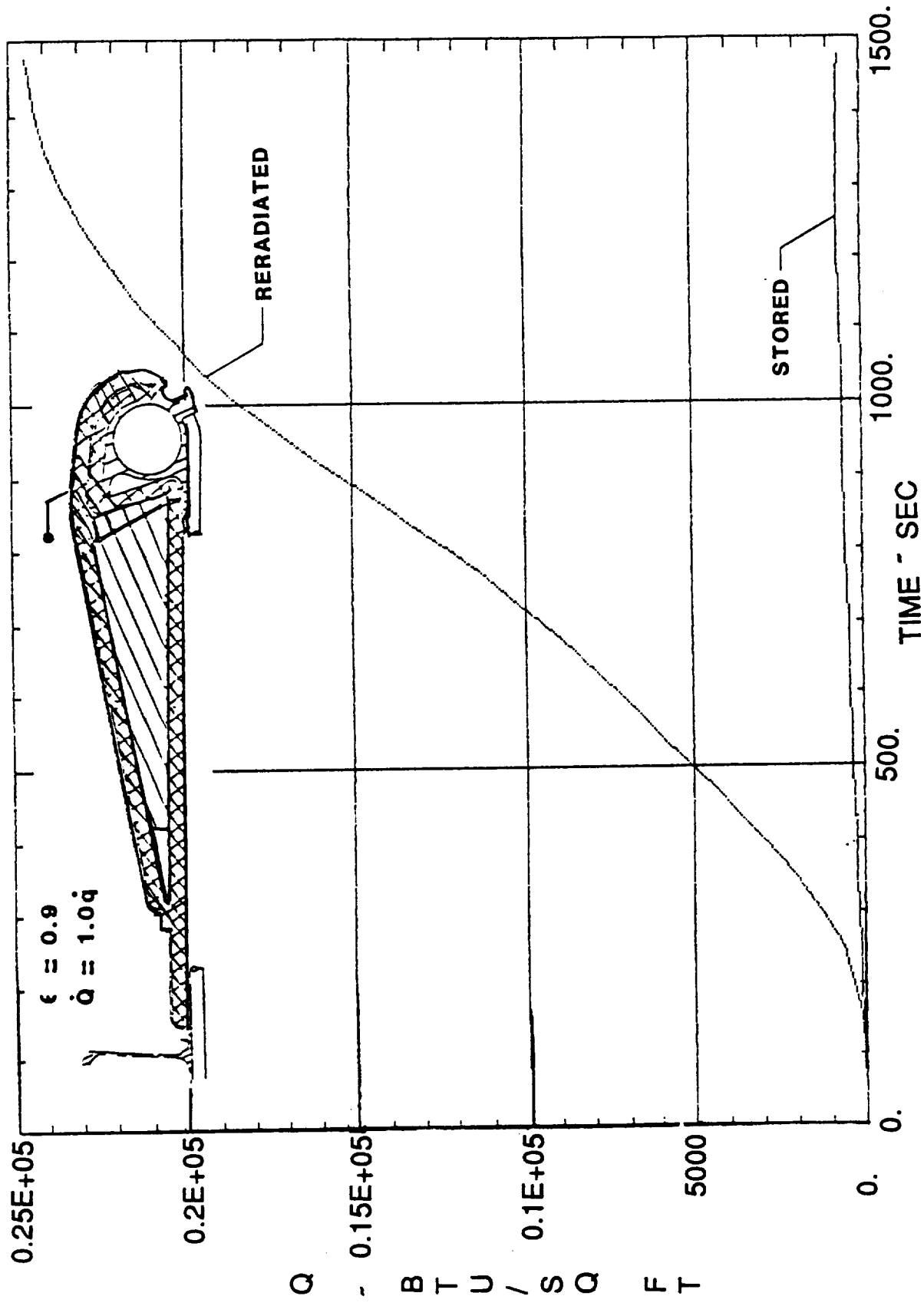


Figure 3.2.3: Comparison of Stored vs. Reradiated Load

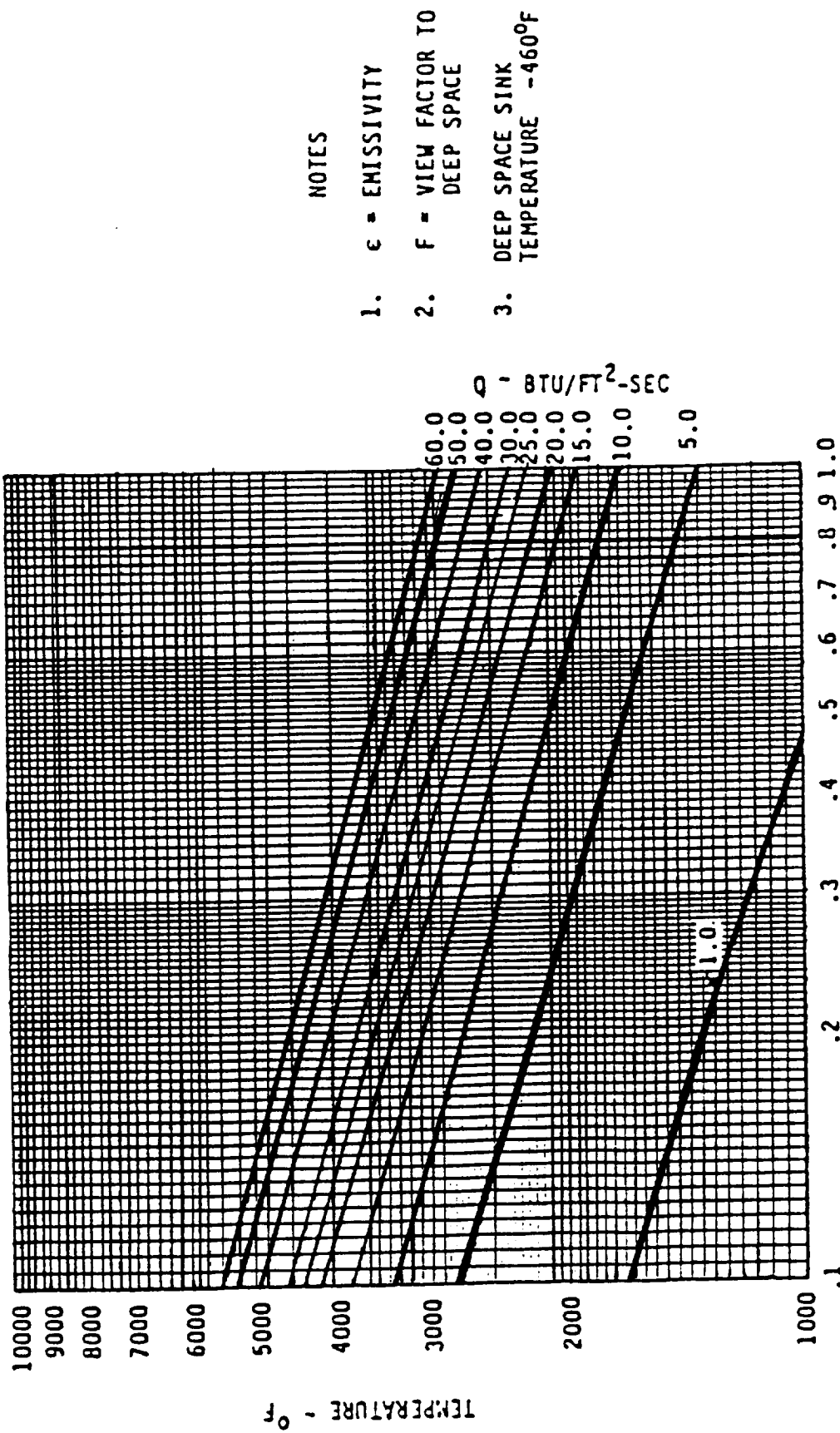


Figure 3.2.4: Radiation Equilibrium Temperature

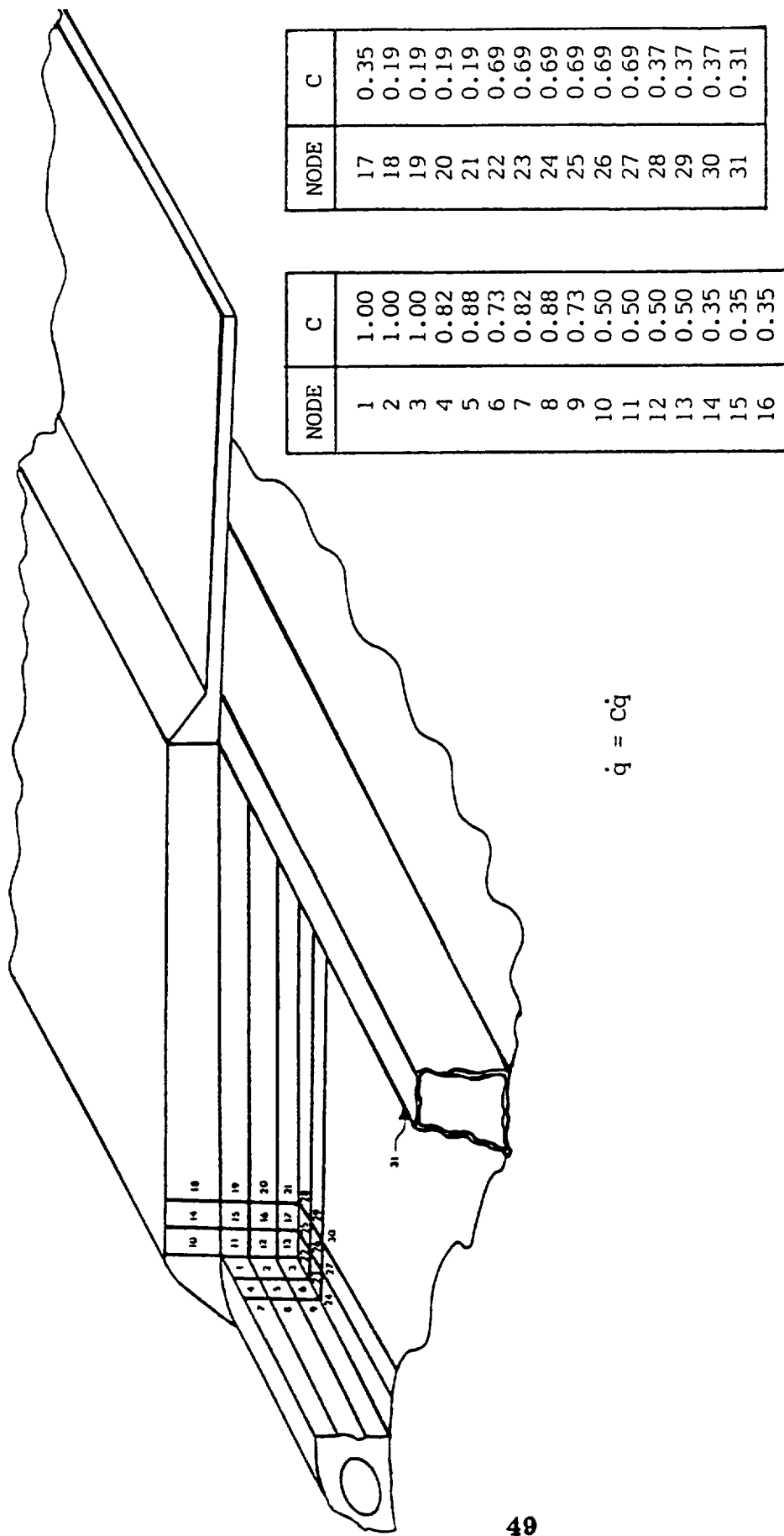


Figure 3.2.5: Heating Distribution

Table 3.2.2: One-Dimensional Thermal Analysis

NO.	ASSUMPTIONS
1	PERFECT CONTACT ASSUMED BETWEEN LAYERS
2	VIEW FACTORS TO DEEP SPACE ≈ 1 . FOR AERODYNAMIC FAIRING
3	QUILTED MESH-FOIL-CERACHROME-MESH PLACED OVER EXISTING TPS AND CERACHROME WEDGE
4	CASES CONSIDERED: HEATING FACTOR $C = .65 \& 1.0$ $\epsilon = .625 \& .900$
5	VIEW FACTOR TO DEEP SPACE ≈ 1.0

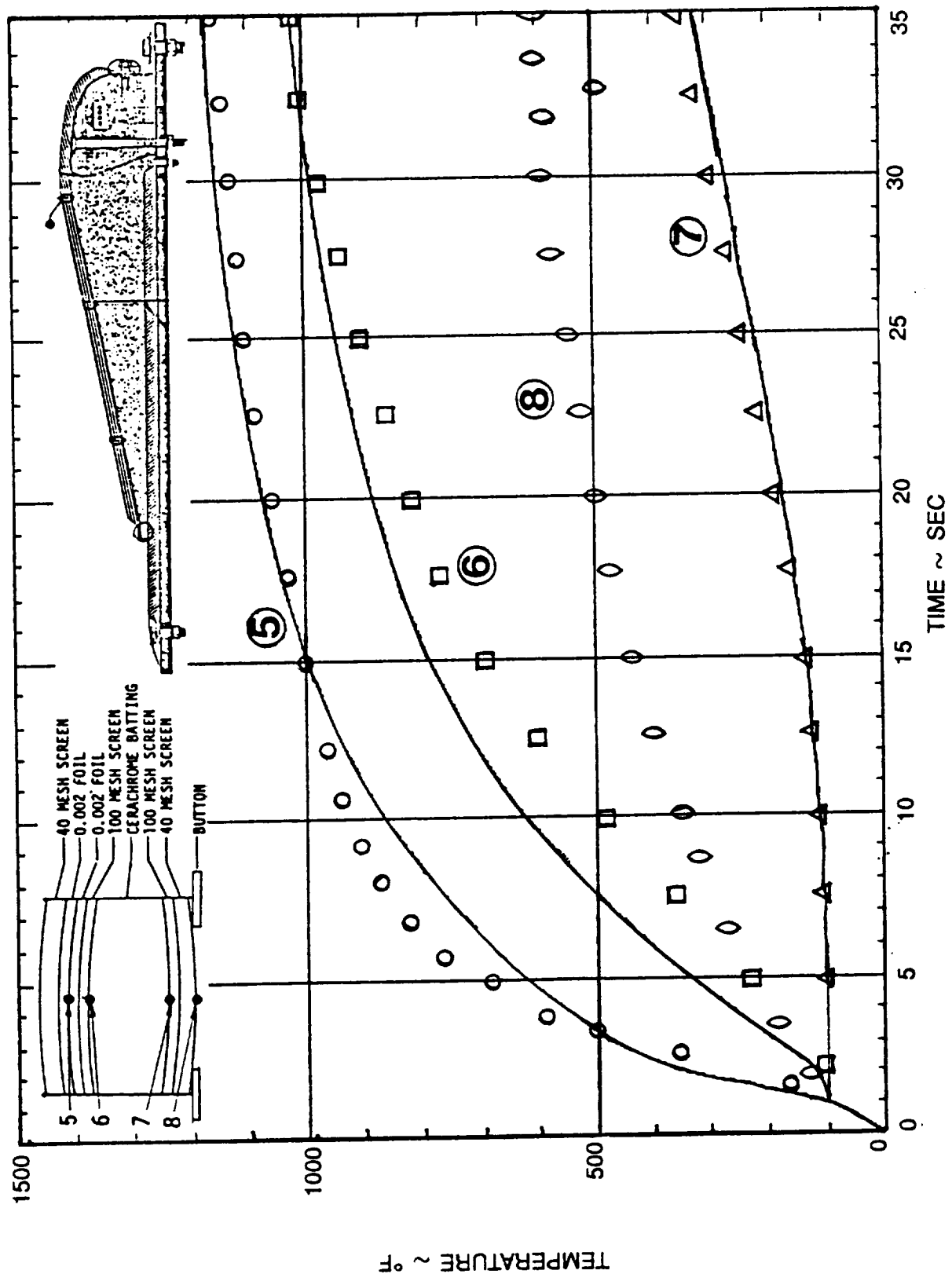


Figure 3.2.6: One-Dimensional Model Temperature Response Comparison with HGF Data

Section 4

FLIGHT PREDICTIONS

Thermal damage to the SSME aft manifold TPS has been observed for flights STS-8 through STS-13. This damaged area is located on the left and right main engines and extends over a region of approximately one square foot. Figure 4.1.1 shows the damage to the TPS for SSME Two. As can be seen from this figure, the screen, foil and the cerachrome insulation have melted, causing the manifold to be exposed. The elevon and body flap, flight experiences for the Best Estimate Trajectory (BET), of flight STS-1 to STS-32 are shown in Figs. 4.1.2 and 4.1.3, respectively. A comparison between REMTECH and Rockwell predictions for the 22 BET flights is shown in Fig. 4.1.4. Predictions were made for the left and right elevon schedules. Flights STS-1 through STS-13 were "step" TPS and had a TPS damage limit of 18.0 BTU/ $\text{ft}^2\text{-sec}$. Flights STS-14 through STS-32 had a "ramp" TPS with a maximum heating rate of 22.0 BTU/ $\text{ft}^2\text{-sec}$ for TPS damage. From Fig. 4.1.4 it is observed that even though Rockwell and REMTECH use different methodology to predict the heating to the SSME aft manifold, the results of the two methods are in agreement.

STS-11 NOZZLE TPS DAMAGE
ENGINE 2012 - POSITION 3



Figure 4.1.1: STS-11 Postflight Photo for SSME #2

ORIGINAL PAGE IS
OF POOR QUALITY

BEST ESTIMATE TRAJECTORY (BET) FOR STS-1 TO STS-32

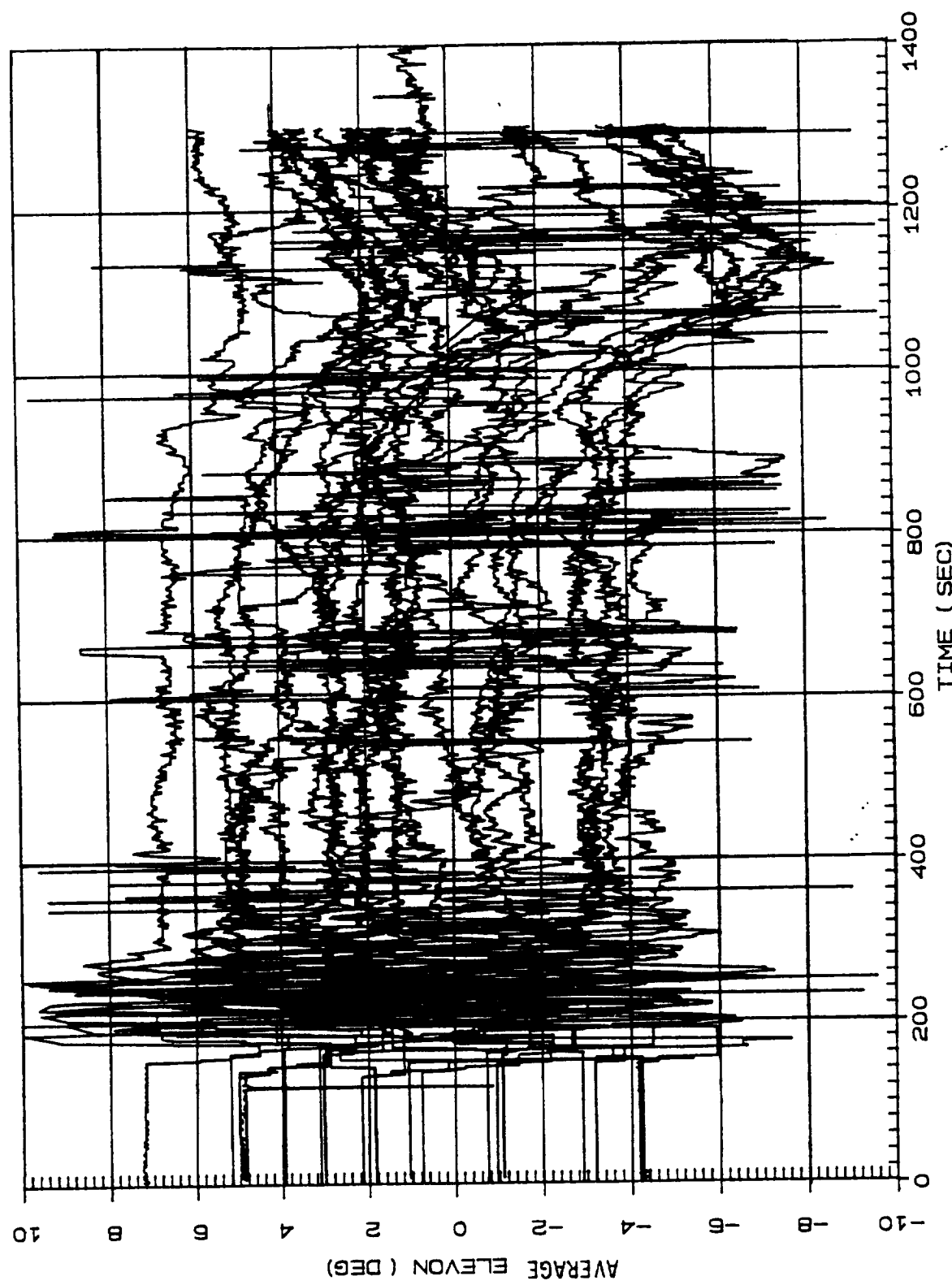


Figure 4.1.2: Elevon Flight Experience

BEST ESTIMATE TRAJECTORY (BET) FOR STS-1 TO STS-32

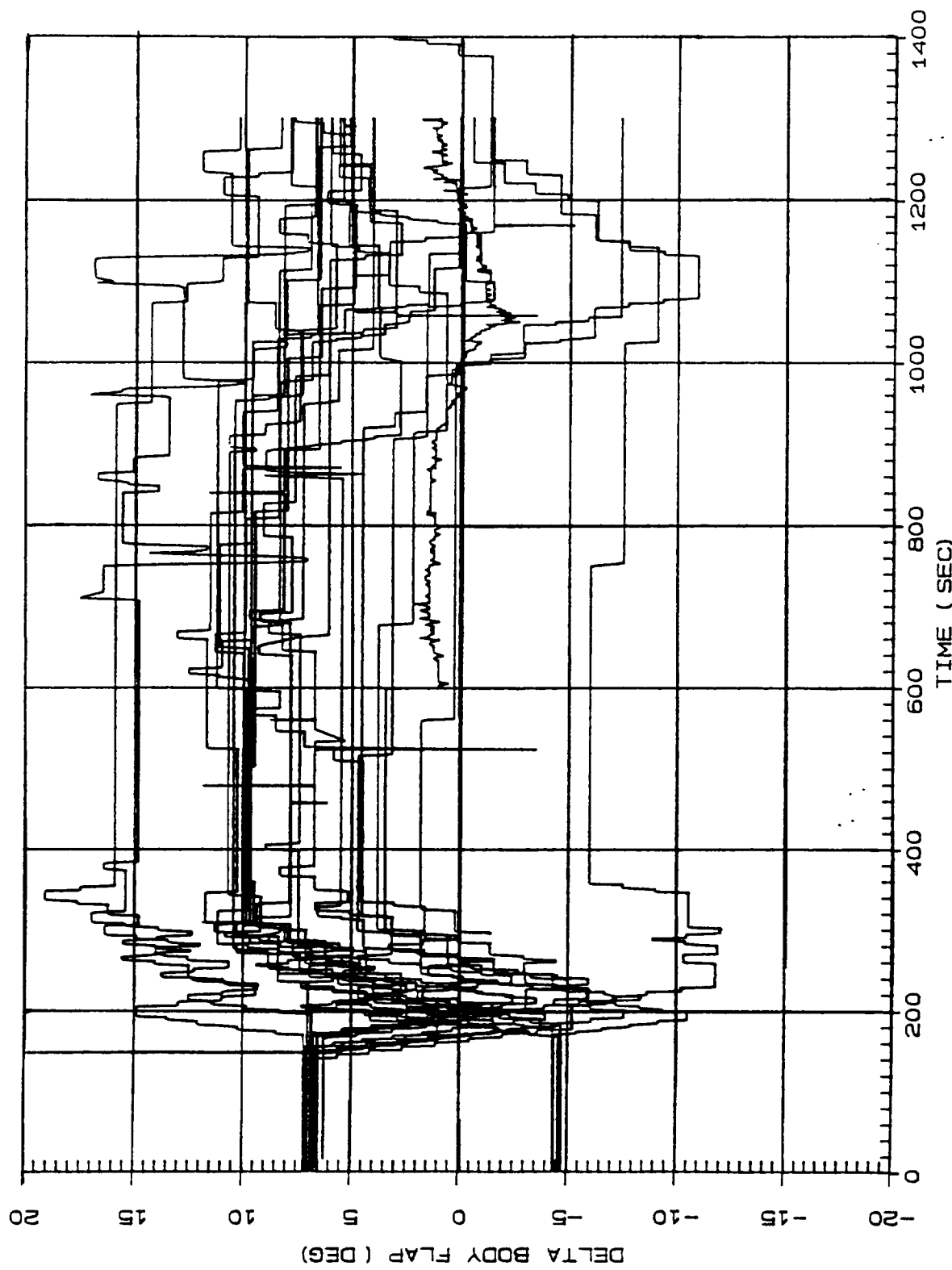


Figure 4.1.3: Body Flap Flight Experience

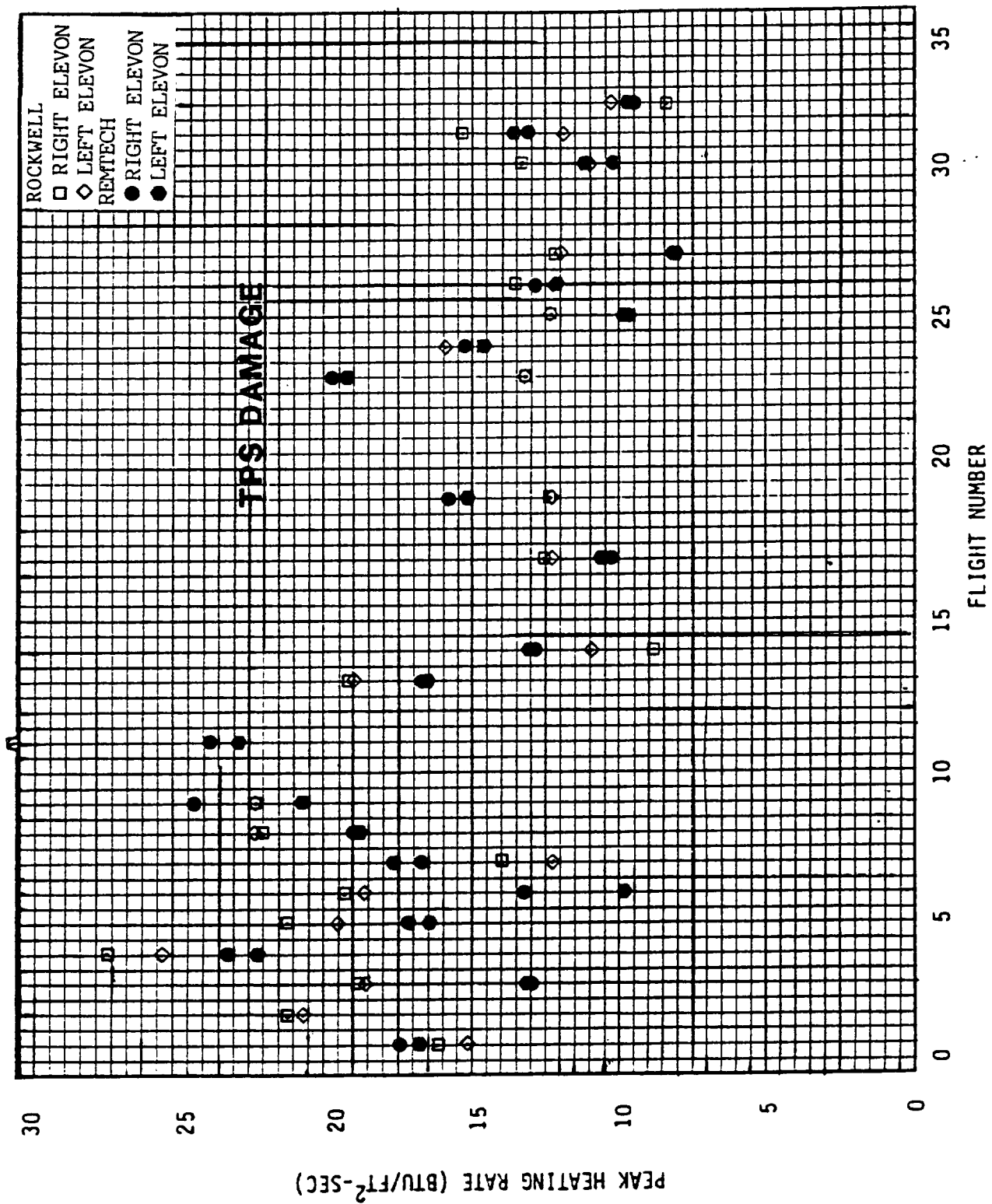


Figure 4.1.4: SSME Aft Manifold Flight Peak Heating Prediction

Section 5

DESIGN TRAJECTORY

The design trajectory was specified by the Integration Project Office (NASA/JSC) (Refs. 7, 8, 9). Figure 5.1.1 shows a comparison between the design angle-of-attack and the 22 Best Estimate Trajectory (BET) of previous flights. This Eastern Test Range (ETR) Trajectory/angle-of-attack is based on a 57 deg orbital inclination, a center of gravity location of 1075.7 inches and an approximate orbiter weight of 225,000 lbs. The alpha profile is based on the earliest possible bank reversal at a velocity of 23,000 ft/sec righthand turn descending ground track, which is the region of worst atmospheric condition. The velocity and dynamic pressure vs. time are shown in Figs. 5.1.2 and 5.1.3 for the descending node design trajectory.

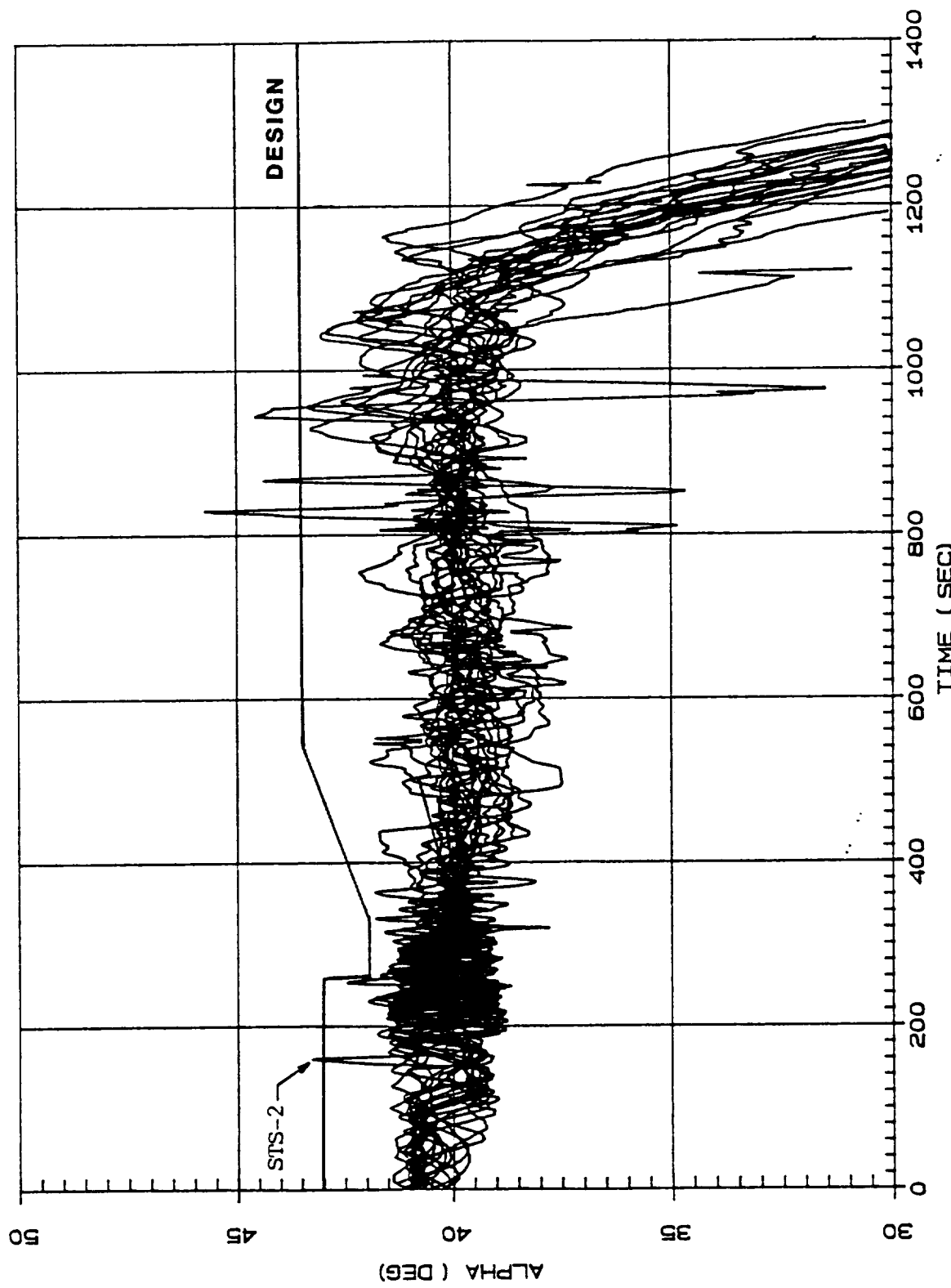


Figure 5.1.1: Descending Node Design Trajectory vs. "BET" for STS-1 to STS-32

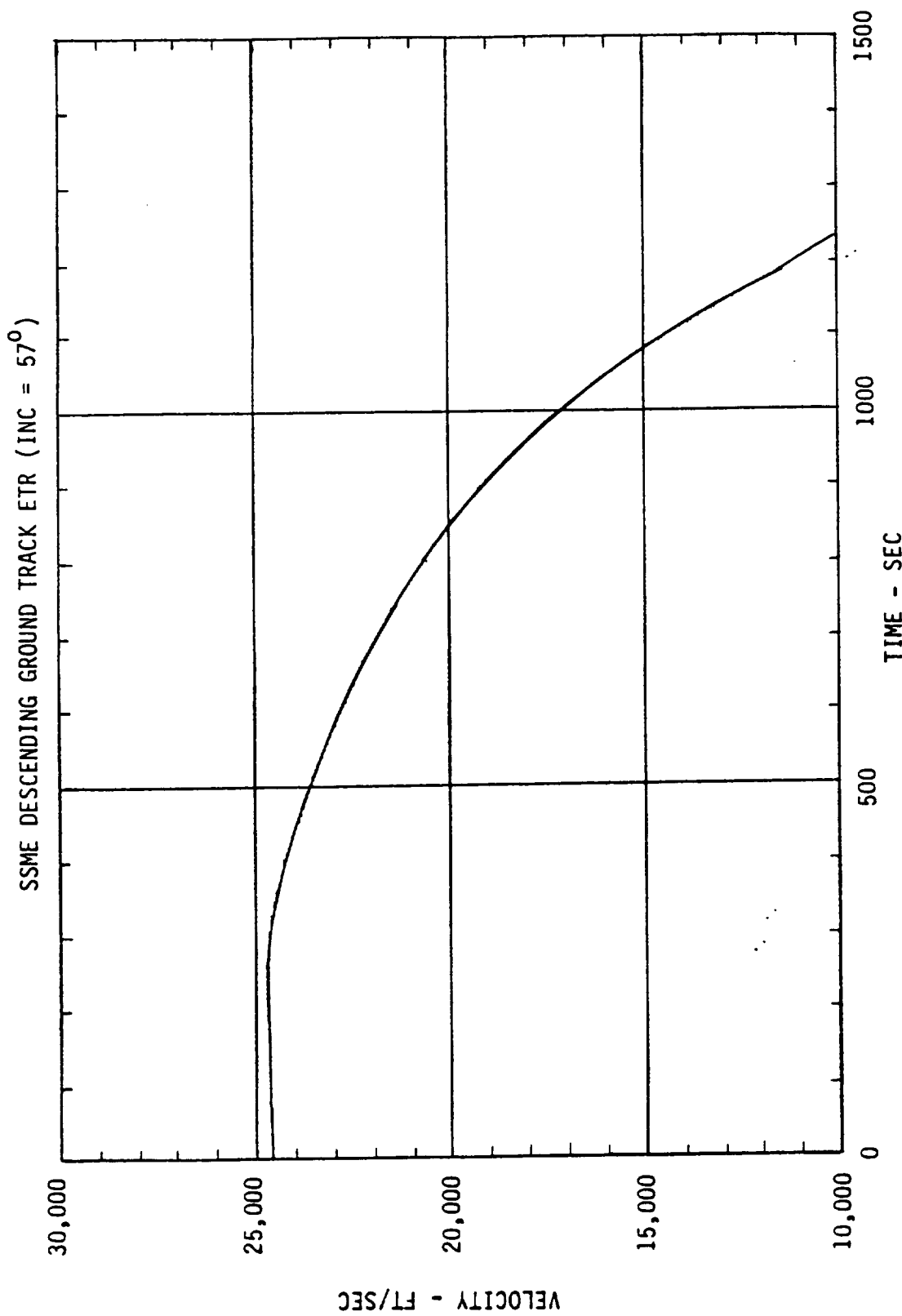


Figure 5.1.2: Descending Node Trajectory Velocity Time History

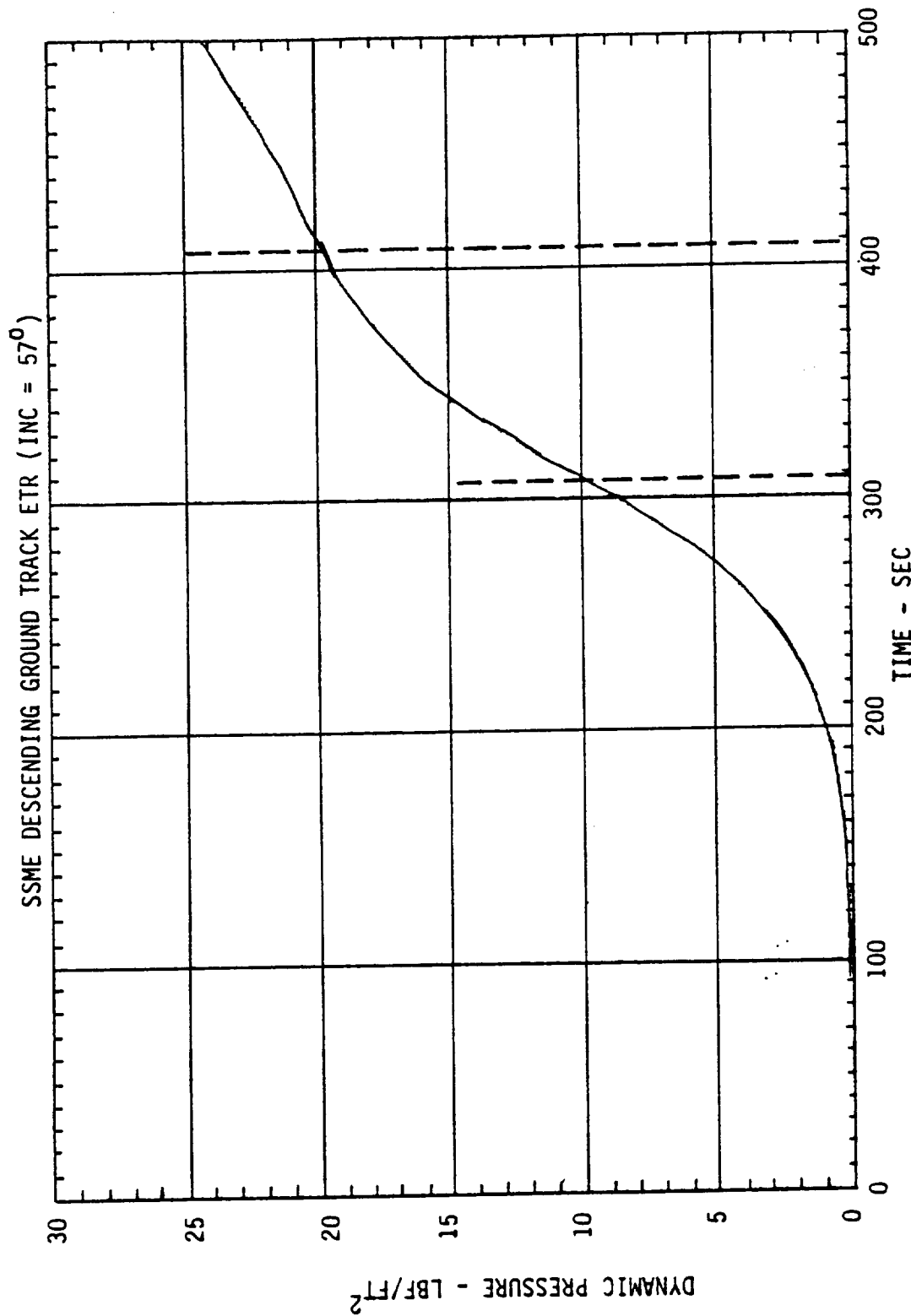


Figure 5.1.3: Descending Node Trajectory Q Time History

Section 6

DESIGN ENVIRONMENT

The REMTECH aerothermal math model as described in Section 3.1 was used with the supplied descending node design trajectory as presented in Section 5.0 to develop the REMTECH SSME reentry thermal environments. Nozzle peak heating rates were predicted for 10 forward, 12 mid and 12 aft center of gravity schedules (Figs. 6.1.1 and 6.1.2). The peak heating rate predictions are presented in Fig. 6.1.3. The worst heating time history occurs at a forward center of gravity location of 1076 (Fig. 6.1.4). Figure 6.1.5 shows a comparison of the worst forward, mid and aft center of gravity heating time history. The peak circumferential heating rate distribution for a "ramp" and "step" TPS configuration is shown in Fig. 6.1.6 for REMTECH and Rockwell predictions. It should be noted that the current alpha profile with the descending node trajectory results in 1.2 percent more heating to the nozzle when compared to the ascending node trajectory.

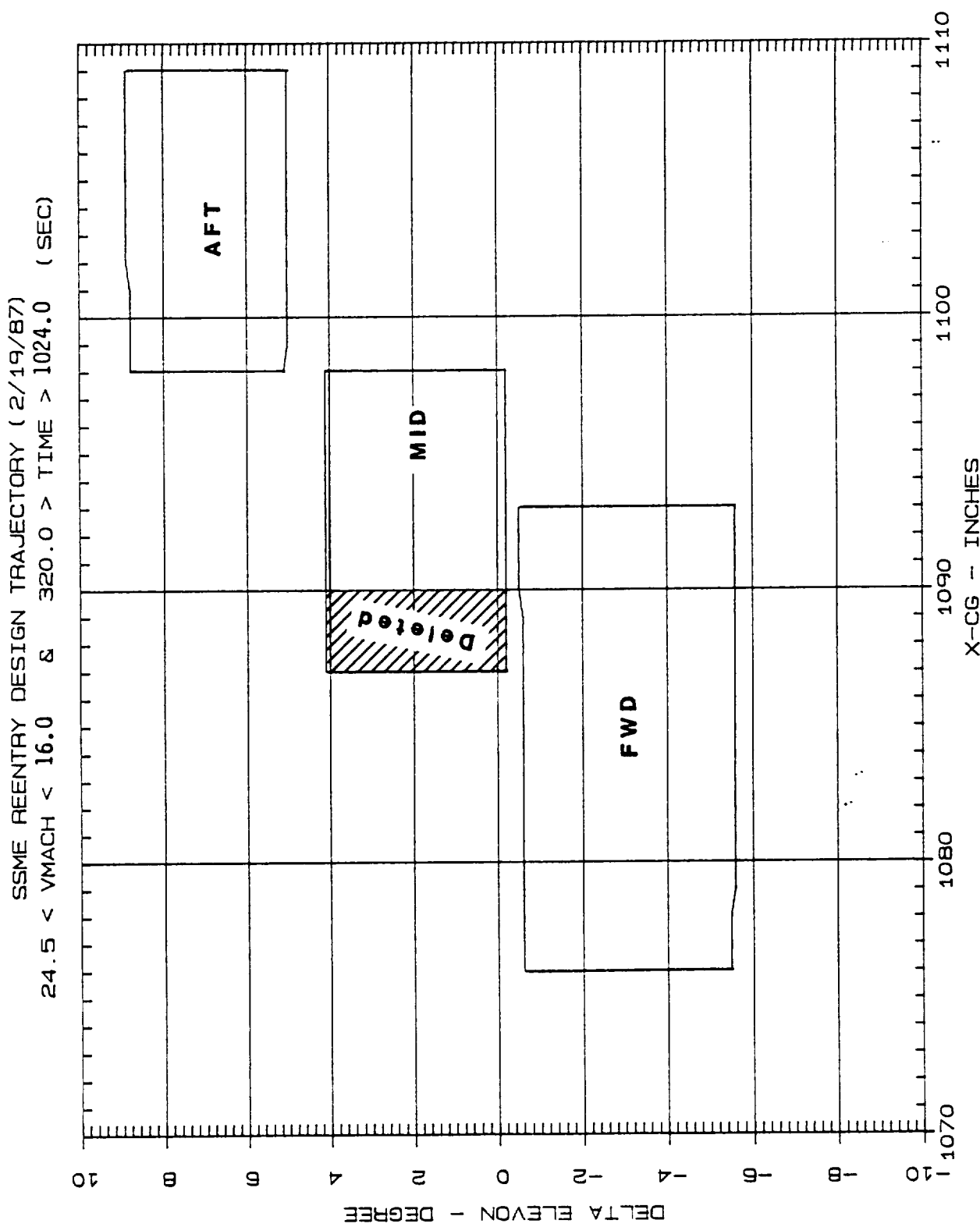


Figure 6.1.1: Design Environment Elevon Schedule

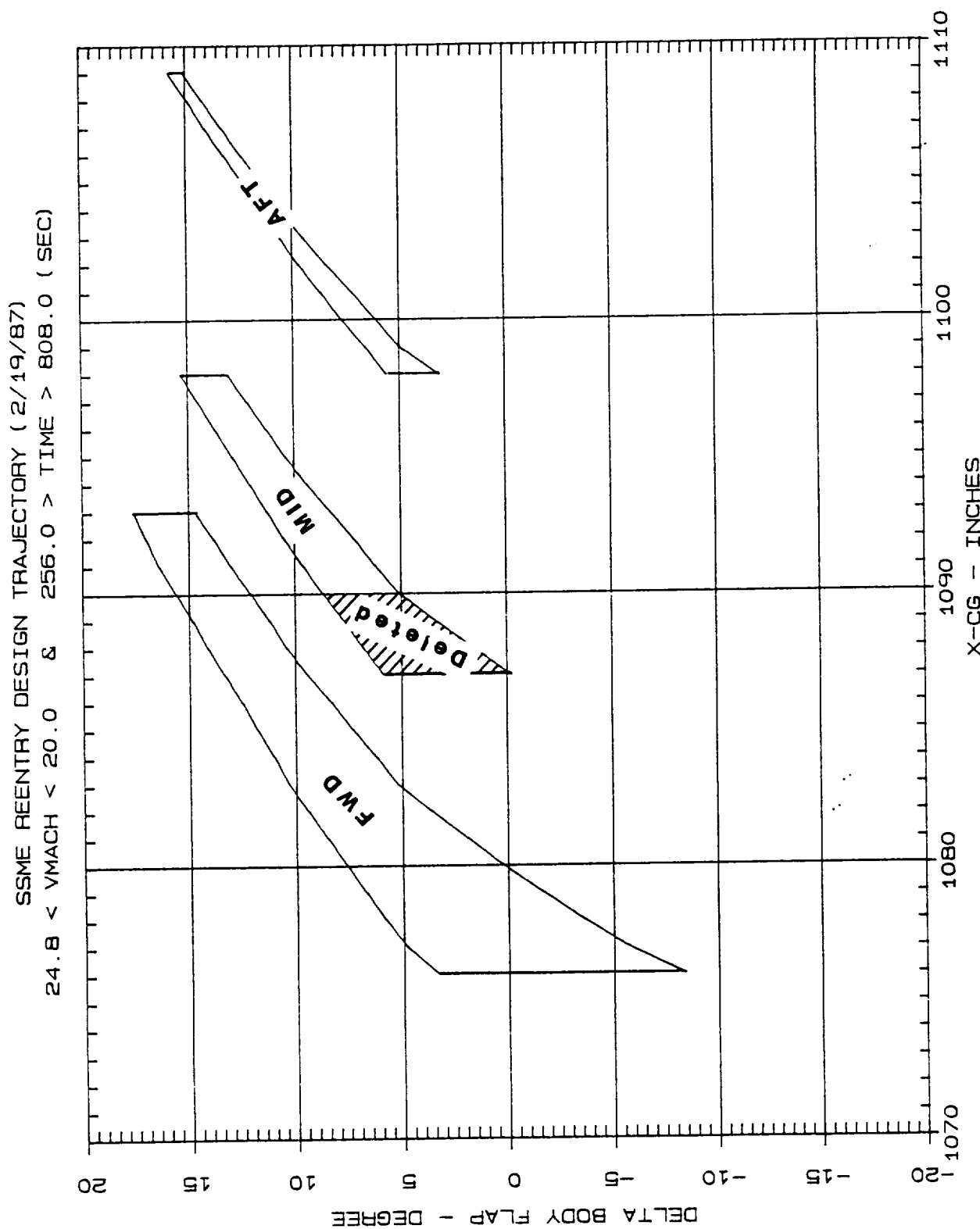


Figure 6.1.2: Design Environment Body Flap Schedule

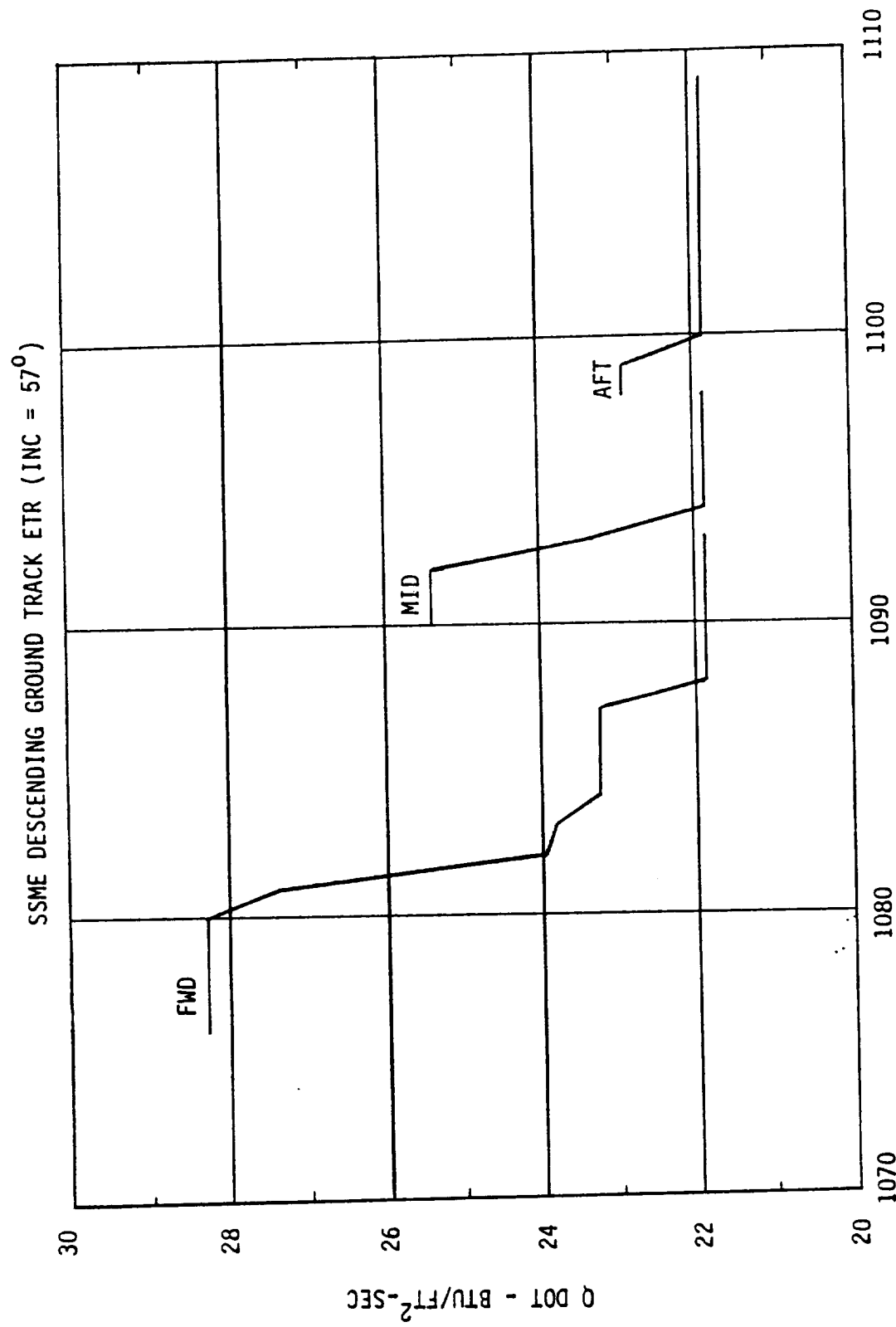


Figure 6.1.3: Peak Heating Prediction

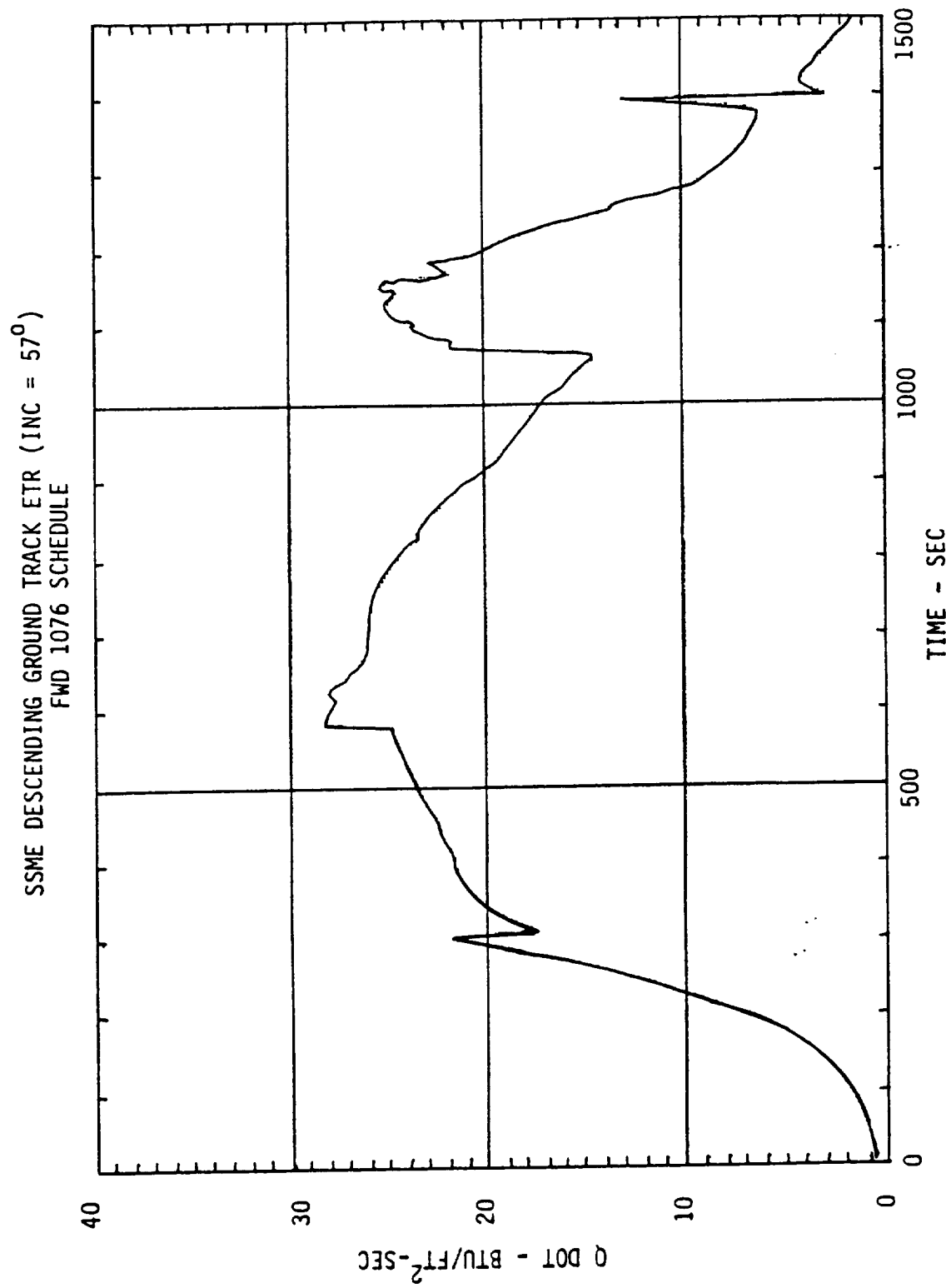


Figure 6.1.4: Worst Heating Time History

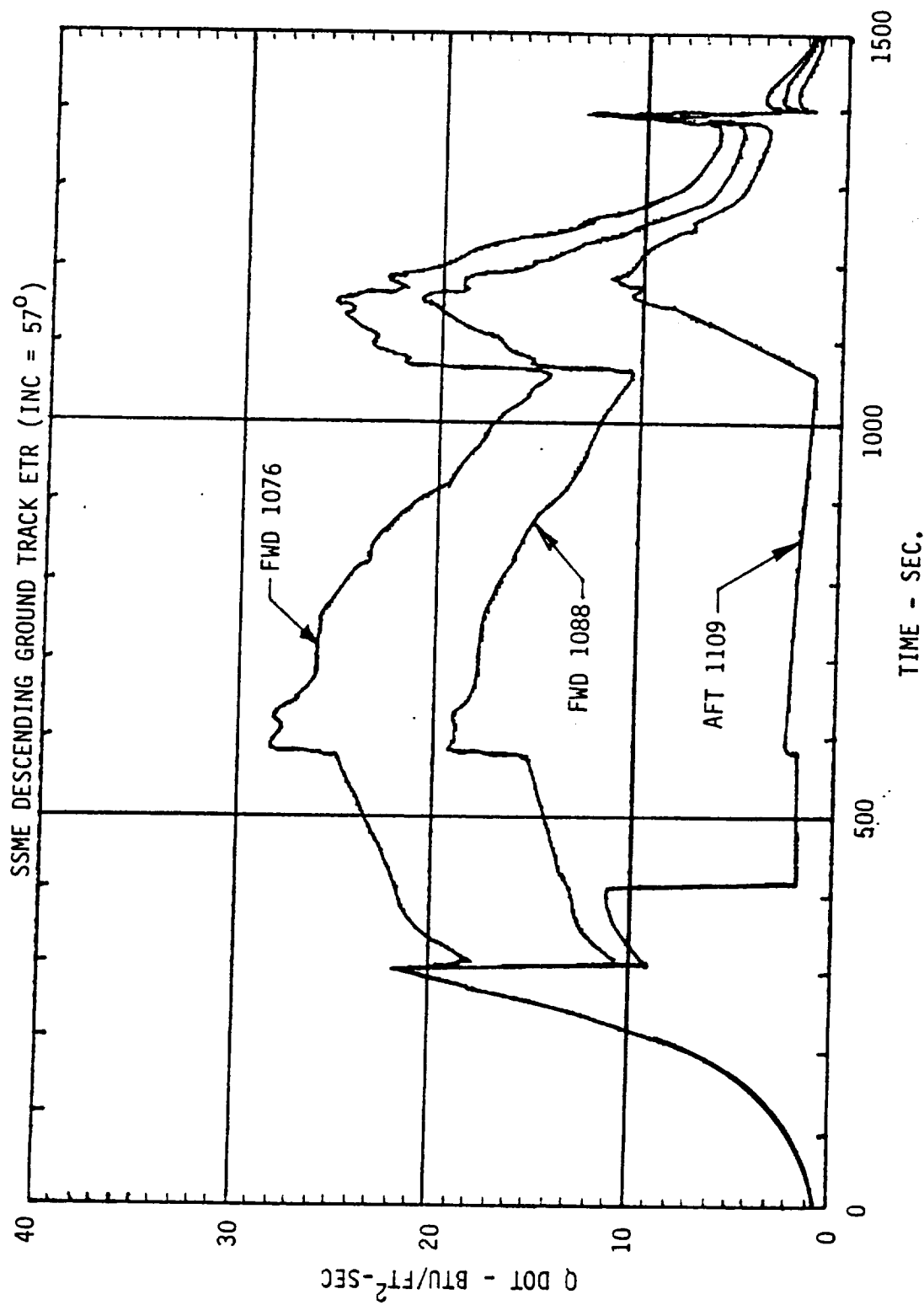


Figure 6.1.5: Worst Forward, Mid and Aft Heating Time Histories

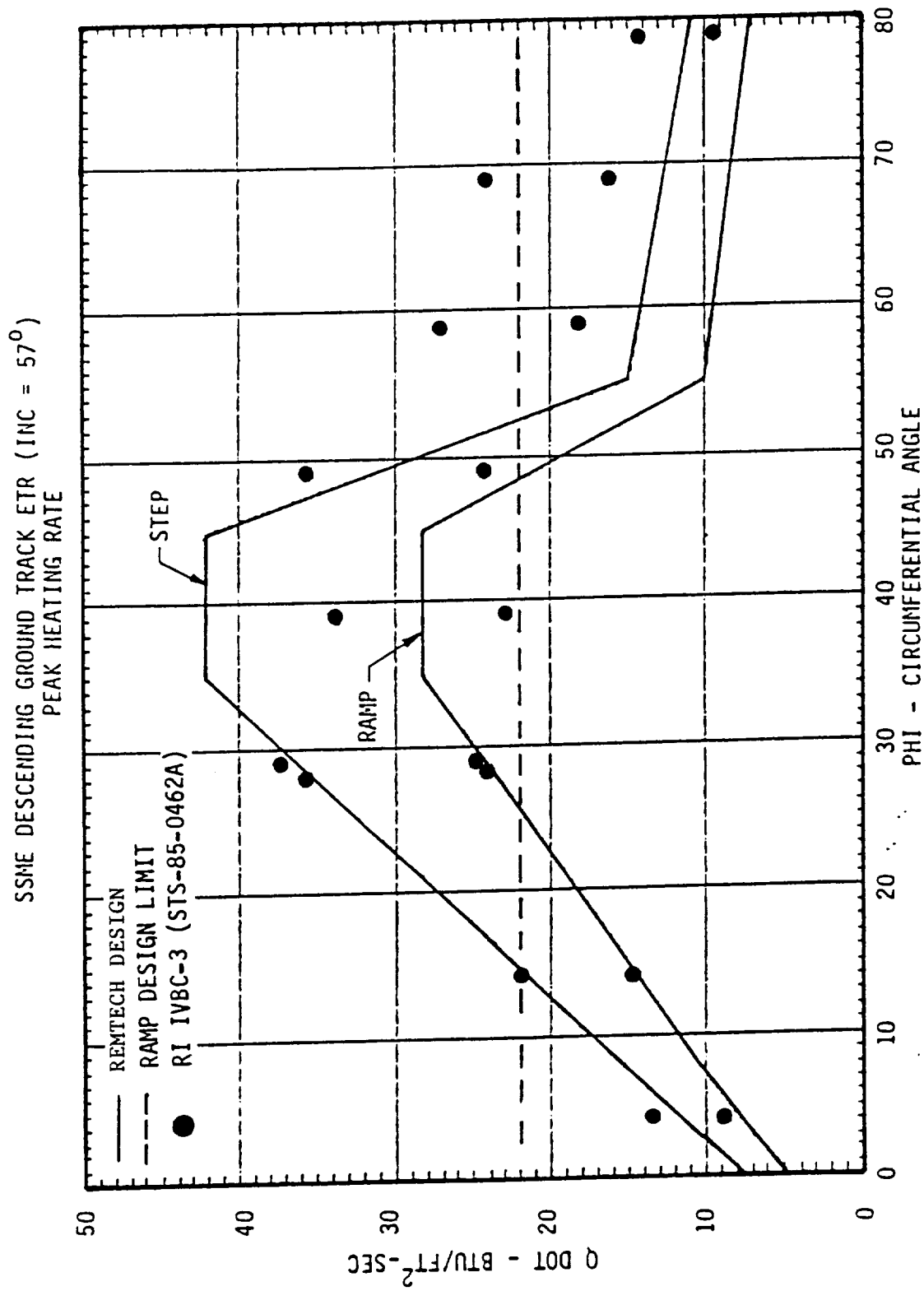


Figure 6.1.6: Peak Circumferential Heating Distribution

Section 7

REMTECH TPS DESIGN

7.1 1985 Environment

The thermal environments which were used to develop the design TPS are presented in this section. The entry flight regime covered by the IVBC-3 data (Ref. 10) corresponds to a dispersed WTR trajectory with 104 deg inclination. Figure 7.1.1 shows a comparison between the 3 sigma and no sigma angle-of-attack for this environment. The entry heating provided from Ref. 10 for heating of the aft manifold and hat bands, and on the surfaces between, are presented here in Table 7.1.1. Since no environments were provided for the $\phi=0$ deg locations, the data at $\phi=14$ deg were used. For the corners, environments for the "no ramp" configuration were used. Nominal alpha heating rate histories for the maximum heating area are shown in Fig. 7.1.2. To determine the design environment at each ϕ location, first, the one hundred second interval where the maximum heat load occurs between the three sigma alpha and the nominal alpha environments was found (this interval is found such that it includes the peak heat rate of the three sigma alpha environment); second, this maximum load was combined with the nominal alpha environment. Figure 7.1.3 presents the axial distribution of the aft manifold heating rate histories.

SSME ICD DESIGN ENTRY AEROHEATING TRAJECTORY (9/30/85)

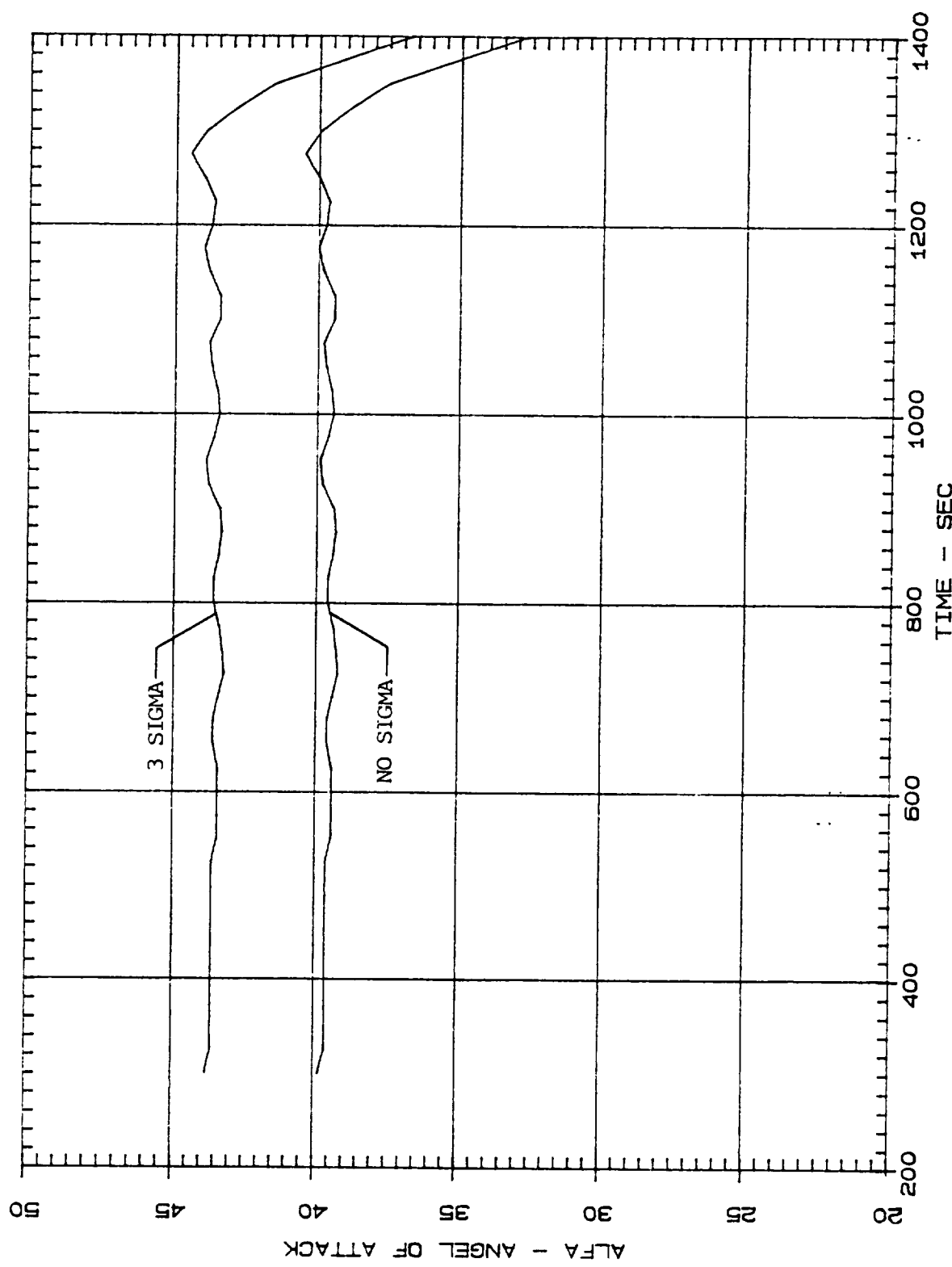


Figure 7.1.1: Comparison of 3 Sigma and No Sigma Angle-of-Attack

Table 7.1.1: Distribution of Maximum Heat Flux to SSME Nozzle (Ref. 10)

ICD 3σ TRAJECTORY, 3σ ALPHA DISPERSIONS

ϕ	$X_B - X$	AFT MANIFOLD 2.5 IN.			HAT BAND #9 16 IN.			HAT BAND #8 29.5 IN.			39.0 IN.
		\dot{q}	F_2	F_3	\dot{q}	F_2	18.5 IN.	25 IN.	\dot{q}	F_2	
14°	24.2	1.6	1.0	15.1	12.3	11.5	1.6	7.2	5.6	7.0	1.6
28°	42.9	1.6	1.0	26.8	—	—	—	—	—	—	—
29°	29.5	1.6	2/3	27.6	12.8	18.1	1.6	11.3	8.2	10.2	1.6
39°	28.5	1.6	2/3	26.4	25.1	19.2	1.6	12.0	8.9	11.1	1.6
49°	38.8	1.6	2/3	36.4	25.2	26.2	1.6	16.4	13.1	16.3	1.6
59°	22.3	1.6	2/3	20.9	14.1	15.0	1.6	9.4	6.6	8.2	1.6
69°	14.9	1.6	2/3	14.1	10.5	10.3	1.6	6.4	5.5	6.8	1.6
69°	22.4	1.6	1.0	14.	—	—	—	—	—	—	—
79°	13.3	1.6	1.0	7.8	6.2	10.1	1.6	6.3	6.5	8.2	1.6
											5.1

Note: $F_1 = 1.5$ for All Locations — $F_2 = F_3 = 1$ Except Where Noted
 = Ramped Area

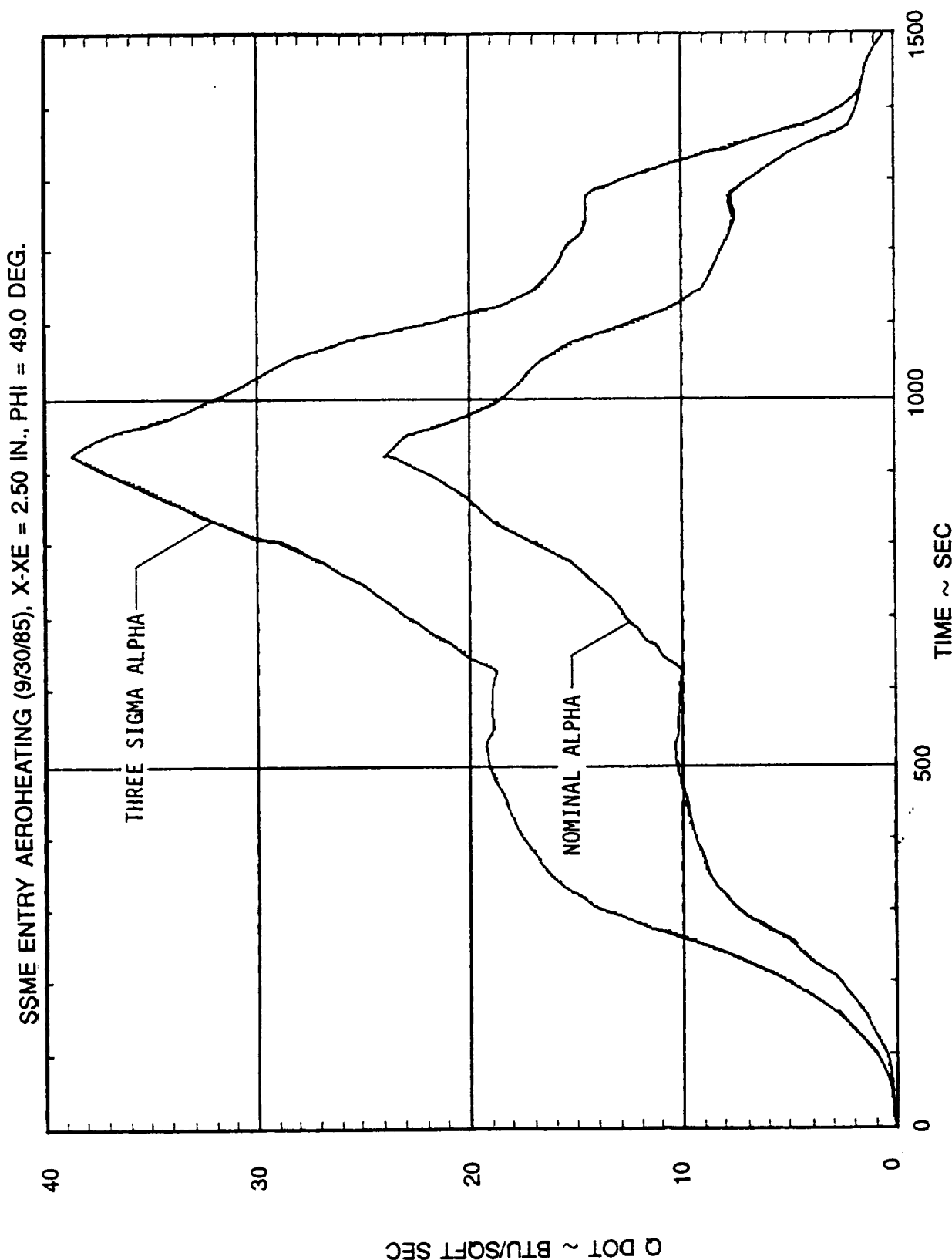


Figure 7.1.2: Nominal Alpha and Three Sigma ICD Design Trajectory

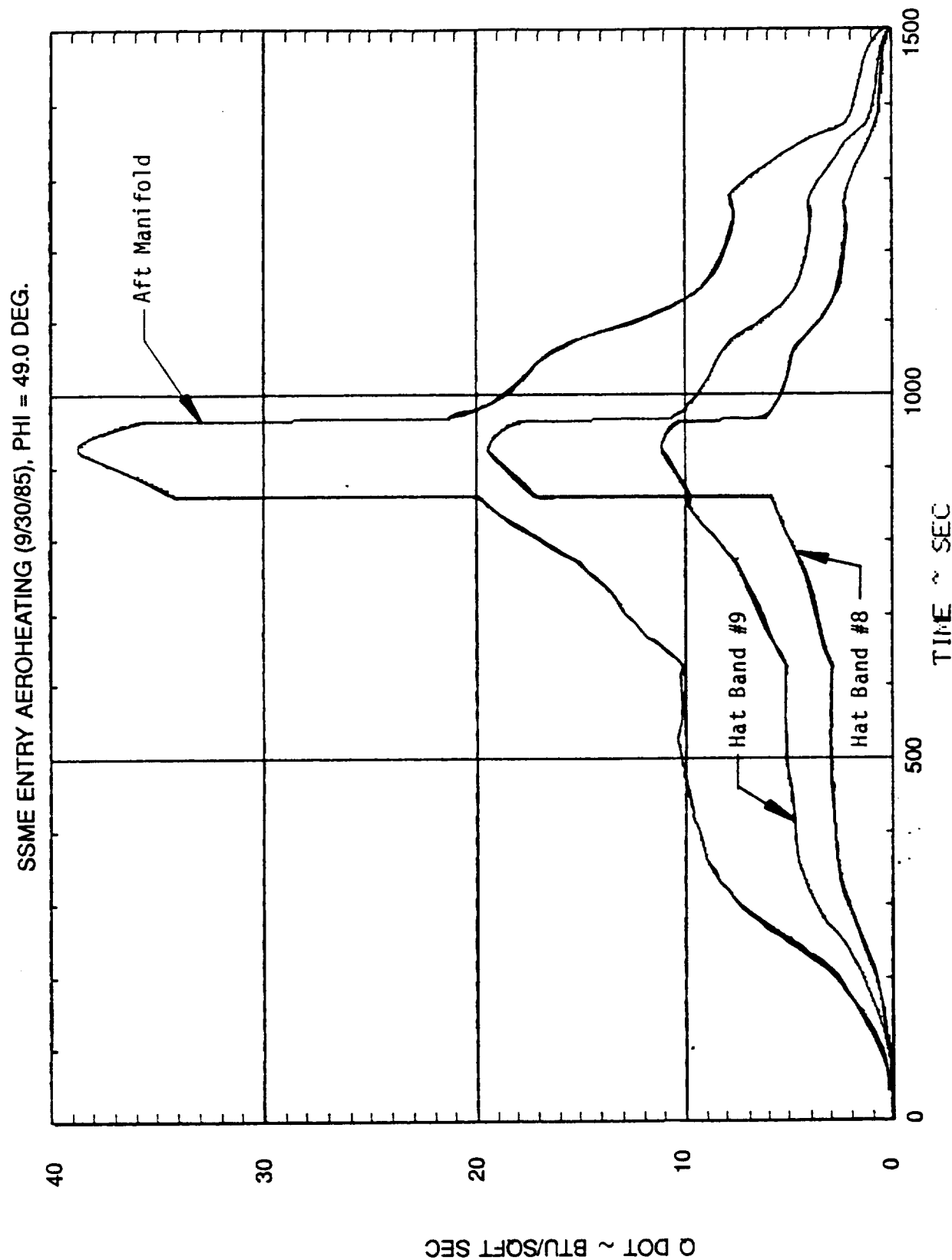


Figure 7.1.3: Heating Rate Distribution at $\text{PHI} = 49^\circ$

7.2 Bridge Concept

The design 1985 IVBC-3 environment presented in Ref. 10 is significantly higher than the original orbiter base heating reentry environment. The maximum heating predicted for the design trajectory with three sigma dispersions is approximately 38.8 BTU/ft²-sec to the aft manifold ramp TPS. Greater heating is expected to the aft manifold step if the ramp is not extended past its current boundaries. Damage to the current TPS is expected to occur if heating rates exceed 20.0 BTU/ft²-sec.

Flight experience to date has shown that the multi-layered TPS performs well for environments less than the damage threshold. To increase the capability of the current design for trajectories where heating rates are expected to cause TPS damage and possible manifold overheating, the TPS was redesigned and extended as shown in Fig. 7.2.1. A TPS support structure was developed to optimize strength and minimize weight. Several alternative designs were investigated, utilizing different materials and support structures. The configuration that was chosen utilizes the same composite blanket shown in Fig. 7.2.1, with the addition of seven (7) Inconel 718 "hat"-section stiffeners spaced evenly, and spot welded to the inside of the bottom 40-mesh screen. Figure 7.2.2 shows construction details of the TPS, along with details of the stiffeners and bracketry required to attach the TPS to the SSME nozzle. The stiffeners provide support to the TPS blanket, allowing the blanket to span the distance between hat-band #8 and #9, and hat-band #9 and the aft manifold, while also providing a solid area for the welded attachment of brackets. The stiffeners were sized to support a 5 psia pressure load applied to the TPS blanket without yielding. (See Appendix).

The TPS blanket is stitched and laced to the stiffeners, as well as to the 40-mesh screen inner and outer layers, to provide additional strength and to maintain blanket position inside the layers. Pinned and sliding joint at the corners, along with slotted brackets along hat-band #9 (Fig. 7.2.2), provide support for flight loads and serve as fixtures during assembly and attachment of the TPS to the nozzle. Figure 7.2.3 shows the TPS close-out concept at PHI = 79 deg between the aft manifold and hat bands #9 and #8. It is envisioned that this concept will also be used at PHI = 0 deg. The close-out structure consists of a cerachrome blanket one to two inches thick covered with 100 mesh screen (Fig. 7.2.3b). The procedure for installing the TPS is as follows: 1) three- to four-inch wide strips of 40-mesh screen are spot welded between the manifold and hat bands #9 and #8 at PHI = 0 deg and PHI = 79 deg; 2) The TPS close-out block is spot welded with foil to this screen; 3) The ramp TPS is installed over the manifold and the hat bands; and 4) The 40 mesh screen of the ramp TPS is brought over the close-out blocks and spot welded with foil to the close-out blocks.

At the ends of the TPS blanket, the outer and inner 40-mesh screen layer edges are pulled together and spot welded to the surrounding structure as a method of closure for blocking air-flow into the TPS inside air space. Spot welding of the screen around the perimeter of the blanket to the nozzle produces a TPS structure that is unitized with the nozzle, and sufficient flexibility should be present in the blanket to allow for distortion and deflection of the nozzle during engine usage without loss of TPS structural integrity.

Various screen, foil and felt TPS materials were considered and investigated as a replacement for the current TPS design. Through thermal analysis, it has been shown that the redesigned TPS structure between PHI = 29 deg and 49 deg, hat band #9 and aft manifold, experiences surface temperatures greater than the melting temperature (2550°F) of the nichrome. This causes damage to the nichrome screen and foils. Several different refractory metals which have a melting temperature greater than 3000°F such as molybdenum, chromium, boron nitride and vanadium were considered as a replacement for nichrome. From the above materials, molybdenum has the best physical properties such as weldability, strength/stiffness at high temperature, weight and cost but it has low emissivity. Considering material emissivity of the above materials compared with nichrome, which has a high emissivity, it was concluded that within the limitations of this investigation nichrome is the best material to use for this TPS configuration. A layer of Nicalon cloth is also added under the 40 mesh screen and two foils to protect the felts for the locations where the surface temperature is greater than the screen melt temperature. This material has a service temperature of 3200°F which will withstand the highest expected heat flux of 38.8 BTU/ft²-sec. Nicalon cloth is needed in the TPS composite between ϕ = 19 deg and X-XE = 2.50-14.75 inches (i.e., AFT manifold and hat band #9).

To reduce the weight of the composite blanket, several different felts, blankets and fibers were considered. One of the materials considered was zirconia and alumina felts, which have very attractive thermal properties and melting temperatures, but their mechanical properties are not sufficient to withstand the SSME start-up vibrations and acoustical loads during liftoff. Hence, it was decided to use cerachrome as the TPS material. Table 7.2.1 presents the TPS materials considered and selected. During this investigation, discrepancy with thermal conductivity data of various cerachrome densities was found. The data used in this analysis are shown in Fig. 7.2.4 and were supplied by Manville Corporation (Ref. 11) which manufactures the cerachrome. Figure 7.2.5 shows the cross section of the design TPS. A parametric study was performed to determine the optimum weight of the composite blanket for the four different densities of cerachrome refractory fiber. Table 7.2.2 shows the results of this 1-D thermal analysis. Within the limitation of this study, it is recommended that the 4.0 lbm/ft³ density cerachrome fiber blanket

be used, since it is readily available and has the least mass. The 4 lb cerachrome thickness of the design TPS is presented in Fig. 7.2.6. Figure 7.2.7 summarizes the REMTECH TPS design. Thermal properties of the materials used appear in the appendix.

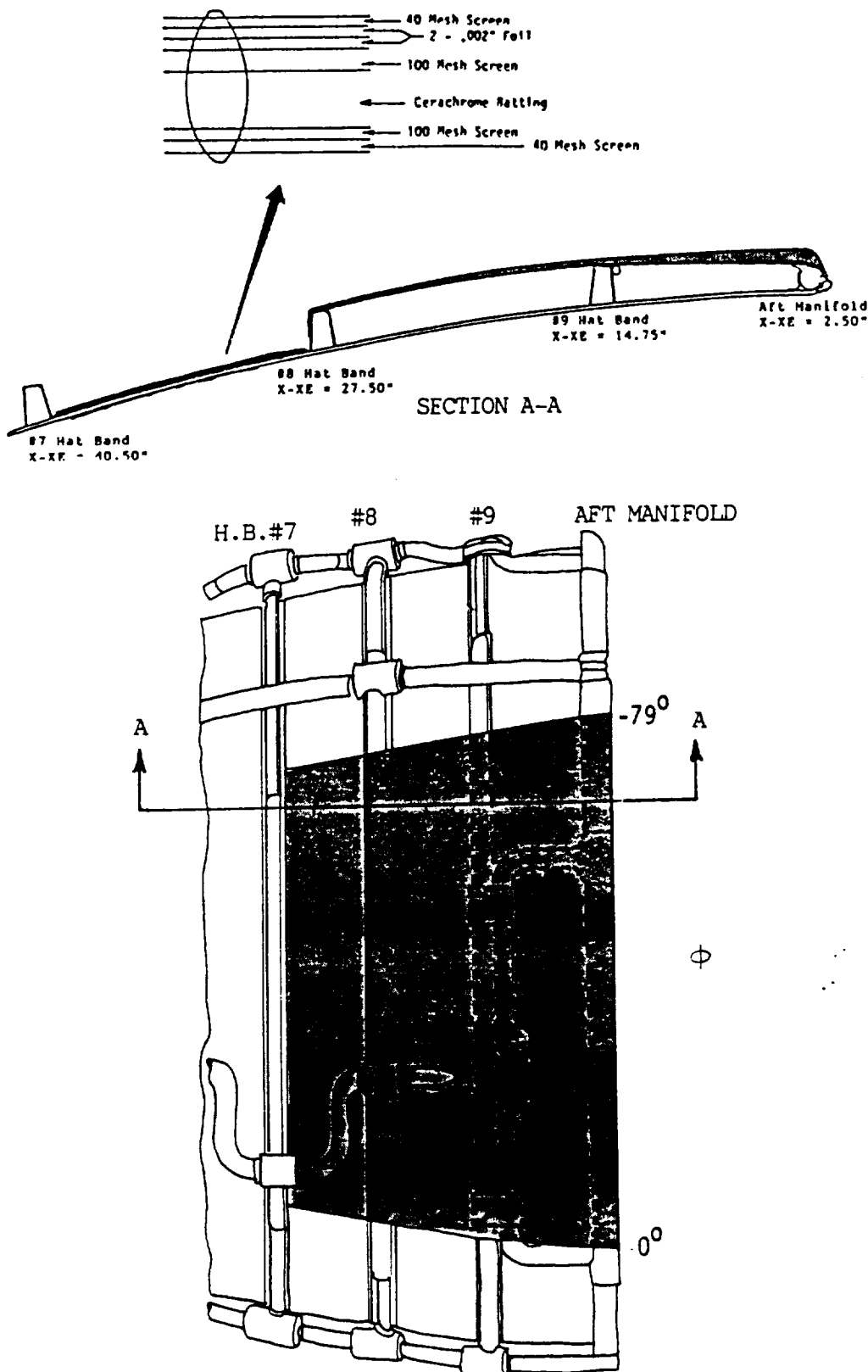
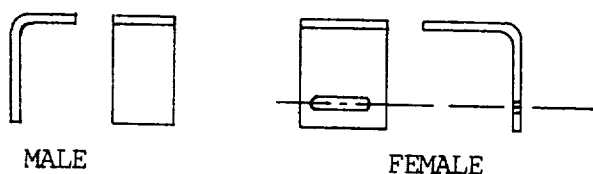


Figure 7.2.1: REMTECH Design TPS



GN #1
FFENERS

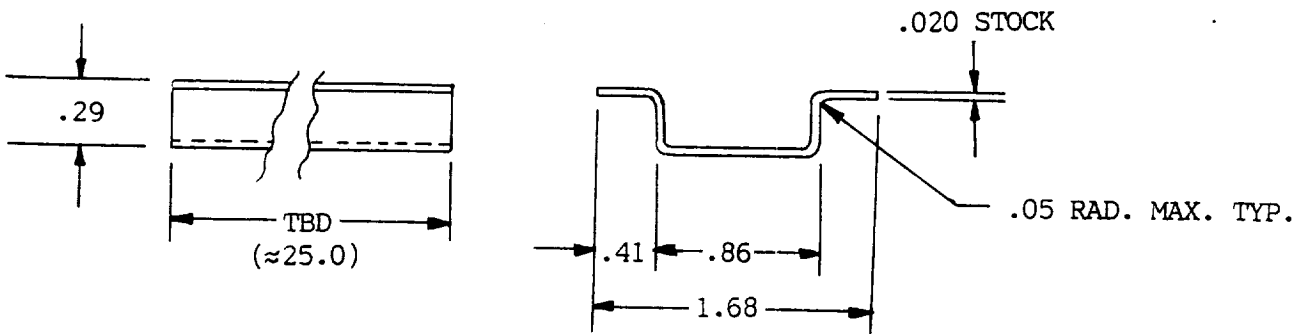
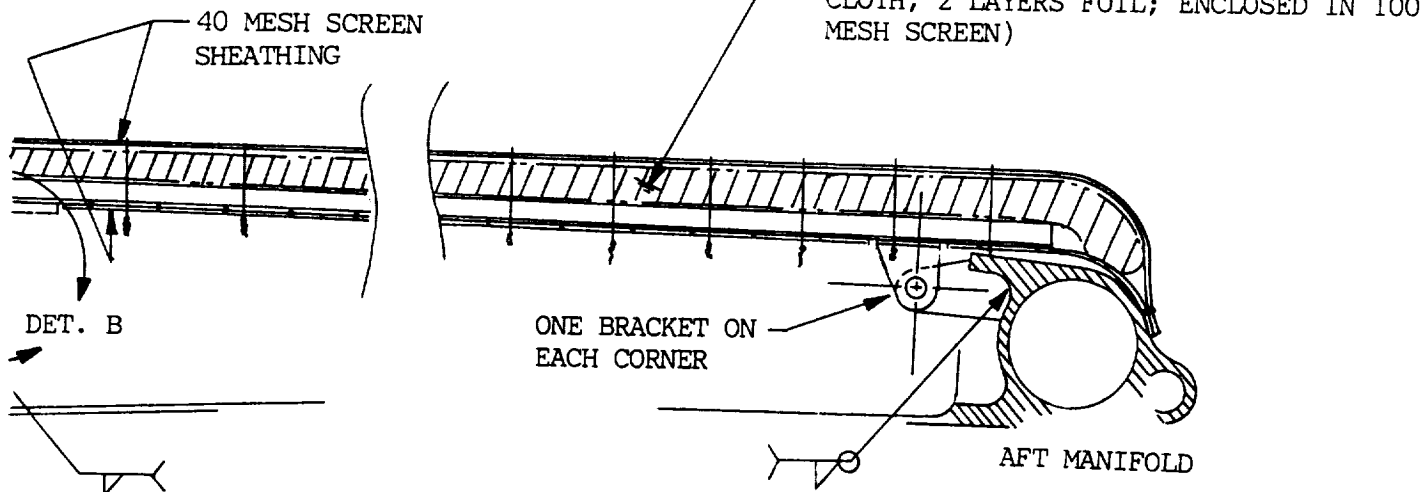
E

DETAIL B: BRACKETS

.050 STK INCONEL

FFENERS
REEN

FFENER, 7 REQ'D,
DETAIL "A"

DETAIL A: STIFFENER, 7 REQ'D, INCONNEL 718

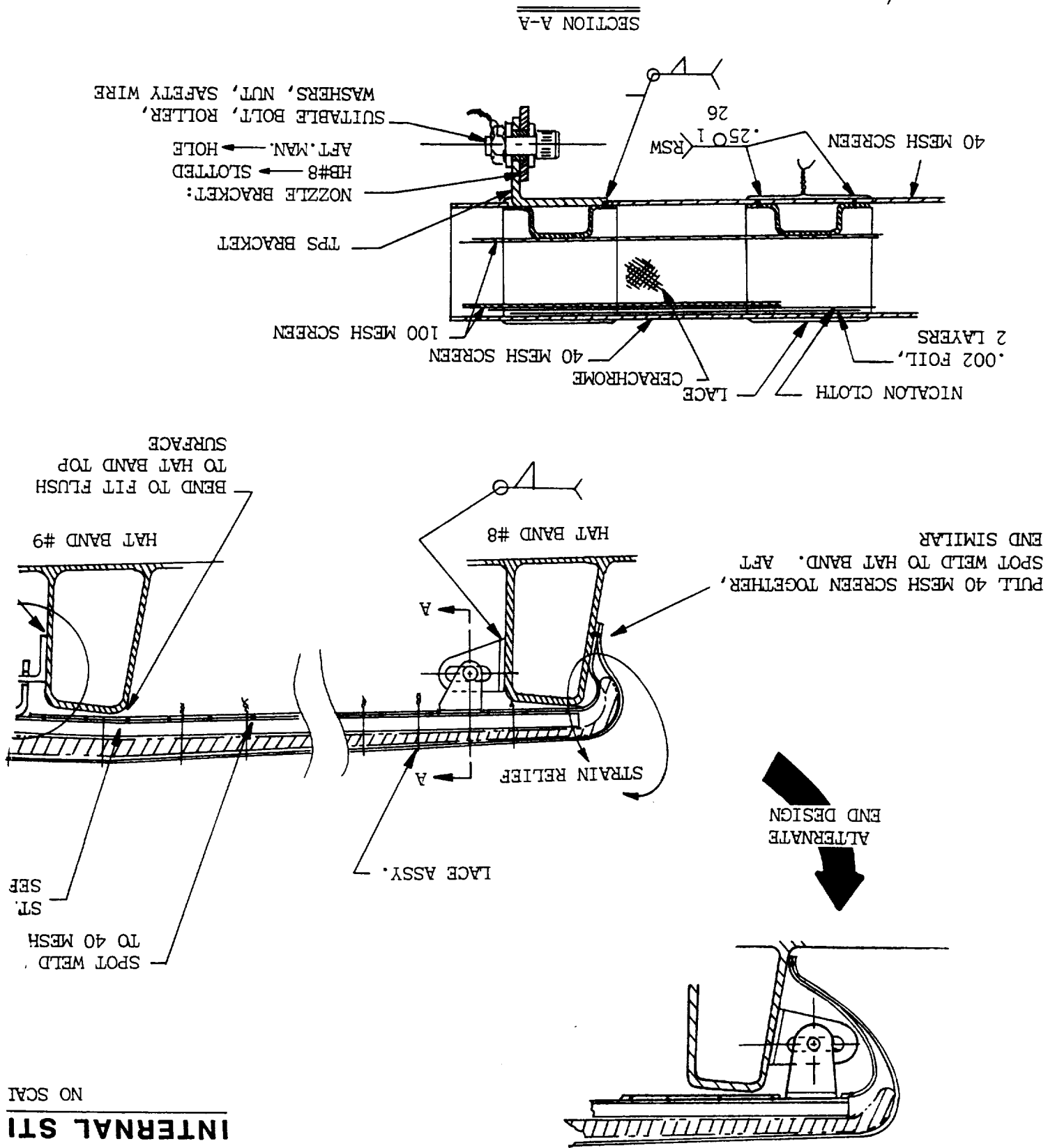
NO SCALE

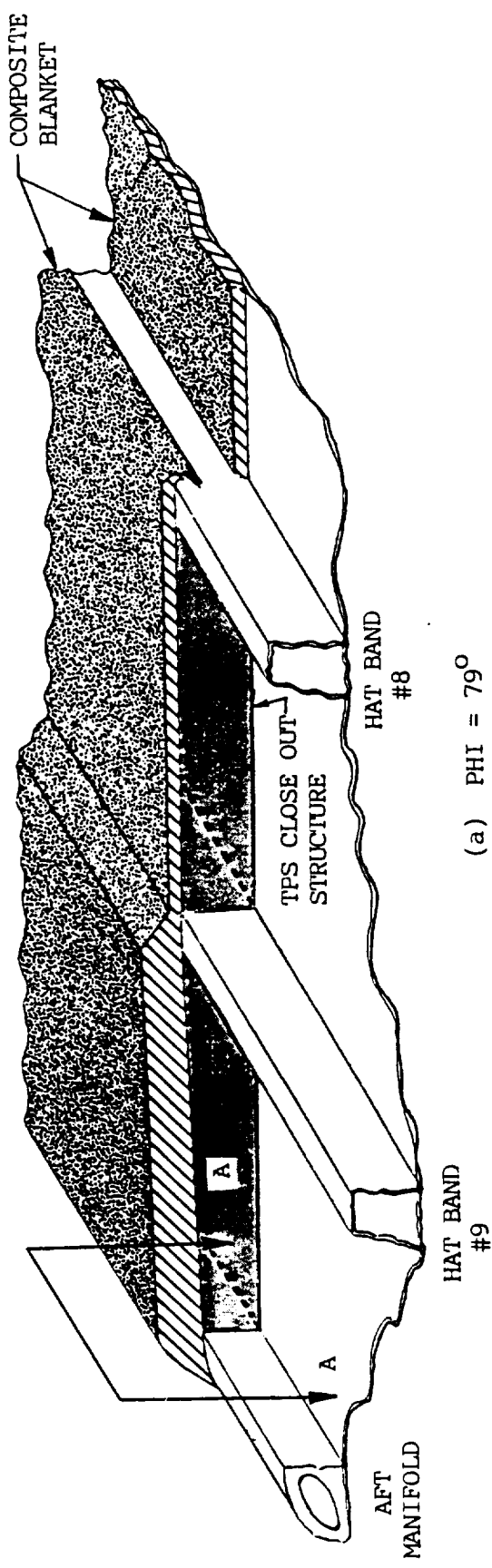
Design #1, Internal Stiffeners

2.

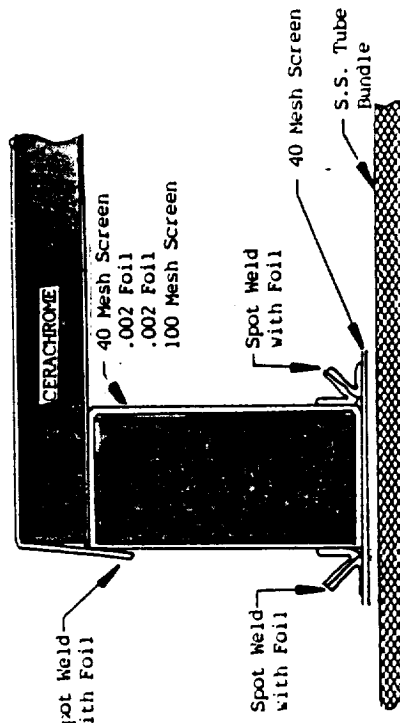
FOLDCUT FRAME

Figure 7.2.2: TPS





(a) PHI = 79°



(b) SECTION A-A

Figure 7.2.3: TPS Closeout Concept at Ramp-Manifold Intersect

Table 7.2.1: TPS Materials Considered and Selected

1	SCREENS AND FOILS CONSIDERED
	a) MOLYBDENUM - EXCELLENT PHYSICAL PROPERTY, LOW EMISSIVITY, 4760° F MELT TEMPERATURE
	b) *NICHROME - GOOD PHYSICAL PROPERTY, HIGH EMISSIVITY, 2550°F MELT TEMPERATURE
	c) *NICALON CLOTH - HIGH MELT TEMPERATURE (3200 - 3400°F)
2	FELTS CONSIDERED
	a) ZIRCONIA ρ & K EXCELLENT
	b) ALUMINA UNATTRACTIVE MECHANICALLY
	c) *CERACHROME ρ & K GOOD MECHANICALLY

•MATERIAL SELECTED

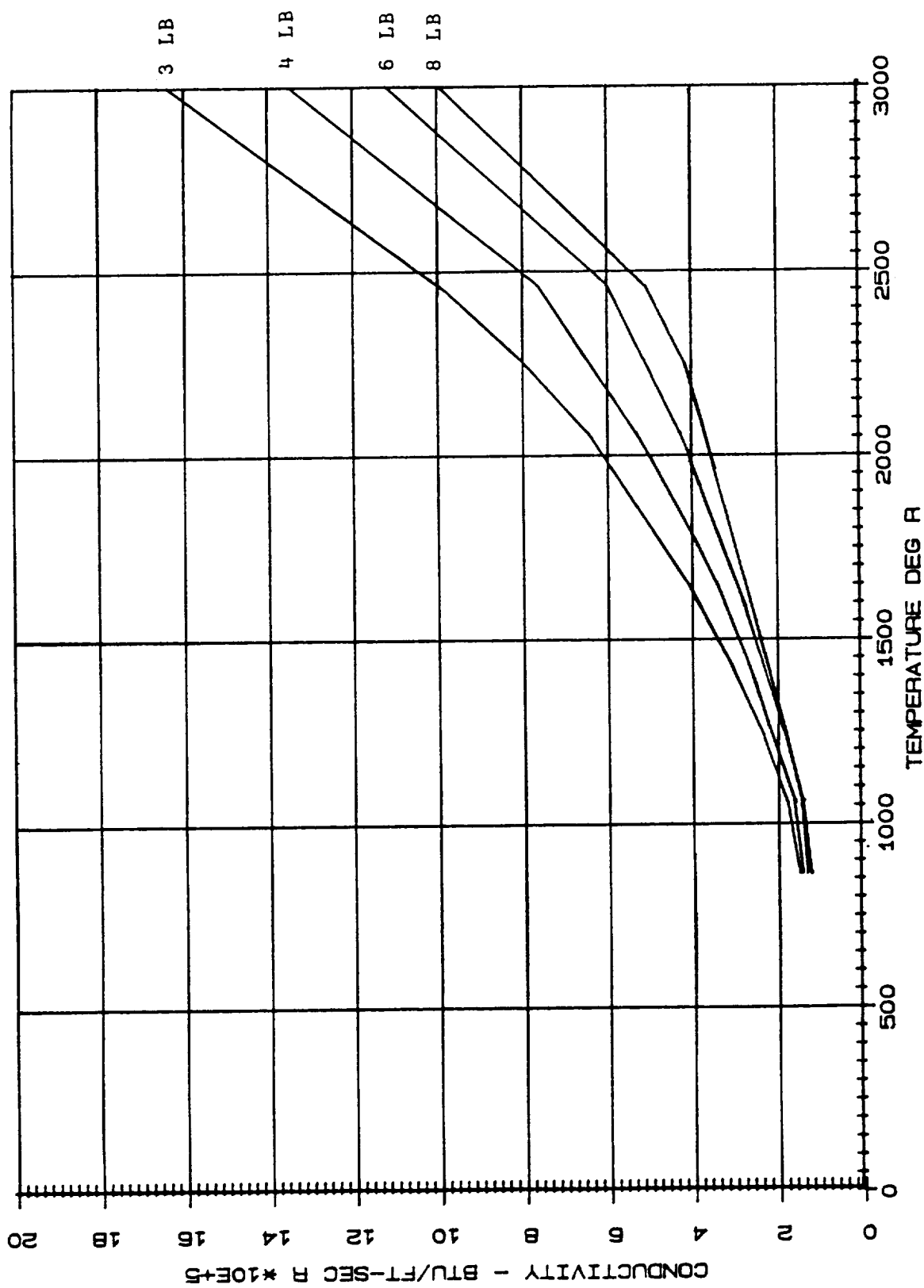


Figure 7.2.4: Thermal Conductivity vs. Temperature for Different Cerachrome Densities (Ref. 3)

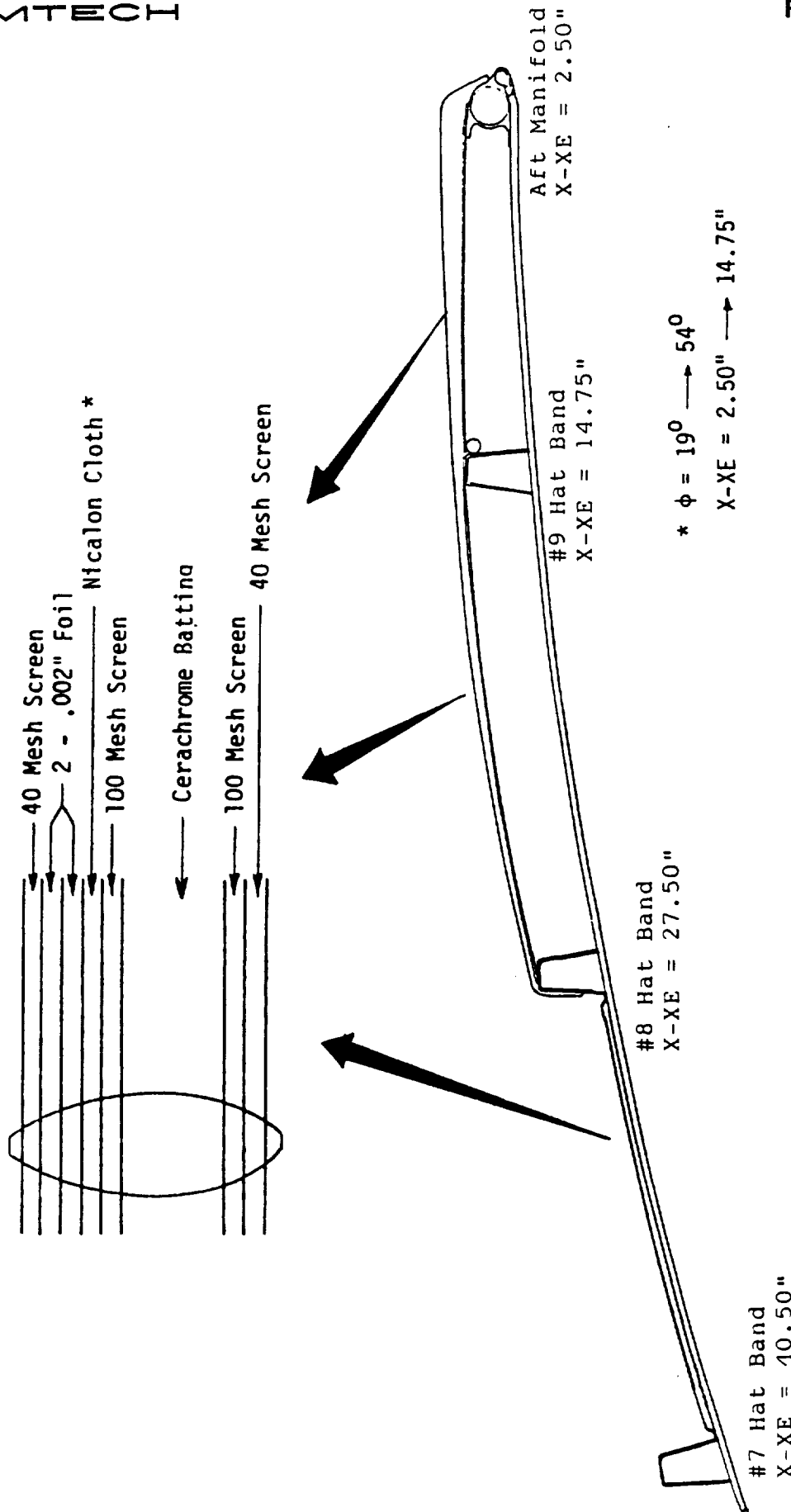


Figure 7.2.5: SSME Redesigned TPS

Table 7.2.2: Estimated TPS Weight

CERACHROME DENSITY (lbm/ft ³)	CERACHROME BLANKET MASS (lbm)	SCREENS, FOILS, NICALON MASS(lbm)	SUPPORT STRUCTURE MASS (lbm)	TOTAL TPS MASS (lbm)
3.0	4.47	7.46	3.53	15.46
4.0	4.78	7.46	3.53	15.68
6.0	5.89	7.46	3.53	16.88
8.0	7.45	7.46	3.53	18.44

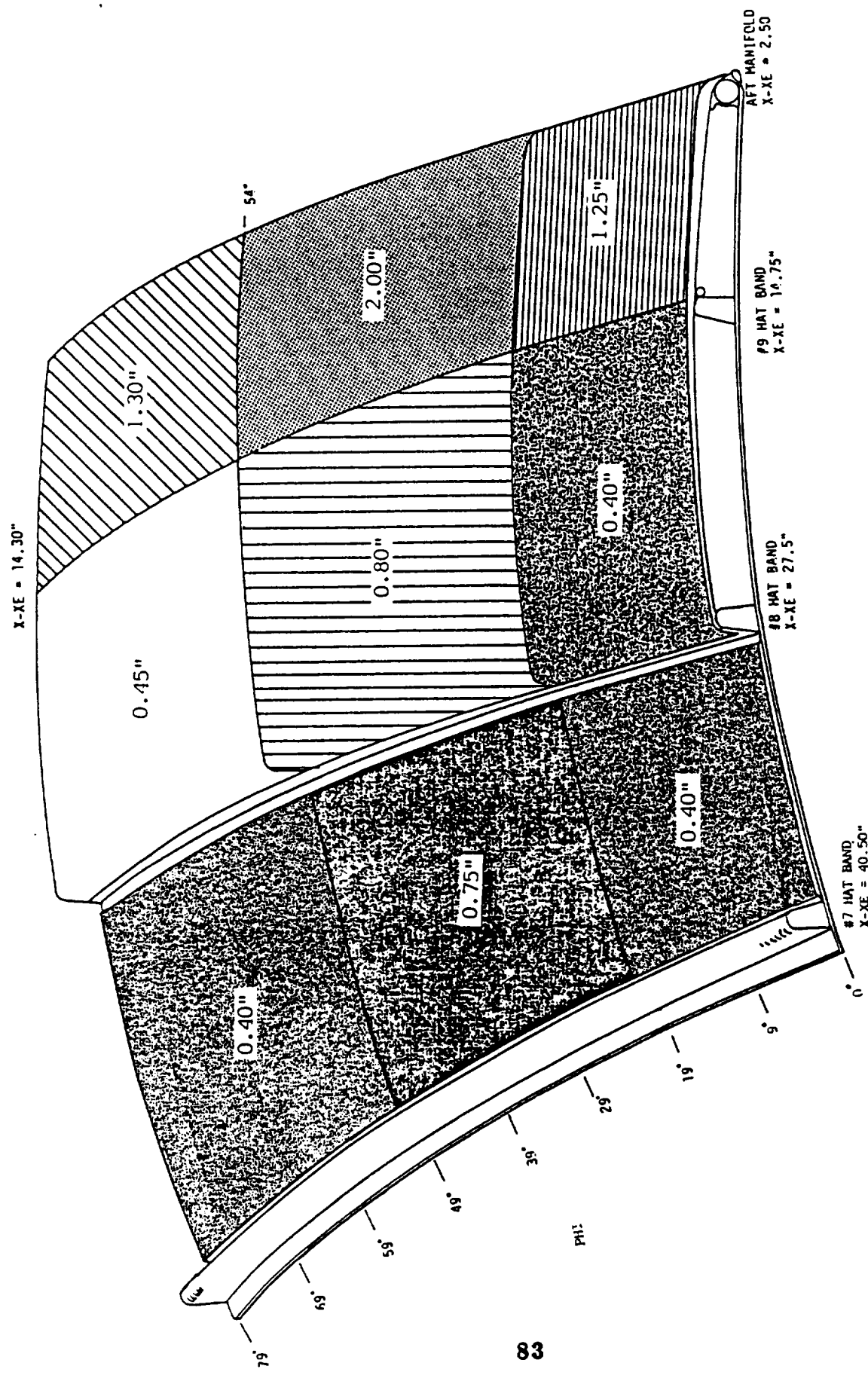


Figure 7.2.6: Four Lb Cerachrome Thickness for SSME Redesigned TPS

- LIGHT WEIGHT 4 LB CERACHROME COMPOSITE BLANKET
- RAMP TPS BETWEEN MANIFOLD AND HAT BAND #8 REDUCES HEATING
- NICALON CLOTH FOR $19^{\circ} \leq \phi \leq 49^{\circ}$ BETWEEN MANIFOLD AND HAT BAND #9 TO PROTECT THE CERACHROME AFTER NICHROME SCREEN AND FOILS MELT (2550°F)
- INCONEL 718 MANIFOLD AND HAT BANDS #8 AND #9 TEMPERATURE REMAINS BELOW 1300°F
- A-286 SS TUBE BUNDLE REMAINS BELOW 1000°F

COMPONENTS	WEIGHT LB
4LB CERACHROME BLANKET	4.78
SCREENS, FOILS	7.09
NICALON CLOTH	0.37
STIFFENERS	3.53
BRACKETS, BOTTLS, ETC.	0.40 (ESTIMATED)
TOTAL	16.17

Figure 7.2.7: REMTECH TPS Design

Section 8

TPS THERMAL RESPONSE

8.1 1987 Design Environment

The SSME descending ground track ETR with 57 deg inclination trajectory as described in Section 5.0 results in the design environments described in Section 6.0. Figure 8.1.1 presents the highest heating rate on the aft manifold.

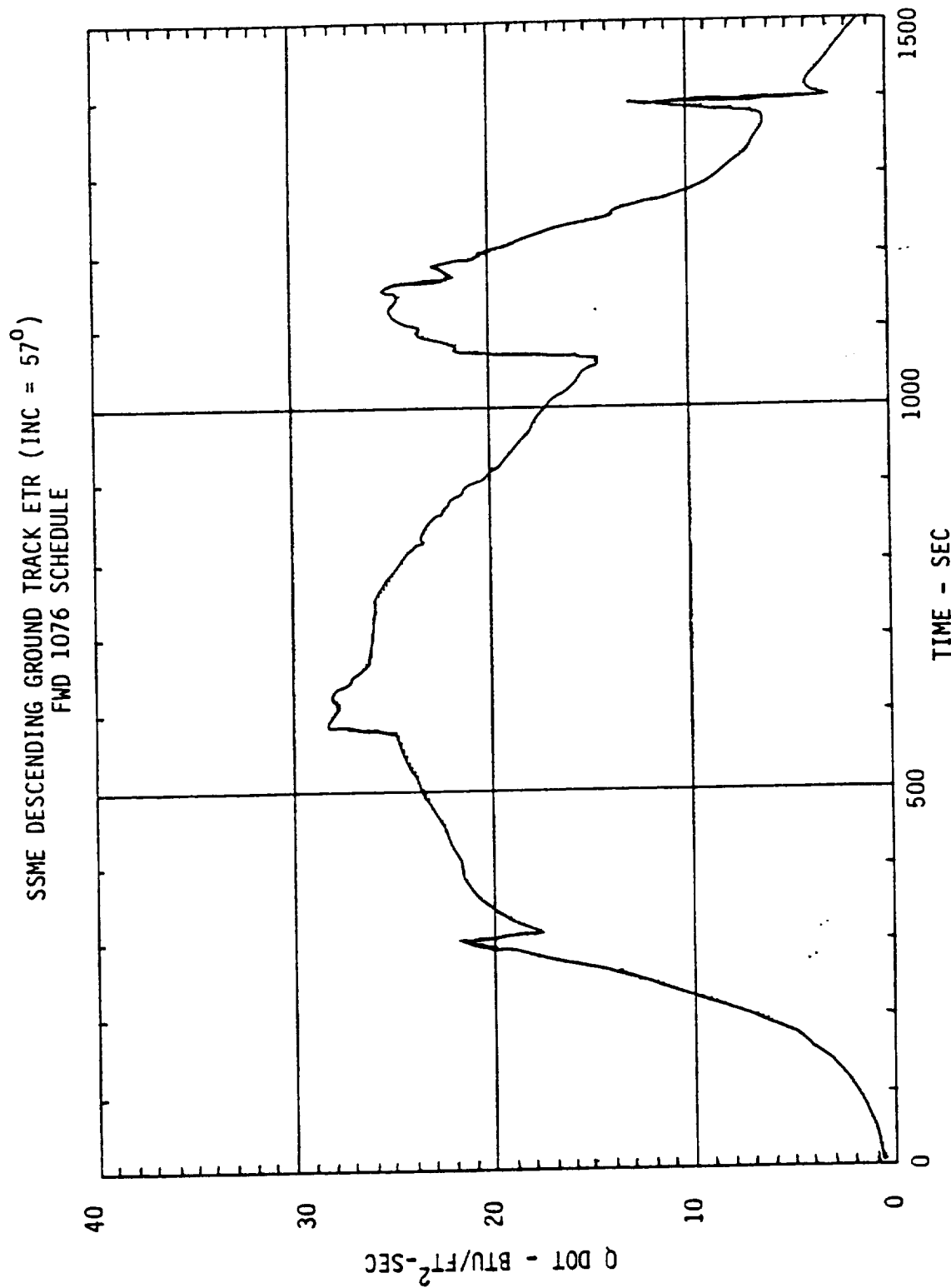


Figure 8.1.1: Worst Heating Time History

8.2 Ramp Design

The current "ramp" TPS two- and three-dimensional radiation thermal models were used to determine its peak usable heating rates. Since the thermal models contain negligible capacitance, the heating rate and time could be equivalenced. The two-dimensional model response is shown in Fig. 8.2.1. The three-dimensional corner model response is shown in Fig. 8.2.2. The critical heating rate (BTU/ft²-sec) levels for TPS damage can be summarized as follows:

TPS	$\epsilon = .625$	$\epsilon = .90$
Wedge Top	25.0	35.5
Wedge Side Corner	21.5	23.5
Manifold Corner	16.5	19.3

Further analyses were performed to determine the time required at higher heating rates to melt the nichrome screen and foils on the surface of the current "ramp" TPS configuration. The results of this thermal analysis are shown in Figs. 8.2.3 and 8.2.4.

Three-dimensional radiation interchange thermal models which were described in Section 3.2 for the STS-9, and the current "ramp" TPS configuration were thermally analyzed using the highest SSME reentry thermal environment (FWD 1076 Schedule) of the ETR. The results of these analyses are shown in Figs. 8.2.5 and 8.2.6. As can be observed from these figures, this thermal environment with the "ramp" TPS causes damage to the screen and foil. The surface of the TPS remains above the 2550°F screen melt temperature for approximately 300 seconds.

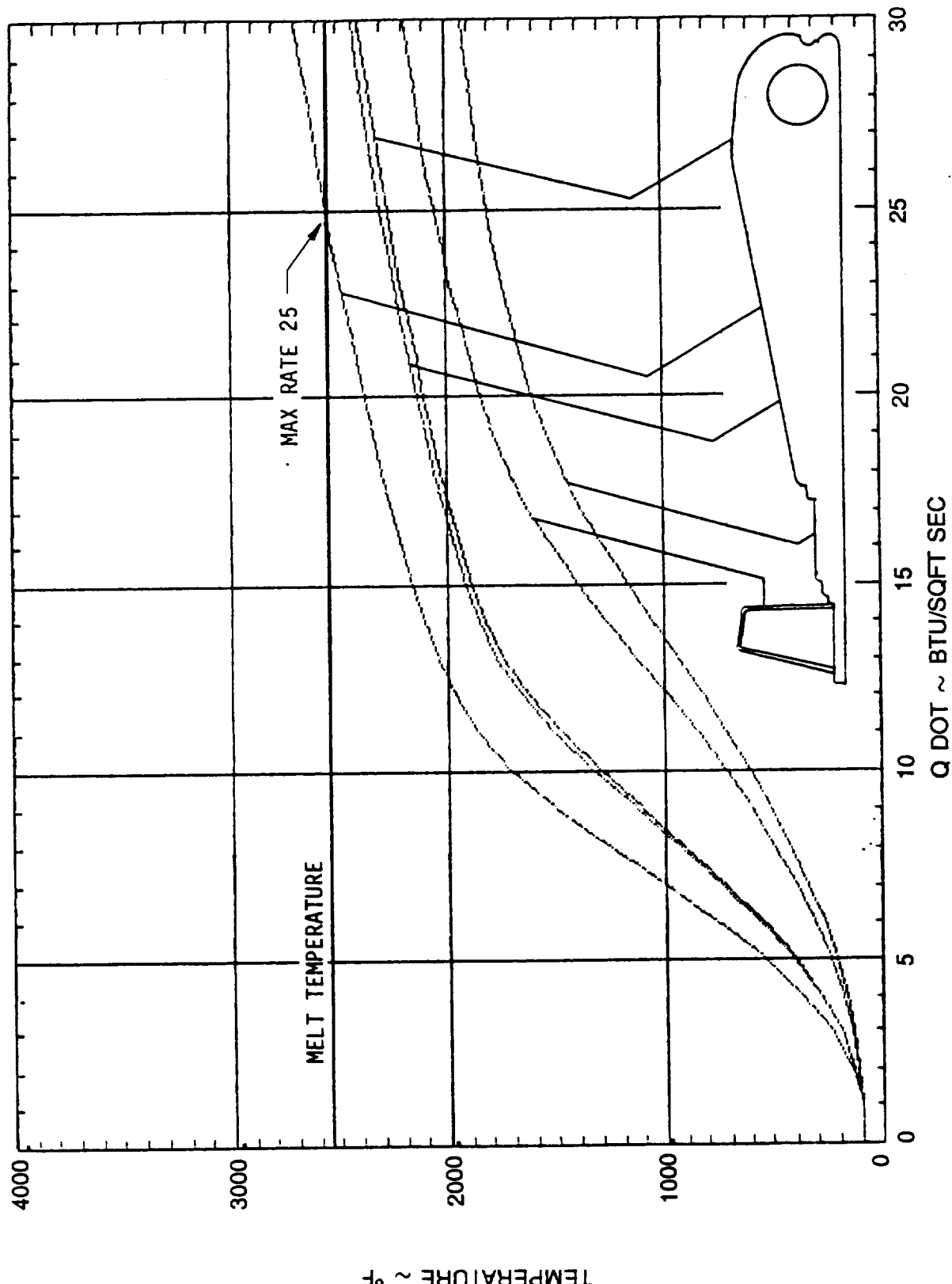


Figure 8.2.1: Current "Ramp" TPS Capability

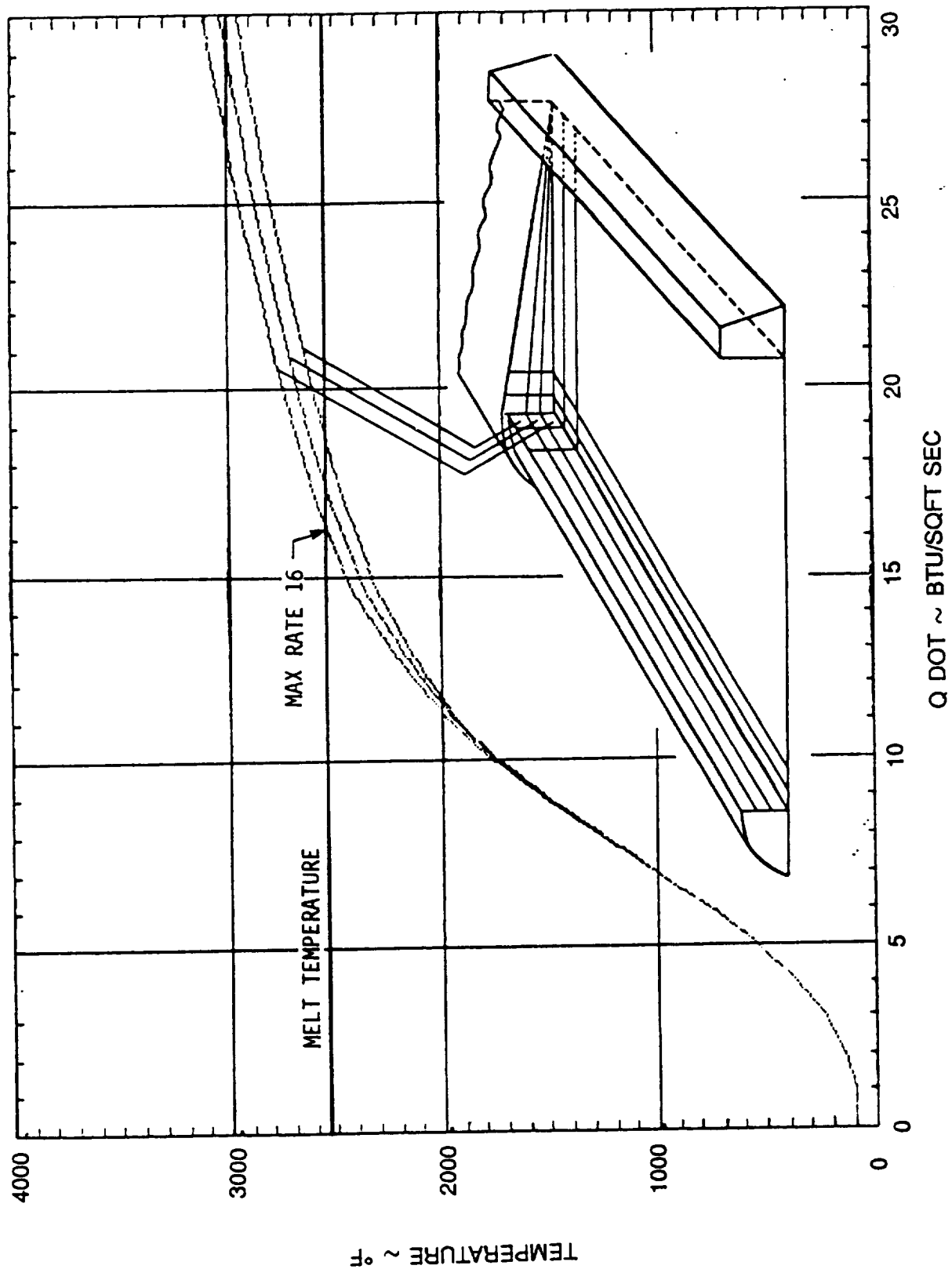


Figure 8.2.2: Current Corner "Ramp" TPS Capability

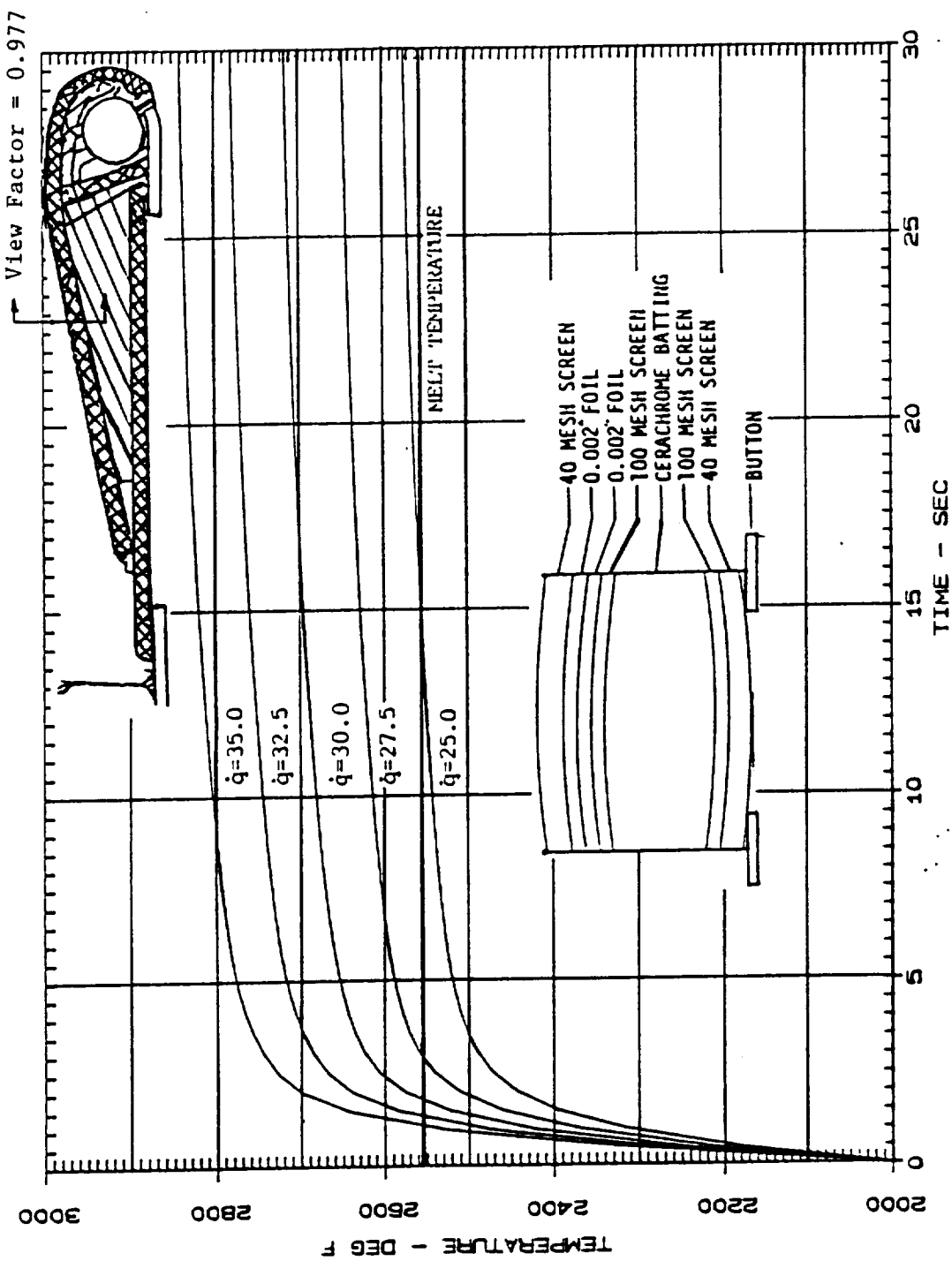


Figure 8.2.3: 1-D Thermal Model Surface Temperature Response

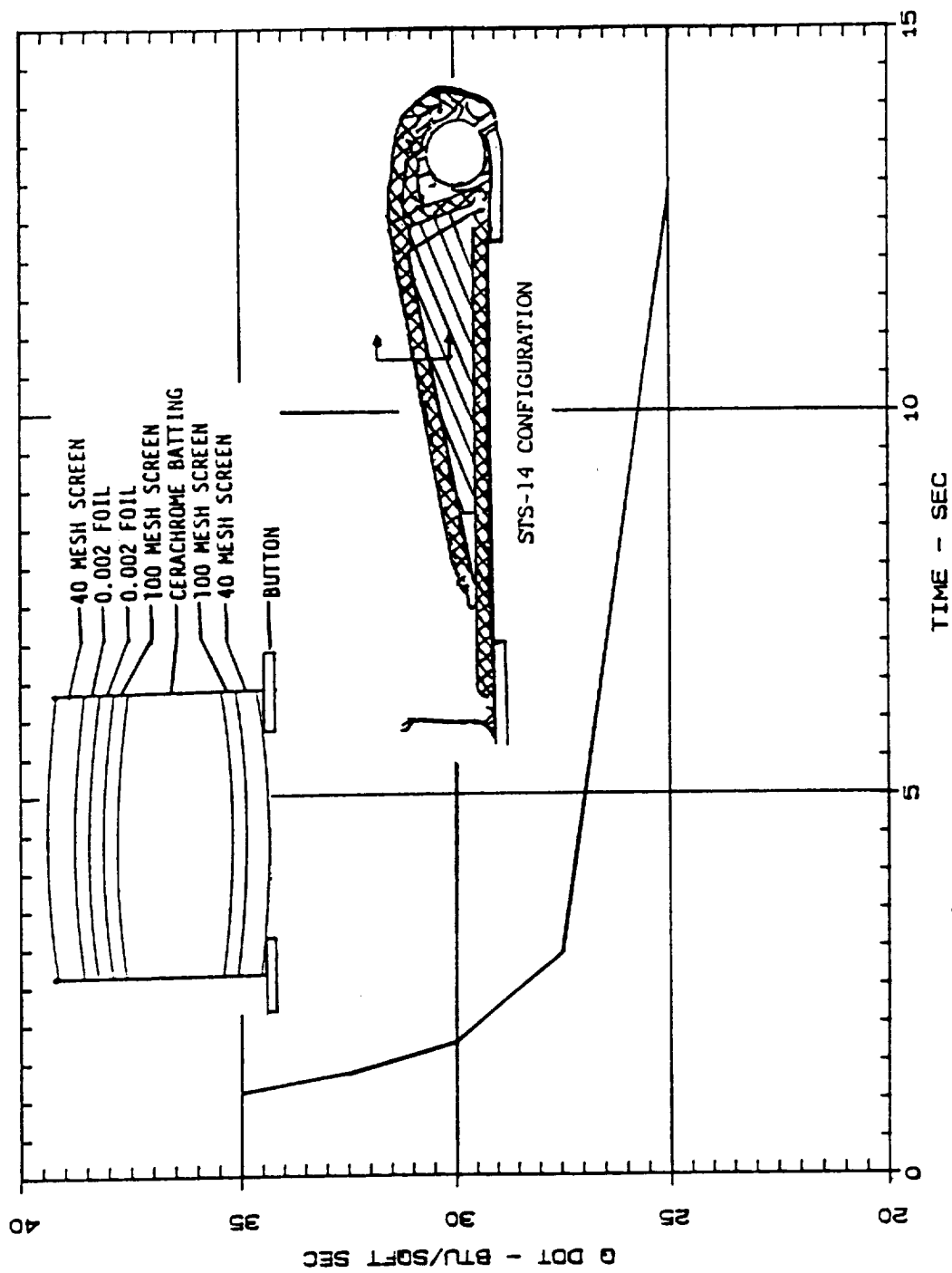


Figure 8.2.4: Time to Reach Nichrome Melt Temperature

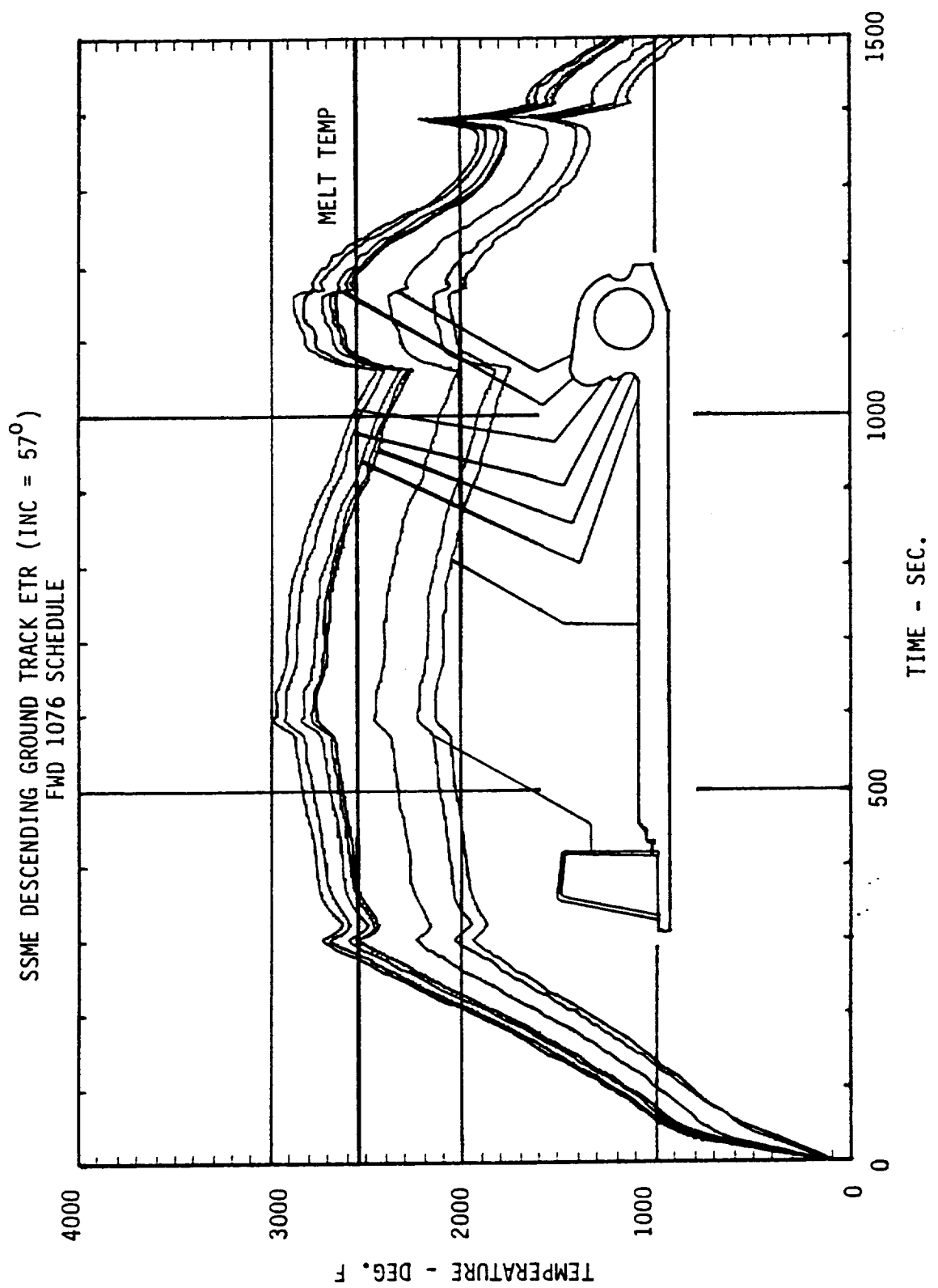


Figure 8.2.5: Radiation Equilibrium Temperature Analysis for STS-9

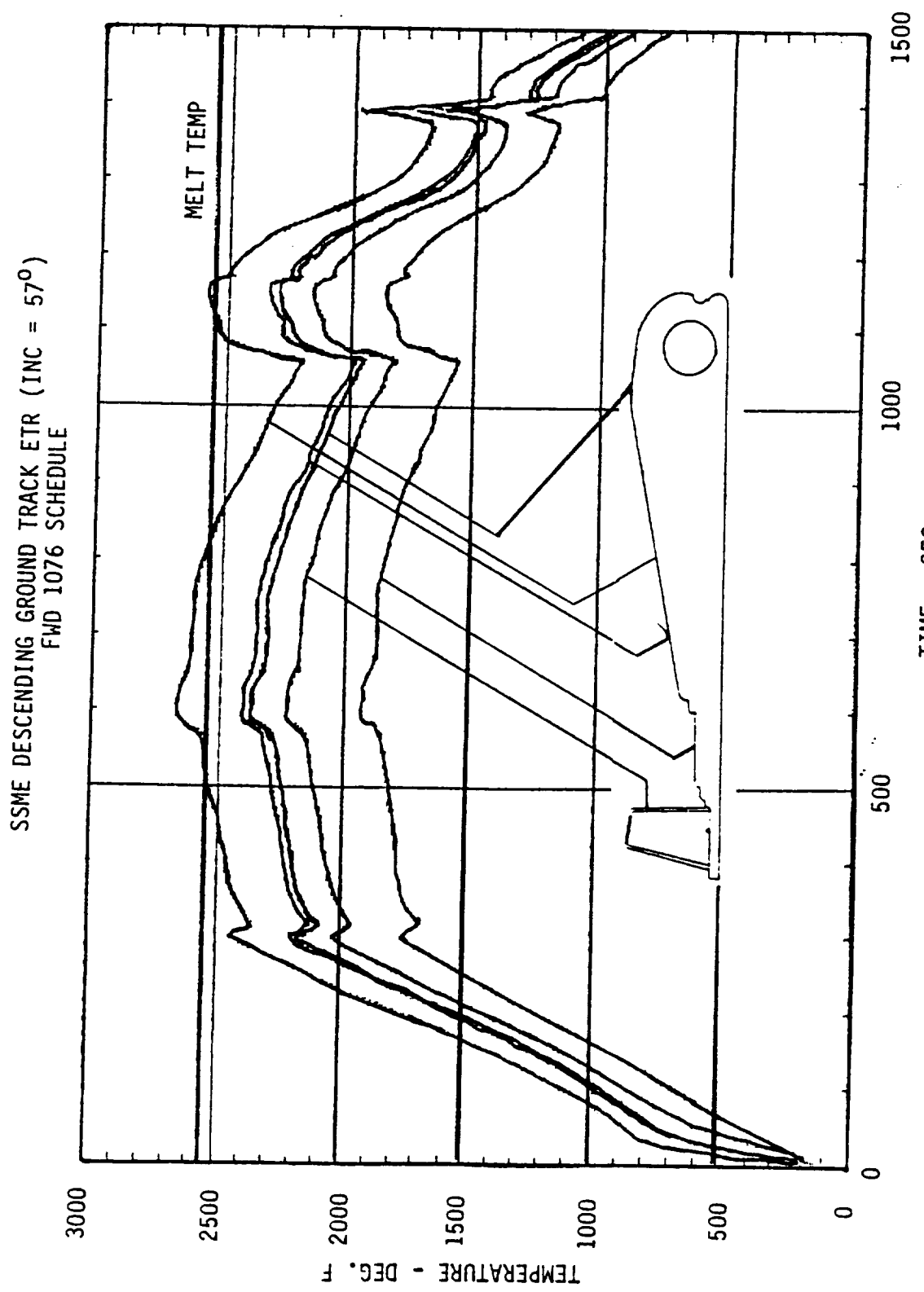


Figure 8.2.6: Radiation Equilibrium Temperature Analysis

Section 9

CONCLUSIONS AND RECOMMENDATIONS

9.1 Conclusions

Flight TPS thermal damage to the SSME external protection system demonstrated that the shear layer issuing from the elevon/body flap junction area has high heating potential. Fortunately, no nozzles were thermally damaged during the first 13 flights, which allowed this and other efforts to address the problem and implement corrective action. Based on the analysis performed, the following conclusions and recommendations were drawn.

- The preflight wind tunnel data base for nozzle heating could be used to predict the flight observed thermal damage if proper tunnel-to-flight scaling was performed. The data base was adequate and useful, contrary to thinking previous to the initiation of this effort
- The hot gas facility TPS provided viable data to compare thermal modeling methods with and provided local nozzle geometry heating distribution data for math modeling.
- The wind tunnel data were analyzed and correlated to produce a laminar set of data and scaling methodology. A procedure was developed to extend the data to turbulent flow. The test data was shown to be a mixture of laminar and turbulent data which should not be arbitrarily combined.
- Flight heating environment predictions were made using postflight trajectories. The current math model agreed with the postflight damage reports. Heating above a threshold value will produce TPS damage since the outer surface is a fast responding radiative equilibrium surface.
- Difficulties occurred in attempting to define design trajectories since several trajectory personnel considered angle-of-attack, body flap, elevon or sideslip excursions lasting approximately 2 sec or less to be insignificant. Thermally, these excursions can be, and probably are, the design drivers.
- Comparisons were made of the Rockwell design environment and the REMTECH design environment for IVBC-3. The peak heating rate distribution over the TPS agreed quite well, even though the two math models were significantly different. Subsequent changes to environments by Rockwell could not be verified since additional comparisons were beyond the scope of the present effort.

- Based on the thermal analysis and environment analysis work, REMTECH produced a new design concept for the nozzle TPS. The TPS consisted of a multilayered bridge over the aft manifold and aft two hatbands. The design met all thermal design criteria and was an acceptable weight. The design featured a Nicalon cloth sheet within the multilayer which would protect the nozzle when for near and at design condition the outer metallic TPS would fail.
- The Rocketdyne TPS which was proposed was analyzed for design thermal environment conditions. Outer surface failure of the TPS is predicted.

9.2 Recommendations

The current TPS is not totally satisfactory since failure is predicted at design conditions. The probability of nozzle thermal damage appears small, but finite. This risk could be mitigated by incorporating the Nicalon cloth sheet into the current design and circumferentially expanding the area protected by the TPS.

Section 10 REFERENCES

1. "An Investigation of Entry Heating on the 0.0175 Scale Space Shuttle Orbiter (Model 60-0 in the AEDC VKF Tunnel B (OH39A/B)," DMS-DR-2241, NASA-CR-160, 493, May 1980.
2. "Results from a Convective Heat-Transfer Rate Distribution Test on a 0.0175 Scale Model (22-0) of the Rockwell International Vehicle 4 Space Shuttle Configuration in the AEDC-VKF Tunnel (OH49A/B)," DMS-DR-2355.2222, NASA-CD 151, 066/147, 626, April 1974.
3. "Results of Heat Transfer Tests in the Arnold Engineering Development Center - Von Karman Facility Tunnels A and B Utilizing Space Shuttle Orbiter Thin Skin Thermocouple Models 56-0, 60-0, and 83-0. Test OH-84B." DMS-DR-2464, NASA-CR 160, 831, May 1981.
4. "Results of Tests on a 0.0175 Scale Model (60.0) of the Space Shuttle Orbiter to Determine Reentry Mode Convective Heat Transfer Rates on the Upper Wind Surface and SSME Nozzles in the AEDC VKF "B" Hypersonic Wind Tunnel (OH98)," DMS-DR2340, NASA-CR-160, 501, August 1980.
5. Bancroft, Steven A. and Pond, John E., "SSME Nozzle TPS Response in the MSFC's Hot Gas Facility," REMTECH Technical Report RTR 113-01, March 1985.
6. Pond, J. E. and Schmitz, Craig P., "MINIVER Upgrade for the AVID System," NASA CR 172214, Vol. III: "EXITS User's and Input Guide," August 1983.
7. "Angle of Attack Envelope to Support Space Shuttle Main Engine Nozzle Heating Analysis," NAS/JSC DM3-87-111, October 5, 1987.
8. "Minutes of System Integration Review," September 22, 1987.
9. "Angle of Attack, Elevon and Body Flap Dispersions for SSME Nozzle Heating Analysis," IL-283-210-87-019, Flight Control, Rockwell Space Division, September 18, 1987.
10. "Space Shuttle IVBC-3 SSME Entry Aeroheating Data Book," STS 85-0462, September 1985.
11. "Refractory Products K," Ken Caryl, Johns-Mansville Corp., Denver CO 80217, IND-321, July 1981.
12. Blair, W., Meaney, J. E., and Rosental, H. A., "Fabrication of Prepackaged Superalloy Honeycomb TPS Panels," NASA CR-3755, October 1985.

13. "Space Shuttle Program Thermodynamic Design Data Book TPS Acreage Methods Validation," Rockwell International, Space Transportation System Integration and Operations Division Space System Group, SD73-SH-0226C, October 1981.
14. "Informal Communication," Bill Miller, Research and Development Center, Johns-Manville Corp., Denver CO, March 1986.
15. "Informal Communication," Monro Schumate, Research and Development Center, Johns-Manville Corp., Denver CO, March 1986.

Appendix

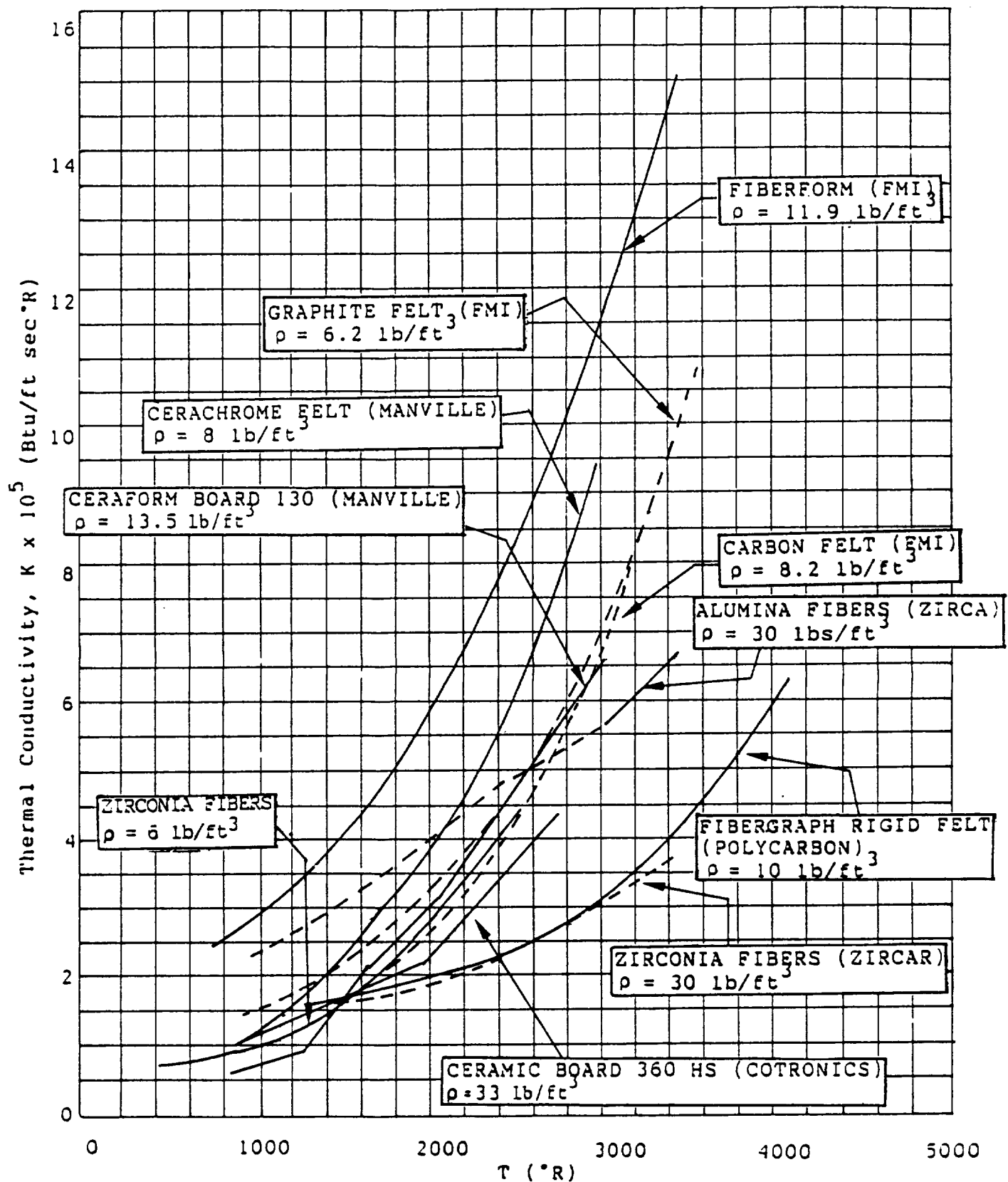


Figure A1: Thermal Conductivity vs. Temperature

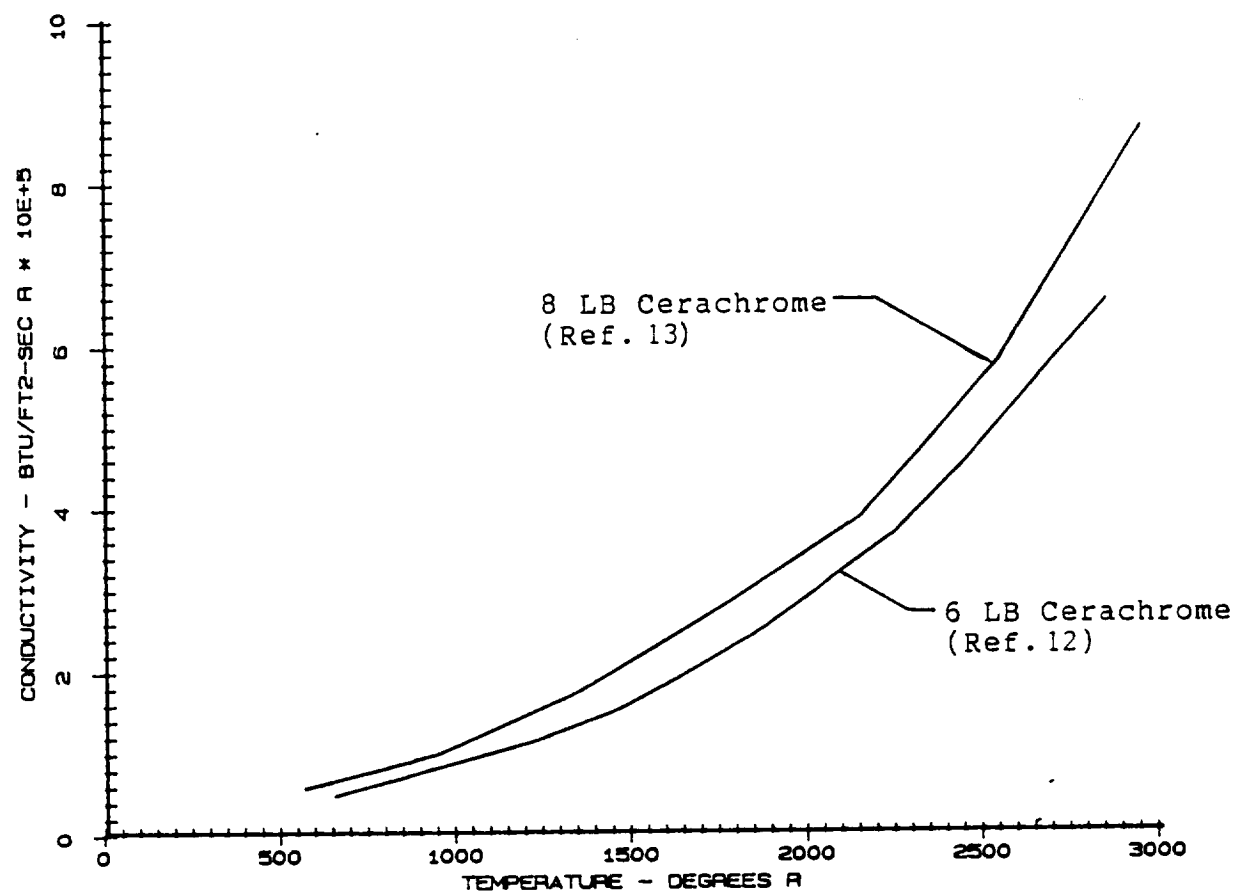


Figure A2: Comparison of Different Cerachrome Conductivity

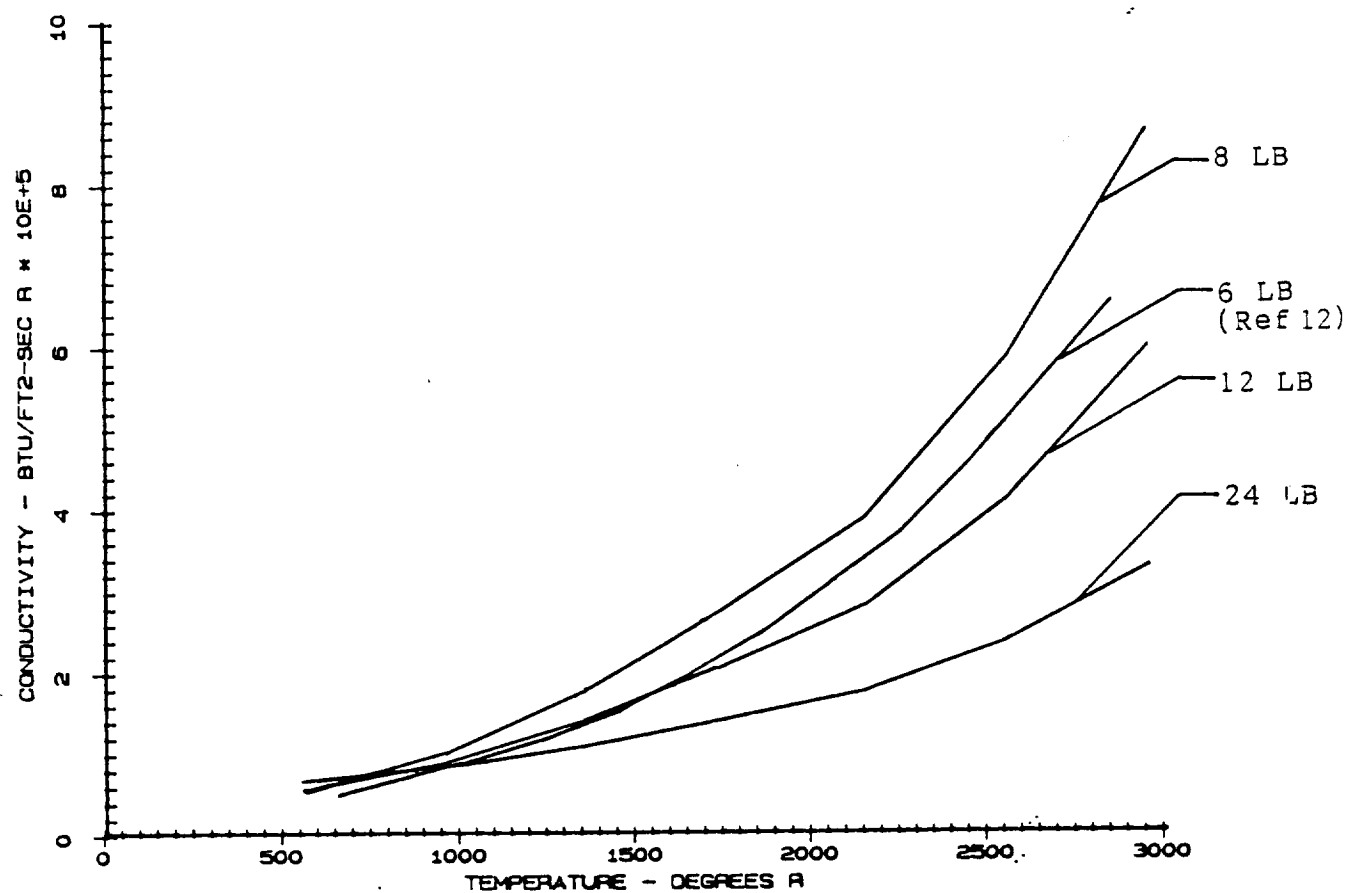


Figure A3: Conductivity vs. Temperature for Different Cerachrome Density (Ref. 6)

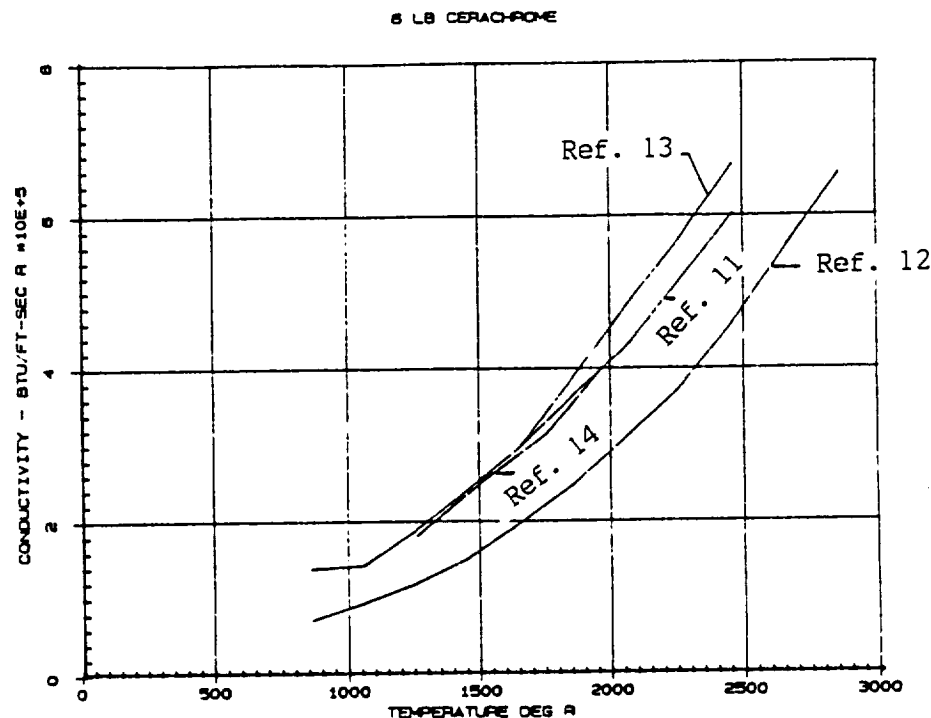


Figure A4: Thermal Conductivity vs. Temperature for 6 Lb. Cerachrome

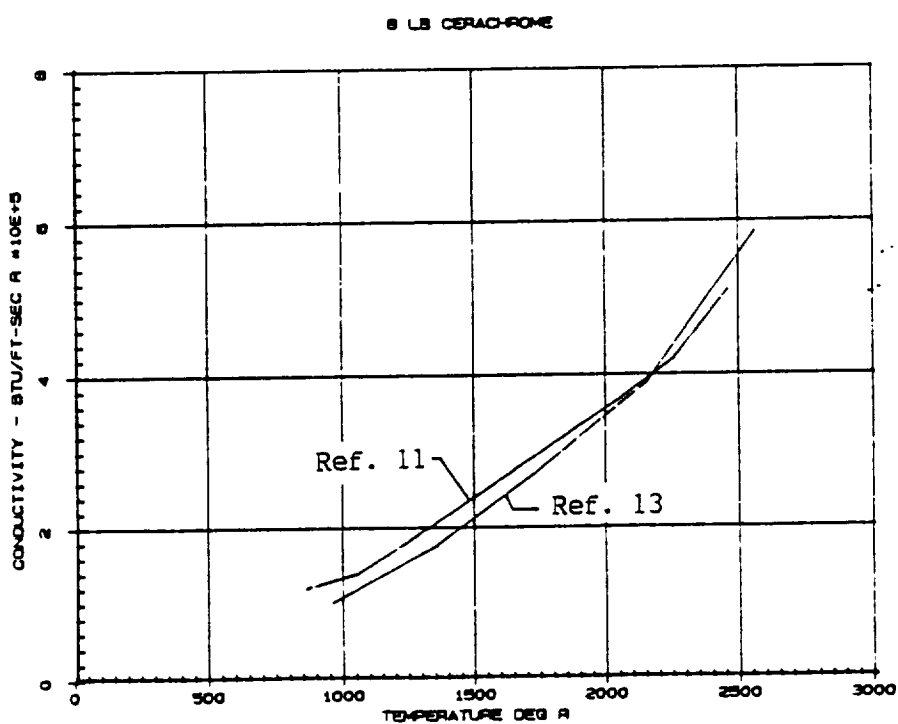
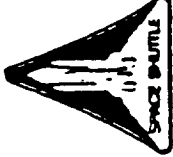


Figure A5: Thermal Conductivity vs. Temperature for 8 Lb. Cerachrome

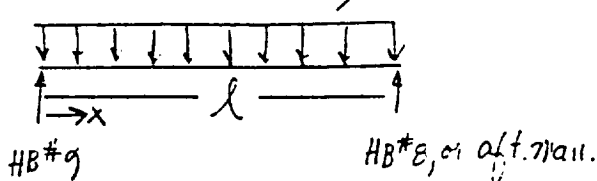


UPRATED DESIGN THERMAL PROTECTION SYSTEM MATERIAL PROPERTIES COMPARISON

NICHROME		SILICON CARBIDE	
EMISSIVITY	0.65 - 0.79	0.7	
STRENGTH (KSI @ R.T.)	100 - 200	350 - 470	
SPECIFIC HEAT (CAL/GM °K)	0.1	0.15	
THEMAL CONDUCTIVITY (BTU IN. /HR FT. ² °F)	880	80	
DENSITY	9.3	2.55	
MELTING TEMP (°F)	2550	3200 - 3400	
HEAT FLUX BALANCE	22 BTU	≈ 56 BTU	
MELTING POINT	FT. ²-SEC.	FT. ²-SEC.	

٢٦١

Rockwell International
Rockford Division
Doc. #13327



$\sigma_{ad} = 5 \text{ psia}$, given by Cal Engg, 7-30-66,
includes safety factor.

$$\text{eq's } \left[V = \frac{w-l}{2} - wx \right. \\ \left. M = \frac{wx(l-x)}{2}, \sigma = \frac{M(S.F.)}{z} = \frac{wx(S.F.)(l-x)}{2z} \right]$$

$$w = 5 \frac{\text{lb}_f}{\text{in}^2} \left(\frac{600 \text{ in}^2}{12.5 \text{ in}} \right) = 240 \frac{\text{lb}_f}{\text{in}}, \quad l = 12.5 \text{ in}$$

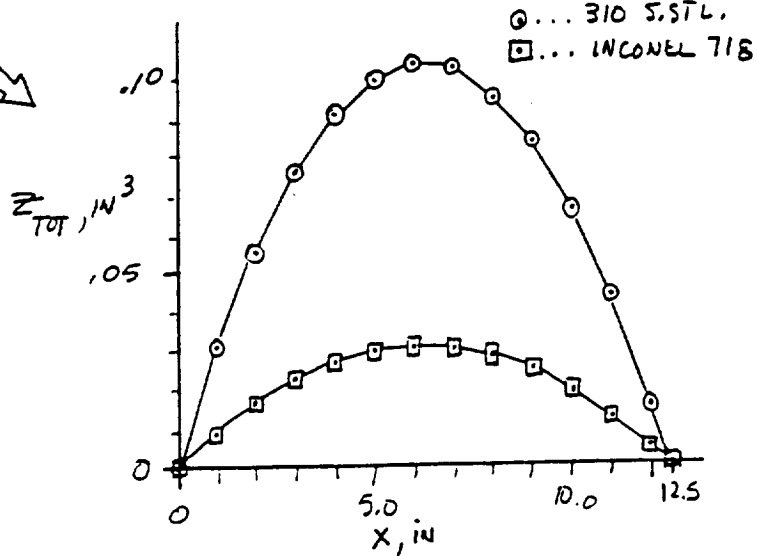
In this design exercise we will evaluate 2 construction walls:

1) ~~AISI 310 ($\sigma_y = 45 \text{ KPSI}$, $\sigma_{UT} = 75 \text{ KPSI}$)~~ Delete.

2) INCONEL 718 ($\sigma_y \approx 150 \text{ KPSI}$) $\rho \approx 36 \frac{\text{lb}_f}{\text{in}^3}$

$$Z_{TOT} \Big|_{req'd} = \frac{wx(l-x)}{2\sigma} = \frac{240 \frac{\text{lb}_f}{\text{in}}(x)(12.5-x)}{2 \cdot \frac{45}{12.5 \text{ in}^2}} = \frac{120x(12.5-x)}{\sigma} \dots \text{in}^3$$

$x, \text{ in}$	$Z_{TOT}, 310$	$Z_{TOT}, \text{INCONEL}$
0.0	0.00	0.000
1.0	.031	.009
2.0	.056	.017
3.0	.076	.023
4.0	.091	.027
5.0	.100	.030
6.0	.104	.031
7.0	.103	.031
8.0	.096	.029
9.0	.084	.025
10.0	.067	.020
11.0	.044	.013
12.0	.016	.005
12.5	.000	0.000
6.25	.1042	.03125



GRAPH 1: SECTION MODULUS = f(DIST. FROM H.P. 9)

E). calculate flat strip inconel grating:

$\text{Mach } Z = .03125 \text{ in}^3$, for bending about xx

$$\times \begin{array}{c} \text{---} \\ | \quad \quad | \\ \text{---} \end{array} \times Z = \frac{xt^2}{6}, \therefore x = \frac{6(.03125)\text{in}^3}{t^2 \mu^2} = \frac{1}{5.333t^2} \dots \text{eq1}$$

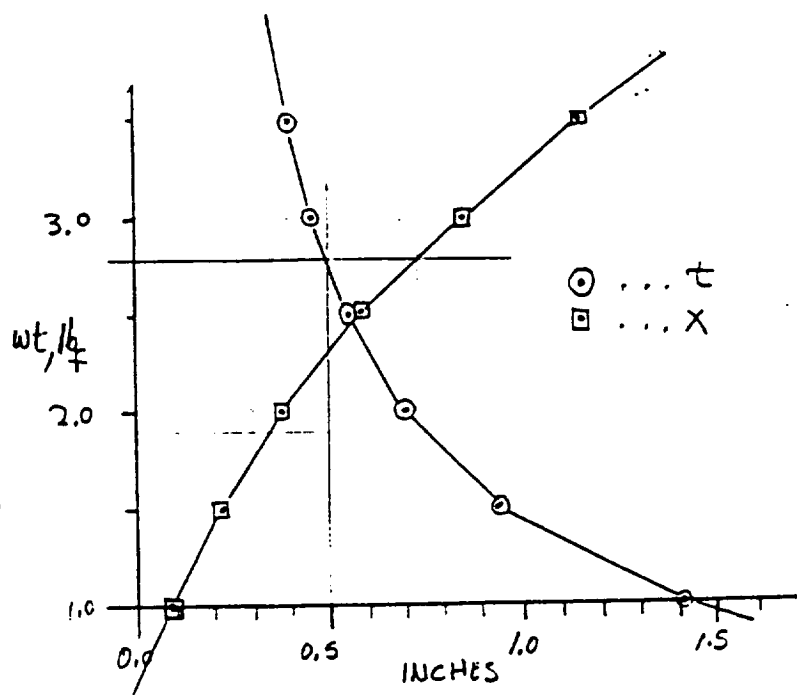
$$\therefore \text{total strip wt} = x(t) 25 \mu \left(\frac{.316_f}{\text{in}^3} \right) \approx \text{wt } 1b_f \quad \begin{array}{l} \text{DESIROD WT} \\ \text{INCONEL} \end{array}$$

$$\text{or } x = \frac{\text{wt } \mu^2}{.3(25)t} : \frac{(\text{wt})}{7.5t} \dots \text{wt in } 1b_f, \text{ eq2}$$

Equating ① & ② :

$$5.333t^2 - \frac{7.5t}{(\text{wt})} = 0 \dots \text{wt in } 1b_f, t \text{ in inches}$$

wt, $1b_f$	t	x
1.0	1.4063	.0948
1.5	.9375	.2133
2.0	.7031	.3793
2.5	.5625	.5926
3.0	.4687	.8533
3.5	.4018	1.1615



$$\text{From fig: } t = .5, \therefore x = .74$$

$$\therefore \text{wt} = .5(.74) 25(.3) = 2.8 \text{ lb}_f$$

GRAPH 2: INCONEL STRIP, $Z = .03125$

Design A cont'd:

force $a = 1.0"$, $t = 20 \text{ vss ga. (.0375")}$, 9 beams (6" pitch)

\therefore for 9-beam, $b_{regd} \approx .5$ inches MAX

$$\therefore \text{wt} \approx \left[9 \left[2(.5) + 1 \right] .0375 \right] \text{in}^2 (2510) \left| \begin{array}{c} \text{total} \\ \text{row} \end{array} \right| \left(\frac{.28lb_f}{in^3} \right) \left| \begin{array}{c} \rho \\ \text{stainless} \end{array} \right| + 25\% \text{ATTACI}$$

$$= 5.9lb_f$$

It will probably be difficult to get a section that will be stiff enough (out of any stainless) and still weigh below 3lb_f.

II) DESIGN B

Suggest INCOVEL ALLOY 71B (weld up, anneal, then age harden; then if kept below $\approx 1300^\circ F$, σ_y should be ≈ 150 KPSI), $\rho \approx \frac{3lb_f}{in^3}$

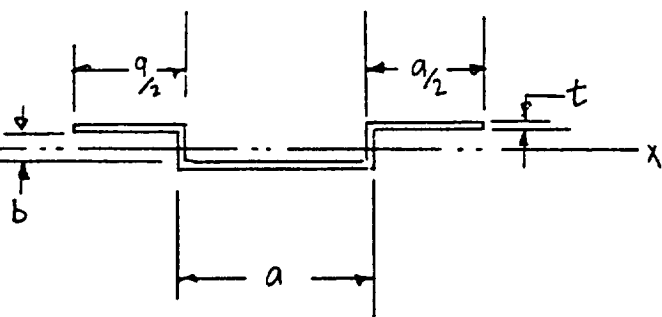
$$\therefore Z_{BR} = \frac{240lb_f}{in} \frac{(x)(12.5-x)}{2(150000 \frac{lb_f}{in^2})} = 8 \times 10^{-4} x (12.5-x) in^3$$

$$= .01x - .0008x^2 in^3 \dots \dots x \text{ in inches}$$



* * per 8-4-86 furnished to International Nickel Co., 1-800-624-3411,
Sam Kaiser.

II) Evaluate INCONEL section:

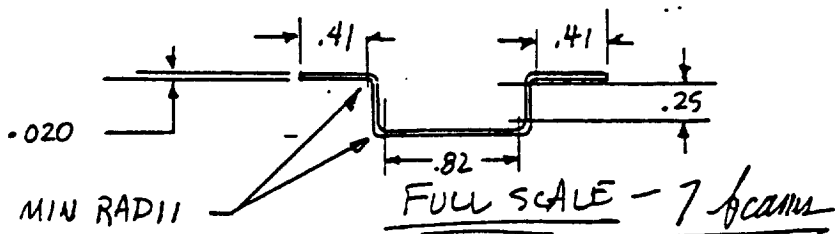


$$\frac{Z_{xx}}{c} = \frac{2 \left[\frac{at^3}{12} + at(b/2 + t/2)^2 + \frac{tb^3}{12} \right]}{(b/2 + t)} = .03125 \text{ in}^3$$

May $Z = .03125 \text{ in}^3$ fit bending about xx :

trial #1: (choose 7 beams, 10 deg spaces)

set $\begin{cases} b = .25 \text{ in} \\ t = .020 \text{ in} \end{cases}$
trial & error: $a = .82 \rightarrow \underline{\text{OK}}$

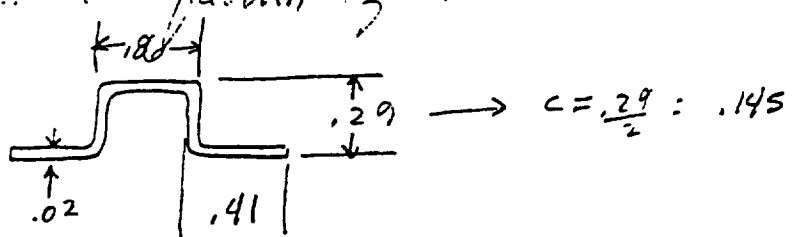


- 1) LENGTHS DO NOT INCLUDE RADII
- 2) ANNEAL, SHEAR, BEND, WELD, ANNEAL, HARDEN TO $S_y = 150 \text{ KPSI MIN}$, ($R_c = \underline{60}$?)

$$wt \approx 7 \left[2(.82) + 2(.25) + 4(.07) \right] (.020) \left[\frac{.25}{.125} \right] \left[\frac{.3}{.020} \right] = 2.54 \text{ lb}_f$$

(Sect - 1-15-87)

Evaluate deflection of the section

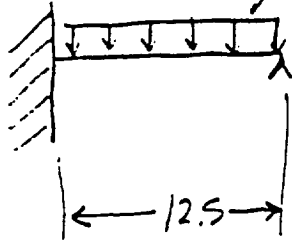


$$Z = \frac{2 \left(.86 \frac{(.02)}{12} \right)^3 + .86(.02) \left(.125 + .01 \right)^2 + .02 \frac{(.25)}{12}^3}{(.125 + .02)}$$

$$= .004691 \text{ in}^3$$

$$E_{\text{concrete}} = 31 \times 10^6 \text{ psi}$$

$$w = \frac{240 \text{ lb}_F / \text{in}}{7 \text{ spans}} = 34.29 \frac{\text{lb}_F}{\text{in}} \text{ per beam}$$



$$\delta_{\text{max}} = \frac{wl^4}{18EI} = \frac{34.29 \frac{\text{lb}_F}{\text{in}} (12.5)^4}{185 (31 \times 10^6) \frac{\text{lb}_F}{\text{in}^2} (.004691 \text{ in}^3)(.145 \text{ in})}$$

$$= .215 \text{ in} \quad \underline{\text{for beams only}}$$

Assuming other structures add $\approx 15\%$ strength,

$$\text{then } S \approx .215 (.85) = \underline{.18 \text{ in}}$$

ORIGINAL PAGE IS
OF POOR QUALITY

